**No. 2000:5** UDK 537.8

**Abstracts of the URSI XXV National Convention on Radio Science**
Helsinki, 21–22 September 2000

Ari Viljanen, Risto Pirjola and Tapio J. Tuomi (editors)

Finnish Meteorological Institute
Geophysical Research Division
Helsinki 2000

ISBN 951–697–531–3
ISSN 0782–6079

Edita Oy
Helsinki 2000

**Finnish Meteorological Institute**

Series title, number and report code of publication

Published by Finnish Meteorological Institute
Vuorikatu 24, P.O. Box 503
FIN-00101 Helsinki, Finland

Date September 1, 2000

Authors

Ari Viljanen, Risto Pirjola
and Tapio J. Tuomi (editors)

Name of project

Commissioned by

Title

Abstracts of the URSI XXV National Convention on Radio Science

Abstract

The URSI XXV National Convention on Radio Science was held in Helsinki on September 21—22, 2000. This book contains the program of the meeting and abstracts of the presentations.

Publishing unit
Geophysical Research

Classification (UDK)
537.8

Keywords
electromagnetics,
URSI

ISSN and series title
0782-6079 Raportteja - Raporter - Reports

ISBN
951-697-531-3

Language
English

Sold by
Finnish Meteorological Institute / Library
P.O.Box 503, FIN-00101 Helsinki
Finland

Pages 108 Price

Note

## Preface

URSI XXV National Convention on Radio Science
Säätytalo & Tieteiden talo, Helsinki, Finland
September 21–22, 2000

It is my great pleasure to welcome you to the XXV National Convention on Radio Science held at “Säätytalo” and “Tieteiden talo” in Helsinki, Finland. The conference is organized by the Finnish National Committee of the International Union of Radio Science (URSI). The local arrangements are carried out by the Geophysical Research Division of the Finnish Meteorological Institute.

The scientific and technological areas in which URSI is working today are very wide extending from space physics to electronics and biological effects of electromagnetic fields. The activities of URSI are conducted by ten Commissions. As a Finnish National URSI Convention is held every year, it is the idea that the topics of all commissions will be raised as highlights at least once every three years. Each time the selection of the topics of the sessions also reflects the interests of the organizing institute. Therefore the present Convention has sessions on Radars, Space Weather and Natural Electromagnetic Fields. Wireless Communication constitutes one of the most important subjects in our modern society, which is also seen in the great number of abstracts submitted on this topic. Thus, we have two sessions on Wireless Communication at this Convention. One of the topics is Electromagnetic Theory which, although founded already more than 100 years ago, is still a very significant, active and continuously–growing research area.

As at previous Conventions, a Young Scientist Award will be delivered to an author (under 35 years of age) whose abstract and presentation are considered outstanding by the Award Committee.

The sponsorship by Nokia Corporation, Sonera Oyj, Fingrid Oyj and Space Systems Finland Ltd to the Convention is gratefully acknowledged.

Finally, I wish to thank the invited speakers, other authors, session chairpersons and the members of the Organizing Committee for making this Convention successful. Special thanks go to Dr. Ari Viljanen, Secretary of the Organizing Committee.

Risto Pirjola
Chairman of the Organizing Committee

## Members of the Organizing Committee

Risto Pirjola (chairman)
Martti Hallikainen
Hannu Koskinen
Heikki Nevanlinna
Jaan Praks
Tapio Tuomi
Ari Viljanen (secretary)

## Program

URSI XXV National Convention on Radio Science
Säätytalo and Tieteiden talo, Helsinki, Finland
September 21–22, 2000

**Thursday 21.9.2000**

09.00–09.30: *Registration + Coffee* (Säätytalo)

09.30–10.15: *Opening Session* (Säätytalo)

Risto Pellinen (Director of FMI/GEO)

Martti Hallikainen (Chairman of the Finnish URSI)

Risto Pirjola (Chairman of the Organizing Committee)

10.15–11.30: *Plenary Session* (Chair: Risto Pirjola) (Säätytalo)

10.15–10.45
Martti Tiuri (invited): Scientists and science policy in the knowledge society

10.45–11.30
Heikki Huomo (invited): Wireless Internet

11.30–13.00: *Lunch Break*

13.00–17.00: *Parallel Sessions* (Tieteiden talo)

1. *Radars and Remote Sensing* (Chair: Tapio Tuomi)

13.00–13.30
M. Uspensky (invited): SuperDARN: A global–scale network of HF and VHF radars for sensing backscatter from ionospheric irregularities in the E– and F–regions of the high–latitude ionosphere

13.30–14.00
R. King, A. Huuskonen, K. Leminen and H. Kärki (invited): Luosto: a new generation weather radar in Finland

14.00–14.30
M. Hallikainen (invited): Future trends in spaceborne radar technology and applications

14.30–15.00: *Coffee Break*

15.00–15.30
M. Lehtinen (invited): Development of new radar methods based on mathematical modelling of radar coding

15.30–15.45
J. Koistinen: The effect of bird migration on Doppler weather radar measurements

15.45–16.00
M. Engdahl: Helsinki and its surroundings seen with multitemporal INSAR

16.00–16.15
A. N. Arslan, J. Koskinen, J. Pulliainen and M. Hallikainen: The use of synthetic aperture radar data on modeling of forest canopy covered by snow

16.15–16.30
A. N. Arslan, W. Huining, J. Pulliainen and M. Hallikainen: Effective permittivity of wet snow

16.30–16.45
J. Praks: Polarimetric SAR image classification with normalized coherency matrix

16.45–17.00
Y. Zhang, S. Koponen, J. Pulliainen and M. Hallikainen: Turbidity detection using AVHRR satellite imagery in the Gulf of Finland

2. *Electromagnetic Theory* (Chair: Ismo Lindell)

13.00–13.30
S. Dudorov, D. Lioubtchenko, J. Mallat, J. Tuovinen and A. V. Räisänen: Low loss dielectric waveguides at 75–110 GHz frequency range

13.30–14.00
V. S. Möttönen, P. Piironen and A. V. Räisänen: Low–loss bias–T for 4–15 GHz

14.00–14.30
A. Hazmi, J. Rinne and M. Renfors: Transmission of DVB–T signal over cable TV network

14.30–15.00: *Coffee Break*

15.00–15.30
A. Viitanen: Chiral soft and hard surface waveguide mode transformers

15.30–16.00
S. Tretyakov and A. Sihvola: Onsager–Casimir principle and reciprocity of complex composite media

16.00–16.30
T. Uusitupa and K. Kärkkäinen: Studying photonic bandgap waveguides using FDTD

16.30–17.00
I. V. Lindell: Ideal boundary conditions in electromagnetics

*Poster viewing during coffee breaks*

18.00–20.00: *Cocktail Party at FMI/GEO*
All participants are welcome!
Address: Vuorikatu 15A, 3rd floor (close to the Kaisaniemi Metro station)

**Friday, 22.9.2000**

09.00–11.30: *Parallel Sessions* (Tieteiden talo)

1. *Wireless Communication – Part I* (Chair: Veikko Porra)

09.00–09.20
P. Eskelinen and H. Eskelinen: Improvements of welded RF components through computer simulations

09.20–09.40
P. Eskelinen: Performance limitations of tactical mobile VHF antennas

09.40–10.00
P. Eskelinen and P. Sjöman: A short performance evaluation of the Metsähovi clock arrangement for VLBI measurements

10.00–10.30: *Coffee Break*

10.30–10.50
J. Häkli, J. Säily, J. Ala–Laurinaho, J. Tuovinen and A. V. Räisänen: Current status of the sub-millimetre wave hologram compact antenna test range

10.50–11.10
J. Säily, J. Mallat and A. V. Räisänen: Development of a phase–locking system for submillimetre wave backward–wave oscillators

11.10–11.30
M. Kärkkäinen, J. Riska, P. Kangaslahti and V. Porra: LNA and mixer circuits for a 60 GHz Radio Front End

2. *Space Weather* (Chair: Hannu Koskinen)

09.00–09.30
S. Korpela and F. von Schoultz (invited): New European satellite navigation service Galileo

09.30–10.00
M. Poutanen (invited): Ionospheric effects in GPS observations

10.00–10.30: *Coffee Break*

10.30–11.00
T. Nygrén, M. Lehtinen and E. D. Tereshchenko (invited): Determination of ionospheric electron density by means of satellite radiotomography

11.00–11.15
J. Mannermaa, K. Kalliomäki and T. Mansten: Detection of tracking loops performance of GPS receivers from PPS measurements

11.15–11.30
K. Kauristie, O. Amm, E.I. Kallio, P. Janhunen and A. Viljanen: Ground–based space weather observations using the MIRACLE system

11.30–11.45
J. Elovaara: Geomagnetically induced currents and their effects in the Finnish power system

11.45–12.00
A. Pulkkinen, K. Pajunpää, A. Viljanen, R. Pirjola, D. Boteler and L. Trichtchenko: Project on geomagnetically induced currents in the Finnish natural gas pipeline network

12.00–13.00: *Lunch Break*

13.00–16.30: *Parallel Sessions* (Tieteiden talo)

1. *Wireless Communication – Part II* (Chair: Martti Hallikainen)

13.00–13.40
J. Lähteenmäki (invited): Radiowave propagation aspects of mobile location techniques

13.40–14.05
H. Laitinen, T. Nordström and J. Lähteenmäki: Location of GSM terminals using a database of signal strength measurements

14.05–14.30
J. Saijets, M. Åberg and M. Andersson: CMOS RF models for mobile radio IC design

14.30–15.00: *Coffee Break*

15.00–15.25
V. Golikov, S. Hienonen, T. Sehm and P. Vainikainen: A passive intermodulation phenomenon in base station antenna design for mobile networks

15.25–15.50
C. Icheln and P. Vainikainen: Designing a dual–frequency balun to eliminate the effect of RF feed cables in measurements of small antennas

15.50–16.15
N. Y. Ermolova: Multiple–signal intermodulation in the nonlinear radio devices

2. *Natural Electromagnetic Fields* (Chair: Heikki Nevanlinna)

13.00–13.25
T. J. Tuomi: Multichannel lightning flashes detected in Finland in 1998–2000

13.25–14.00
J. Elovaara (invited): Co–operation of Fingrid and Finnish Meteorological Institute in questions related to natural electromagnetic fields

14.00–14.30
A. Väänänen: New research radars in Sodankylä

14.30–15.00: *Coffee Break*

15.00–15.25
N. Partamies, K. Kauristie, P. Eglitis and M. Uspensky: Sudden impulse events observed by magnetometers and coherent radars

15.25–15.50
R. Pirjola: Geoelectromagnetic modelling at the Finnish Meteorological Institute

15.50–16.15
J. J. Hänninen, I. V. Lindell and R. Pirjola: Exact image theory applied to geophysics

16.30–17.00: *Closing Session including Young Scientist Award* (Tieteiden talo)

*Poster viewing during coffee breaks*

## Contents

# Plenary Session

# SCIENTISTS AND SCIENCE POLICY IN THE KNOWLEDGE SOCIETY

Martti Tiuri
Parliament of Finland
martti.tiuri@eduskunta.fi

The developed countries are transforming to a knowledge society. Knowledge is applied purposefully in all fields and new knowledge is searched systematically. The most important means to get new knowledge is scientific research. Hence science and science policy are very important in the future society. It is necessary that as many scientists as possible inform their result clearly to laymen so that they understand and approve the significance of scientific research. Only this way it can be guaranteed that the knowledge society can develop without difficulties, which are caused by misinformation and fear. Another reason for increased scientific information is science policy. The resources of scientific research can be secured only if people understand the importance of science for the advancement of the society.

# WIRELESS INTERNET

Heikki Huomo
Nokia Research Center
heikki.huomo@nokia.com

The wireless Internet will introduce revolutionary new applications that pave the way toward a mobile information society. Third generation mobile communication systems and broadband wireless access systems will play the key role in enabling wireless Internet. Because of rapidly increasing system complexity, wireless terminal manufacturers face huge challenges in ensuring fast product creation. In the radio frequency section, the main challenge is to achieve high overall linearity with low power consumption and low implementation complexity. In the baseband section, managing complexity remains the key challenge; it requires a paradigm shift in system and IC design practices, the design re-use of circuit blocks.

# Radars and Remote Sensing

**SuperDARN: A global-scale network of HF and VHF radars for sensing backscatter from ionospheric irregularities in the E- and F-regions of the high-latitude ionosphere**

Mikhail Uspensky
Finnish Meteorological Institute
Geophysical Research Division
P.O.Box 503, FIN-00101 Helsinki, Finland
mikhail.uspensky@fmi.fi

ABSTRACT. SuperDARN (DARN: Dual Auroral Radar Network) consists of the STARE VHF radar system in northern Scandinavia (STARE: Scandinavian Twin Auroral Radar Experiment), a northern-hemisphere longitudinal chain of nine phased array HF radars, which extends from King Salmon, Alaska (C) to Finland (F), and a southern-hemisphere chain of 6 identical HF radars, which extends from Halley Bay, Antarctica (H) to Tasmania, Australia (V). Both the northern and southern hemisphere

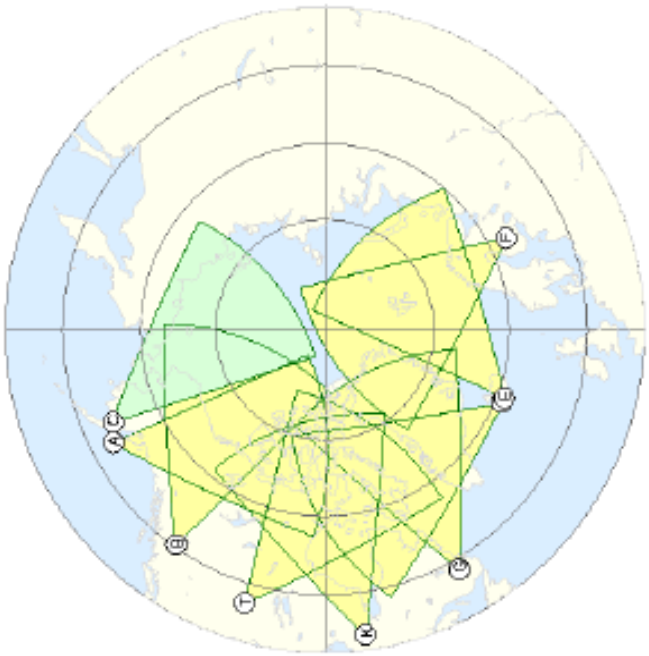

SuperDARN networks cover almost 180 degrees in longitude (see Figs) including the conjugate stations (H/G and P/F). The SuperDARN is widely used by the international community for studies of a global view of dynamical processes in the magnetosphere-ionosphere system, such as the structure and evolution of the global configuration of the convection electric field under changing IMF conditions. Other tasks contain a) substorm studies, b) MHD wave studies, c) ionospheric irregularity studies, d) gravity wave studies, e) high-latitude plasma structure studies f) HF propagation studies and g) analysis of co-ordinated, multi-instrumental satellite and ground-based experiments including an active modification of the ionosphere and magnetosphere.

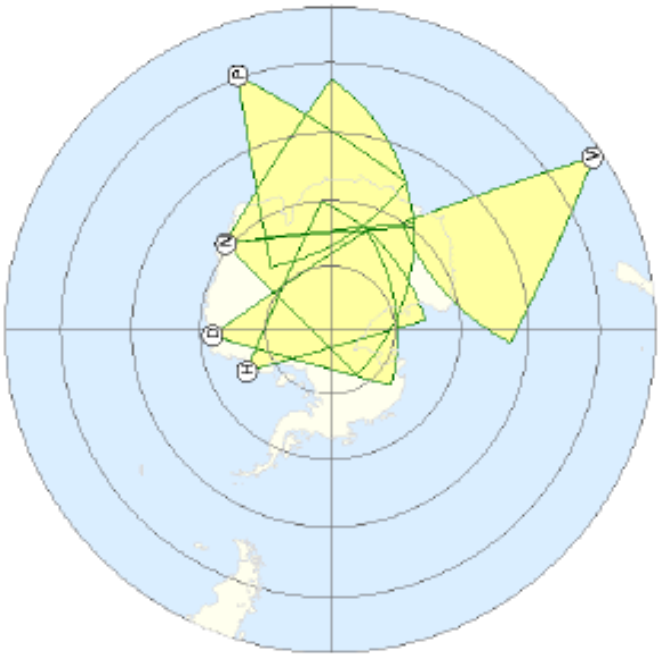

The report will illustrate how the SuperDARN radars can observe different magnetospheric and ionospheric phenomena. A short relevant instrumental description will be also given.

Greenwald, R.A., K.B. Baker, J.R. Dudeney, M. Pinnock, T.B. Jones, E.C. Thomas, J.-P. Villain, J.-C. Cerisier, C. Senior, C. Hanuise, R.D. Hansucker, G. Sofko, J. Koehler, E. Nielsen, R. Pellinen, A.D.M. Walker, N. Sato and H. Yamagishi, 1995: DARN/SUPERDARN. *Space Science Reviews*,**71**,761-796.

## LUOSTO: A NEW GENERATION WEATHER RADAR IN FINLAND

R. King, A. Huuskonen, K. Leminen and H. Kärki
Finnish Meteorological Institute
Observational Services
Sahaajankatu 20 E
FIN-00810 Helsinki, Finland
asko.huuskonen@fmi.fi

ABSTRACT. The Finnish Meteorological Institute is building its next Doppler weather radar on top of the Luosto mountain (67°8'19" N, 26°54'03" E, 514 m a.s.l.). The new radar will extent the present network of the 6 C-band Doppler radars to the northenmost part of Finland and will replace the only remaining non-Doppler X-band radar. The new radar will have features not found in the present FMI radars. These include a 6.1 m antenna and a transmitter driven by a solid state modulator, capable of forming any pulse length between 0.5 $\mu$s and 2.4 $\mu$s. The larger antenna gives a smaller beam width and a larger operational range, while the flexible modulator allows for a choice of the best operational pulse length. In the present radars only two fixed pulse lengths are available, namely a 2 $\mu$s pulse with a maximum PRF of 570 Hz and a 0.86 $\mu$s pulse with a maximum PRF of 1220 Hz. With the help of unfolding software, the first provides a sufficient velocity range in the Finnish climate conditions, but it is expected that pulse lengths between these two would provide a better overall quality for the measurements. The transmitter modulator allows one to change the pulse repetition interval from pulse to pulse. This opens up the possibility of using codes which are able to solve the long standing problem of weather radar measurements, the range-Doppler dilemma.

# FUTURE TRENDS IN SPACEBORNE RADAR TECHNOLOGY AND APPLICATIONS

Martti Hallikainen
Helsinki University of Technology
Laboratory of Space Technology
P.O. Box 3000, 02015 HUT, Finland
martti.hallikainen@hut.fi

ABSTRACT. Trends in the technology and applications of spaceborne radar for Earth Observation are reviewed, with the main emphasis in the development of synthetic aperture radar (SAR) sensors for various surface monitoring applications.

## TECHNOLOGY

The first western satellite SAR sensors were those onboard SEASAT (1978), ERS-1 (1991) and JERS-1 (1992) satellites, launched by the United States, European Space Agency (ESA) and Japan, respectively. The SEASAT SAR and JERS-1 SAR operated at L-band, whereas the ERS-1 SAR operated at C-band. Each sensor employed a single polarization and incidence angle and provided data over a maximum area of 100 km by 100 km. The SAR sensor, launched by Canada in 1995 onboard RADARSAT provides data using an incidence angle range of approximately 20 to 50 degrees off nadir and, consequently, a swath of up to 500 km.

The next generation of satellite SAR sensors will employ an incidence angle range of 20 to 50 degrees, multiple polarizations (VV, HH and VH/HV) and a number of operating modes providing data in various spatial resolutions and swaths. The ESA ENVISAT satellite is scheduled for launch in the summer/fall of 2001 and one of its main sensors is ASAR (C-band). The ASAR radar provides a swath of over 400 km using ScanSAR techniques. In the alternating polarization mode, the transmit and receive polarizations can be selected allowing scenes to be imaged simultaneously in two polarizations. Canada is planning a follow-on mission to RADARSAT (launch in 2003 or later) (C-band) with a maximum spatial resolution of three meters. Japan plans to launch PALSAR (L-band) with multipolarization capabilities. For several applications, including forest monitoring, L-band has been observed to be more useful than C-band, due to its better target penetration capabilities. It is worth noting that the United States has presently no firm plans to launch a SAR sensor in spite of its several multifrequency and multipolarization Shuttle SAR missions in the 1990 s. Recently, the United States operated a Shuttle SAR interferometry mission and covered most of the land surface between latitudes 60S and 60N. Analysis of these data is in progress.

The latest technology innovation is bistatic SAR that could use several small satellites to provide polarimetric and interferometric capabilities. Realization of the small satellite technology is independent of the launch and operation of the main satellite and can be added later.

## APPLICATIONS

Using spaceborne and airborne SAR data, several potential applications have been investigated, including monitoring of sea ice, snow, ocean waves, oils spills and forests. Canada has developed methods for sea ice monitoring in Arctic waters. Norway uses ERS SAR data operationally to monitor ships and oil spills near its coasts. Discrimination of oil from sea water is based on the change of backscatter intensity. Snow melt is presently monitored in Finland using both optical and SAR images. Inventory of forests using satellite SAR data is investigated in several countries; however, results so far have not been good enough for operational service. All these applications rely on using single-frequency and single-polarization data.

In the near future multi-polarization and multi-angle data will very likely improve the feasibility of radar for these applications. L-band data are not presently available for satellites, but the Japanese PALSAR sensor will operate at L-band and provide data suitable for forest monitoring. Even more feasible data will be available when multi-frequency SAR sensor data will become available.

Perhaps the most interesting data sets will be obtained from interferometric measurements. These data can be used to produce height information and to monitor land surface deformations.

# DEVELOPMENT OF NEW RADAR METHODS BASED ON MATHEMATICAL MODELLING OF RADAR CODING

Markku S. Lehtinen
University of Oulu
Sodankylä Geophysical Observatory
markku.lehtinen@sgo.fi

During the past 20 years, careful and rigorous mathematical modelling of the radar coding and target scattering processes combined with statistical inversion analysis and systematic optimization of the coding methods to minimize random fluctuations of the results have lead to a total revolution of the methods used in incoherent scatter radars both in EISCAT and other IS radars in the world. In addition to this, these new methods are now being applied to various other radar and sonar measurement applications, including weather radar, space debris radars and synthetic aperture sonars, meteorite radars, ionosondes, MST radars etc. All this is facilitated by development of a general–purpose hardware, which makes it possible to implement the new types of signal processing algorithms directly on modern general–purpose computers instead of traditional signal processors, which makes the implementation of these new kinds of methods both easier to program and achieves better throughput than what is possible with signal processors.

For these new applications, it has become necessary to rewrite the formulation of the theories in a more general setting – for example not directly referring to the space plasma as the scattering medium. In addition to this rather trivial modification, there are many new problems arising from the more or less differing nature of the problems in various new applications. Moreover, the modelling of the synthetic aperture situation is an even more fundamental expansion of the old theory, which we believe will eventually result in a similar revolution in remote sensing radars. The key mathematical idealization is the It'o integral representation of the random scatterer, one–dimensional in the traditional situations and two–dimensional in the new synthetic aperture modelling.

In this talk we mainly describe the goals of a new MaDaMe–funded project aimed at solving the mathematical radar measurement modelling problems. In addition to the applications mentioned above, the most ambitious goals include the solution of the problems occurring in measuring overspread targets in synthetic aperture radars and radar mapping of 'too fast' rotating planets, for example.

# THE EFFECT OF BIRD MIGRATION ON DOPPLER WEATHER RADAR MEASUREMENTS

Jarmo Koistinen
Finnish Meteorological Institute
Product Development
P.O.Box 503, FIN–00101 Helsinki, Finland
Jarmo.Koistinen@fmi.fi

ABSTRACT. The aim of this presentation is to describe the reflectivity and Doppler velocity properties of migrating birds. For more details see Koistinen (2000). Diagnosis and elimination of spurious atmospheric winds due to bird migration is important for real time wind monitoring and for the quality of the Doppler winds assimilated into numerical weather prediction models.

## BIRD MIGRATION AND WEATHER

The navigation, orientation and flying strategies of migrating birds vary much. In general wind at the cruising altitude (typically 0–5 km) is the most important meteorological factor for a migrating bird. They have to cope with windspeeds commonly ranging from 50 to 100 % of their normal airspeed in the boundary layer. Typical airspeed of birds is 7–20 m/s depending on the species involved. A bird migrating selectively during nights with following wind conditions speeds up its flight by 30 % on average compared to an individual disregarding the wind situation. Selecting the most profitable flight altitude may result in an additional gain of 40 % in flight speed. This strategy is clearly visible in weather radar measurements. Heavy migrations can be seen when the 10 m height wind speed is 0–8 m/s (calm to moderate breeze) and wind vector points towards the goal region of the migrants. In case of strong tailwinds the migration is too risky due to turbulence during the takeoff and large wind drift. The only other important limiting weather factor is visibility. The knowledge of the main migration types, their diurnal and seasonal distribution and the forcing by weather and local topography helps to diagnose the origin of the measured signals as birds.

## REFLECTIVITY PATTERNS OF MIGRATION

Birds and insects are biological targets, which can be easily detected with operational weather radar systems. Point echoes from solitary bird flocks can be easily distinguished from weather phenomena. However, in heavy migration individual flocks merge commonly into more widespread structures which resemble weather echoes. Meteorological data users may easily misinterpret the reflectivities and Doppler “winds” which migration generates.

Nocturnal or morning migration of small birds can be seen commonly as a circular or elliptic disc concentrated around the radar. The density can be e.g. 50–200 birds/km3 and typical reflectivities vary from –10 dBZe to +10 dBZe. It is quite similar to the reflectivity fields of shallow weak precipitation, drizzle or insect migration. Concentrations of large birds as streams of flocks generate sometimes local reflectivities of 20–50 dBZe. Major part of bird migration is so weak in terms of reflectivity that it has no significant effects on the accumulated precipitation products used in hydrological applications. Still, widespread weak “precipitation” due to intensive bird migration can irritate customers when they see that the sky is clear. The easiest way is to use a lower dBZe threshold (e.g. 10 dBZe) for accumulation products.

## DOPPLER MEASUREMENTS OF BIRDS

Doppler winds from insects represent reasonably accurately actual winds whereas birds have a much larger own velocity component. Thus the occurrence of bird migration introduces bias to atmospheric wind measurements, which can be fatal e.g. for the estimation of sensitive quantities like convergence. In the worst case automatic diagnosis packages interprete Doppler patterns from birds as dangerous weather phenomena, e.g. microbursts or low level jets. On the other hand, birds and insects may help in detecting meso–scale meteorological phenomena, especially lines of wind shear like sea–breeze and gust fronts.

Comparisons between the spectrum widths from precipitation and nocturnal migration during spring 2000 in Southern Finland revealed that from the spectrum width, based on Gaussian shape assumption, it is impossible to separate areas of rain, insects and birds. The real shapes of Doppler spectra and their time variations would certainly help in the diagnosis of the echo source at each individual measurement bin. On the other hand, automatic bird diagnosis based on the weak Gaussian coherency of the Doppler signal seems promising. Also the rms–difference between a linearly fitted VVP or VAD wind and the individual bin values is larger in bird migration than in rain or insect migration. Both of these quantities are effective in automatical quality thresholding.

## CONCLUSIONS

Diagnosis and elimination of bird migration from Doppler data is preferable. For a human analyst that is relatively easy but automatic detection is more demanding.

## REFERENCES

Koistinen, J., 2000: Bird Migration Patterns on Weather Radars. *Physics and Chemistry of the Earth*, 9 pp (in press).

# HELSINKI AND ITS SURROUNDINGS SEEN WITH MULTITEMPORAL INSAR

Marcus Engdahl
Laboratory of Space Technology
Helsinki University of Technology
mengdahl@avasun.hut.fi

ABSTRACT. Interferometric coherence is formed by correlating images in an interferometric SAR (INSAR) image pair. INSAR coherence contains information that is complementary to the scene information contained in SAR intensity imagery. This poster was formed using data from 28 ERS–1/2 SAR intensity images acquired during the ERS–1/2 Tandem mission in 1995–1996. 14 Tandem coherence images (temporal baseline 24 hours) were computed in addition to two INSAR coherence images with longer temporal baselines (35 and 240 days). A digital elevation model (DEM) was created from a linear combination of ERS–1/2 Tandem interferograms and a high quality orthorectified multitemporal interferometric data set was created for further study. Temporal averaging, i.e. incoherent averaging over several intensity and coherence images dramatically decreased noise, improved apparent resolution and increased the number of visually discernible features in the data set.

# THE USE OF SYNTHETIC APERTURE RADAR DATA ON MODELING OF FOREST CANOPY COVERED BY SNOW

***Ali Nadir ARSLAN*****(1)**, *Jarkko Koskinen(2), Jouni Pulliainen(2), Martti Hallikainen(2)*
*(1) Nokia Research Center, P.O.Box 407,FIN-00045 NOKIA GROUP,Finland*
*Phone (+358)-9-43761, Fax (+358)-9-43766067 E-mail: Ali.Arslan@Nokia.Com*
*(2) Helsinki University of Technology, Laboratory of Space Technology*
*P.O.Box 3000, FIN-02015 HUT,Finland*

The main problem with the forest canopy models is the complexity of the target. The more accurately the model includes the physical features of the target, the larger is the number of parameters needed. Empirical models typically have a substantially smaller number of parameters than theoretical models. Semi-empirical models can basically combine benefits of both modeling approaches. In this paper, a C-band semi-empirical backscattering model is presented for the forest-snow-ground system. The empirical SAR data used in the model were acquired by EMISAR of Technical University of Denmark over the city of Oulu in Northern Finland during EMAC 95 (European Multisensor Airborne Campaign-95). Airborne measurements were conducted on 22 and 23 March, on 2 and 3 May 1995. The total backscattering coefficient of the forested snow-covered ground is divided into two (incoherent) contributions which are given as follows,

$$\sigma^0 = \sigma_v^0 + t^2 \sigma_{bg}^0 \tag{1}$$

where $\sigma_v^0$ is the backscattering coefficient of the forest canopy, $\sigma_{bg}^0$ is the backscattering coefficient of the background, and $t^2$ is two-way transmissivity of the canopy.The canopy transmissivity is determined as a function of stem volume by analyzing the change observed in the backscattering contribution of the ground floor /ref: Nerijus: TGARS Nov. 99/. The backscattering coefficient of the forest canopy is expressed as a function of the stem volume and can be given as,

$$\sigma_v^0 = \frac{C}{-2.a}\left[-e^{2.a.V}\right] \tag{2}$$

where C is a constant coefficient (ha/m$^3$) and a is a transmissivity regression coefficient (ha/m$^3$).The backscattering coefficient of the background is modelled empirically and the empirical data is fitted with a linear expression :

$$\sigma_{bg}^0 = b_1.\text{swe} + b_2 \tag{3}$$

where $b_1$ and $b_2$ are constant coefficients and swe is the snow water equivalent of dry snow (mm). The coefficients were determined by the least square sum fitting of (3) to the measurement data as follows,

$$\sum_{i=1}^{N} \left(\sigma_{i,MEAS}^0 - \sigma_{i,MODEL}^0(swe, b_1, b_2)\right)^2 = minimum \tag{4}$$

where $N$ is the number of training sample plots of dry snow, $\sigma_{i,MEAS}^0$ is the measured mean backscatter for sample plot $i$ of dry snow and $\sigma_{i,MODEL}^0(swe, b_1, b_2)$ is the modeled backscatter for sample plot $i$ of dry snow.

The results showed that the semi-empirical model presented in this study is in good agreement with the experimental data. Correlation coefficients (R) between the model and data are 0.80 and 0.85 for co and cross polarizations respectively.

**EFFECTIVE PERMITTIVITY OF WET SNOW**

***Ali Nadir ARSLAN*****(1)**, *Wang Huining(2), Jouni Pulliainen(3), Martti Hallikainen(3)*
*(1) Nokia Research Center, P.O.Box 407,FIN-00045 NOKIA GROUP,Finland*
*Phone (+358)-9-43761, Fax (+358)-9-43766067 E-mail: Ali.Arslan@Nokia.Com*
*(2) Nokia Mobile Phones, P.O. Box 83 (Sinitaival 5) FIN-33721 Tampere,Finland*
*(3) Helsinki University of Technology, Laboratory of Space Technology, P.O.Box 3000, FIN-02015 HUT,Finland*

## ABSTRACT

In remote sensing applications, random media such as snow, vegetation canopy, soil are characterized by an effective permittivity that describes microwave propagation and attenuation in the media. The effective permittivity of snow is a function of frequency, temperature, volumetric water content, snow density, ice-particle shape and the shape of the water inclusions. Wet snow is assumed to consist of either dry snow and water, or of air, ice and water. The simple mixing models relate the effective permittivity of the mixture to the permittivities of the constituents (inclusions and host) well if the sizes of the inclusions are much smaller than the wavelength and if their shapes are known. The empirical models are also confined by the frequency. A summary of the semi-empirical dielectric models of wet snow is found in Hallikainen et al. The free water content of wet snow is an important factor in the calculation of the effective permittivity of wet snow. The shape of the water inclusions has to be considered. Jin and Kong used the strong fluctuation theory with the three-phase mixture approach (air, ice and water particles) to calculate the permittivity of wet snow. In their calculation, the inclusions are considered as spherical scatterers.

In this paper, wet snow is treated as a mixture, where water particles (inclusions) are embedded in dry snow (background material). The shape of the water inclusions is taken into account by using an anisotropic and azimuthally symmetric correlation function. The effective permittivity is calculated by using the two- and three-phase strong fluctuation theory model with symmetrical and non-symmetrical inclusions. The results are compared with the Debye-like semi-empirical model and the theoretical Polder-Van Santen mixing model. A comparison with the experimental data at 6, 18 and 37 GHz is also presented.The shape of the water inclusion is considered by using an anisotropic and azimuth symmetric correlation function. Now we consider dry snow as background medium which is a continuous random medium with permittivity $\varepsilon_b$ , and the water inclusion as scatterers with permittivity $\varepsilon_s$ . The fraction volume occupied by the scatterers is $f_v$ and the fraction volume occupied by the background medium is $1 - f_v$ . The permittivity of scatterers is $\varepsilon_s = \varepsilon_{water}$ and the permittivity of background is $\varepsilon_b = \varepsilon_{dry\_snow}$ .Effective permittivity tensor $\bar{\bar{\varepsilon}}_{eff}$ of the inhomogeneous medium is composed of a quasi-static part and a scattering effect part corresponding to the first and second terms, respectively, in the following expression :

$$\bar{\bar{\varepsilon}}_{eff} = \bar{\bar{\varepsilon}}_g + \varepsilon_0 \left[ \bar{\bar{I}} - \bar{\bar{\xi}}_{eff} \left\langle \bar{\bar{S}} \right\rangle \right]^{-1} \cdot \bar{\bar{\xi}}_{eff} \qquad (1)$$

where $\bar{\bar{I}}$ is the unit dyad, $\bar{\bar{\varepsilon}}_g$ is the auxiliary permittivity tensor, $\bar{\bar{S}}$ is the dyadic coefficient of the Dirac delta part in the dyadic Green s function of an anisotropic medium, and $\bar{\bar{\xi}}_{eff}$ is the effective dyadic scatterer.

# POLARIMETRIC SAR IMAGE CLASSIFICATION WITH NORMALIZED COHERENCY MATRIX

Jaan Praks
Helsinki University of Technology, Laboratory of Space Technology
P.O. Box 3000, FIN-02015 HUT, Finland
Jaan.Praks@hut.fi

ABSTRACT. In this paper some new parameters are proposed for using in polarimetric SAR image classification. It is shown here that using very simple invariants of power normalized coherency matrix (NCM), classification scheme similar to the entropy-alpha classification can be established. Classification results for a example image differ for 3% of pixels. Proposed method makes it possible to use established polarimetric classification even in image processing software.

## ENTROPY ALPHA CLASSIFICATION SCHEME

Classification scheme of fully polarimetric SAR image based on polarimetric properties of radar targets was proposed by *Cloude and Pottier* (1997). Proposed classification is based on two parameters, scattering randomness (called target entropy) and scattering mechanism (called alpha angle). Parameter space formed by alpha and entropy is divided into nine categories based on character of scattering as presented in Figure 1 a). Both parameters are calculated using eigenvalues and eigenvectors of target average coherency matrix. Calculating of eigenvectors and eigenvalues of complex matrices employs complicated algorithms. This classification is not directly applicable in the standard image processing software packages.

## NORMALIZED COHERENCY MATRIX BASED CLASSIFICATION SCHEME

Here it is proposed an alternative classification algorithm based on the simple invariants of normalized coherency matrix (NCM) proposed by *Praks and Hallikainen* (2000). As shown by Praks and Hallikainen, first element of the NCM is closely related to the alpha angle and sum of squared elements of the NCM is related to the target entropy. These parameters form very similar parameter space to the alpha-entropy space as shown in Figure 1 b). However, parameters are related to entropy and alpha with some ambiguity and classification results differ slightly from entropy-alpha classification. Proposed parameters can be easily calculated with image processing software if polarimetric data is given in covariance matrix (or comparable) format. Calculations employ only linear combinations of absolute values of the NCM elements.

## CLASSIFICATION OF EXAMPLE IMAGE

As an example, NASA/JPL AIRSAR L-Band image for the San Francisco bay was classified with both algorithms. Size of the used image was 224 x 256 pixels. Both algorithms classified 97 % of pixels into corresponding classes. Misclassification rate of Sum-N1 classification compared to the entropy-alpha classification for each class is presented in table 1. Highest misclassification rates are for high entropy classes. Misclassification rate for most classes is less than 10 %.

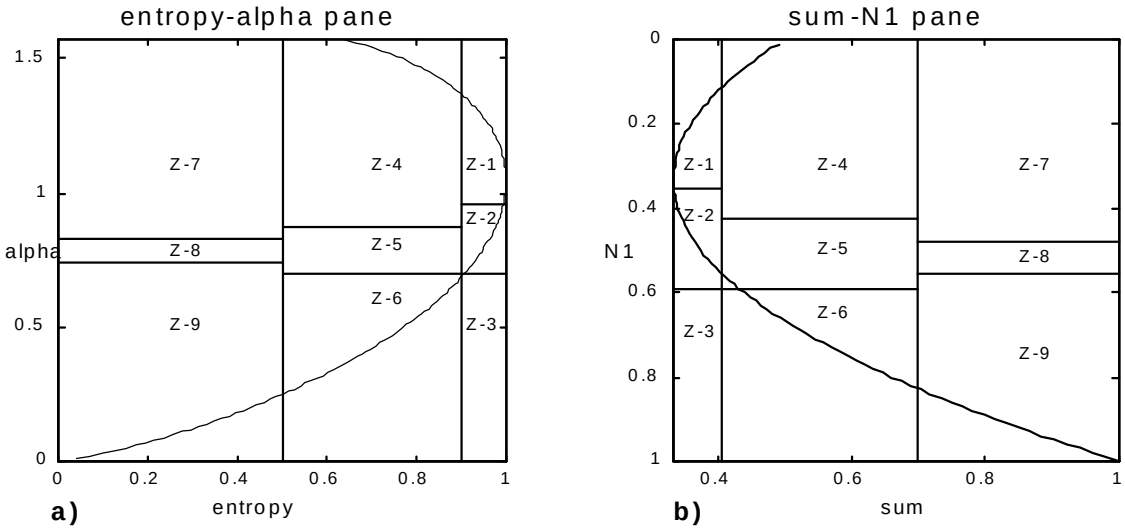


Figure 1. *a) Entropy-alpha parameter space with classification boundaries. Zone 9: Low Entropy Surface Scatter, Zone 8: Low Entropy Dipole Scattering, Zone 7: Low Entropy Multiple Scattering Events, Zone 6: Medium Entropy Surface Scatter, Zone 5: Medium Entropy Vegetation Scattering, Zone 4: Medium Entropy Multiple Scattering, Zone 3: High Entropy Surface Scatter (not measurable), Zone 2: High Entropy Vegetation Scattering, Zone 1: High Entropy Multiple Scattering.*
*b) Sum-N1 parameter space with classification boundaries. Classes correspond approximately to entropy-alpha classification classes.*
*Note that allowed values for both parameter pairs are inside the curved line.*

Table 1. *Percentage of pixels classified into wrong classes by NCM based classification compared to entropy-alpha classification.*

| Z-1 | Z-2 | Z-4 | Z-5 | Z-6 | Z-7 | Z-8 | Z-9 | All Classes |
|---|---|---|---|---|---|---|---|---|
| 10 % | 12 % | 3 % | 3 % | 5 % | 6 % | 7 % | 0.3 % | 3 % |

## CONCLUSION

Simple and fast classification scheme for polarimetric SAR images is presented. Method is suitable for using as fast approximation for the entropy-alpha classification or independent classification scheme. Presented method uses only absolute values of coherency matrix elements and thereby it is applicable in advanced image processing software.

## REFERENCES

Cloude, S. R., E. Pottier, 1997: An Entropy Based Classification Scheme for Land Applications of Polarimetric SAR, *IEEE Trans. Geosci. Remote Sensing*, vol 35, pp. 68-78, Jan. 1997.

Praks, J., M. Hallikainen, 2000: A Novel Approach in Polarimetric Covariance Matrix Eigendecomposition, *Digest IEEE International Symposium on Geoscience and Remote Sensing (IGARSS'2000)*, Honolulu, USA

# Turbidity Detection Using AVHRR Satellite Imagery in the Gulf of Finland

Yuanzhi Zhang, Sampsa Koponen, Jouni Pulliainen, and Martti Hallikainen
Helsinki University of Technology, Laboratory of Space Technology
P.O. Box 3000, 02015 HUT, Finland
zhang@avanet.hut.fi

**Abstract - This paper presents turbidity change detection using AVHRR satellite imagery in the Gulf of Finland. AVHRR imagery is evaluated as a potential data source for monitoring light attenuation, as a measure of turbidity.**

## INTRODUCTION

The Gulf of Finland is highly effected by the input from the rivers which have a high concentration of mineral suspended solids and nutrients. Optically, the Gulf of Finland is dominated by scattering from suspended sediments, whereas the coastal waters of the Gulf are dominated by absorption from both dissolved and particulate organic matter. Although AVHRR imagery can provide a synoptic turbidity information of coastal waters, its quantitative use is still a difficult task in this study.

## METHODOLOGY

Satellite remote quantification of light attenuation has focused on oceanic regions due to the relative optical simplicity of oceanic waters and the availability of Coastal Zone Color Scanner (CZCS) data in the past. Light attenuation in oceanic waters is primarily related to phytoplankton pigments and their derivative products. However, Light attenuation in coastal waters is greater optical complexity in the form of inorganic particulates, and a greater variety and higher concentration of dissolved and particulate organic matter which result from significant quantities of terrigenous materials.

There are two main methods to derive water quality parameters. One is the use of empirical algorithms derived from remotely sensed reflectance data. They can provide site-specific predictions of water quality parameters with reasonable accuracy, but are limited in their universal application. The other approach is the use of analytic inversion models that employ solutions to the radiative transfer equation for deriving absorption and scattering coefficients. The latter approach allows remote sensing measurements to be understood in terms of the inherent optical properties, and provides insight into the characteristics of the effectiveness and significance of differences in algorithm coefficients in various regions (Woodruff *et al.,* 1999). Figure 1 shows an example map of turbidity change detection using empirical algorithms from AVHRR satellite imagery in the Gulf of Finland.

Satellite remote sensing observations are also effected by the atmosphere and radiation from the direct reflectance due to the water surface. These effects must be removed

with suitable atmospheric correction and bidirectional reflectance models before data analysis.

## FURTHER STUDY

This study is still in process, and we will present further applications of turbidity algorithms, define geographic limitation of the model within our study area based on optical characteristics of the water, and examine variations over time. Furthermore, the AVHRR has particular utility with respect to recent and near-future sensors such as SeaWiFS and permits to be integrated into the future.

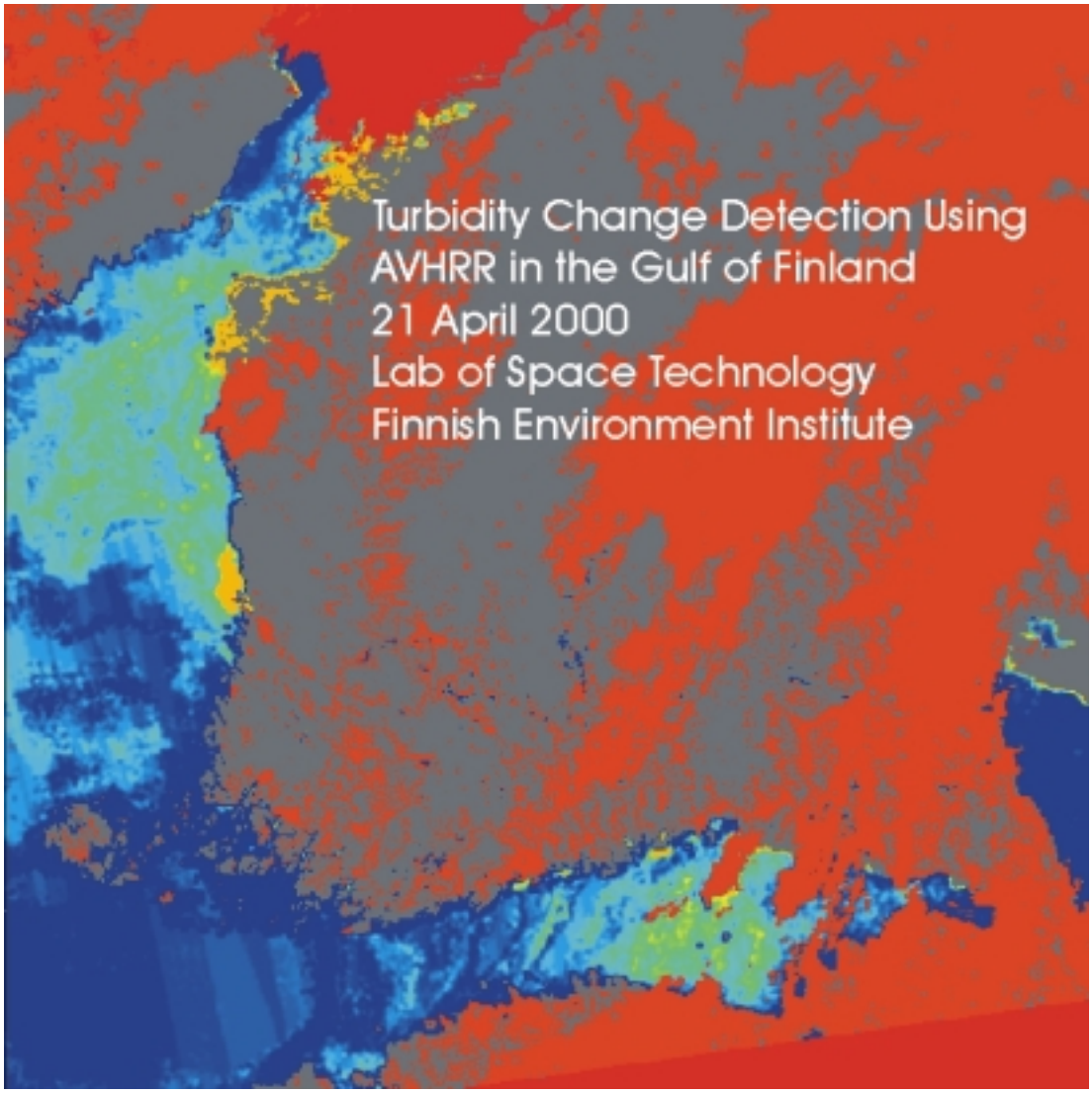


Figure 1: Turbidity change detection using AVHRR imagery in the Gulf of Finland

## REFERENCES

Woodruff, D. L., Stumpf, R. P., Scope, J. A. and Paerl, H. W., 1999: Remote estimation of water clarity in optically complex estuarine waters. *Remote Sensing of Environment,* **68,** 41-52.

# Electromagnetic theory

# LOW LOSS DIELECTRIC WAVEGUIDES AT 75-110 GHZ FREQUENCY RANGE

Sergey Dudorov[1], Dmitri Lioubtchenko[1], Juha Mallat[1], Jussi Tuovinen[2], Antti V. Räisänen[1]
[1]Helsinki University of Technology, Radio Laboratory, P.O. Box 3000, 02015 HUT, Espoo, Finland
[2]MilliLab, VTT Information Technology, Espoo, Finland
sdudorov@cc.hut.fi

ABSTRACT**.** The problems of single-mode metal waveguide applications at the frequency above 75 GHz are due to increasing losses when the frequency increases. The dielectric waveguides are promising to be used instead of metal ones due to low propagation losses. The dielectric waveguides should have extremely low propagation losses at high frequencies if made of monocrystalline materials. However the experimental performance and matching with metal waveguides are problematic.

In this work we present computer simulation and experimental results of Dielectric Rod Waveguide (DRW) made of single crystal sapphire. Simple tapering was used for the waveguide matching (Fig.1). However, different tapers give different results [1-3]. The simulation results show that tapering in *E*-plane is better for matching with.

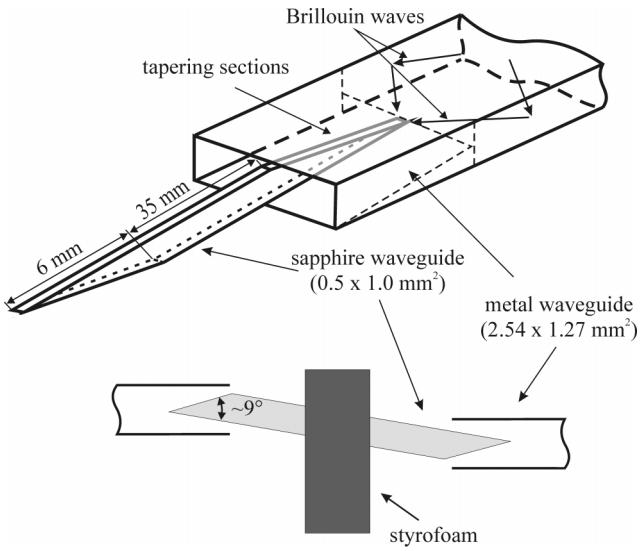


Figure 1. Experimental setup.

Single mode rectangular dielectric waveguides with cross section of 0.5x1.0 $mm^2$ with refractive indexes 3.0 (sapphire) and 3.41 (silicon) were simulated. It was found that in spite of small aperture overlapping, good transmission characteristics are obtained (better than 20 dB for return loss and 0.16 dB (for two transitions) for the insertion loss). The simulation results are shown in Fig. 2.

The experimental results for monocrystalline sapphire DRW in the frequency range of 75-110 GHz are shown in Fig. 3. It can be seen that the standard metal waveguide

section has an insertion loss of 0.4-0.55 dB while the sapphire one has it mainly between 0.1 and 0.3 dB and sometimes even near 0.05 dB. From 98 GHz upwards the losses increase and decrease approximately between 100-103 GHz. This can be explained by difficulties of the excitation occurring due to tapering sections, which are non-symmetrical with respect to the optical axis of the DRW. The discrepancy of $S_{21}$ curves (Fig. 3a) for three different DRW might be due to their small non-identities.

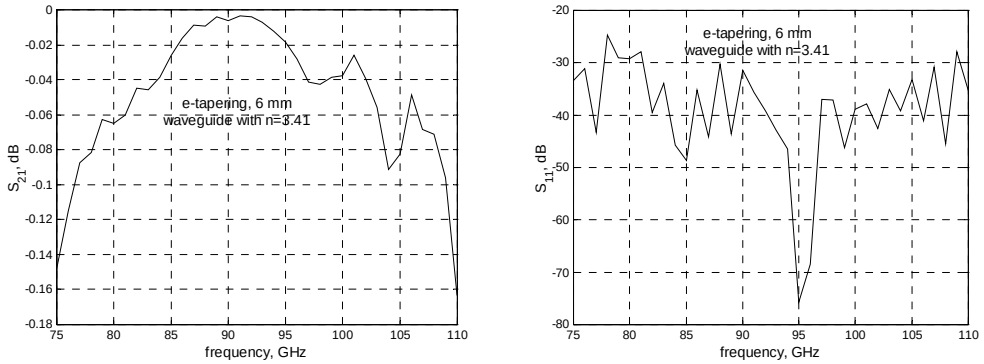


Figure 2. S-parameters simulation for a silicon waveguide with tapering in E-plane.

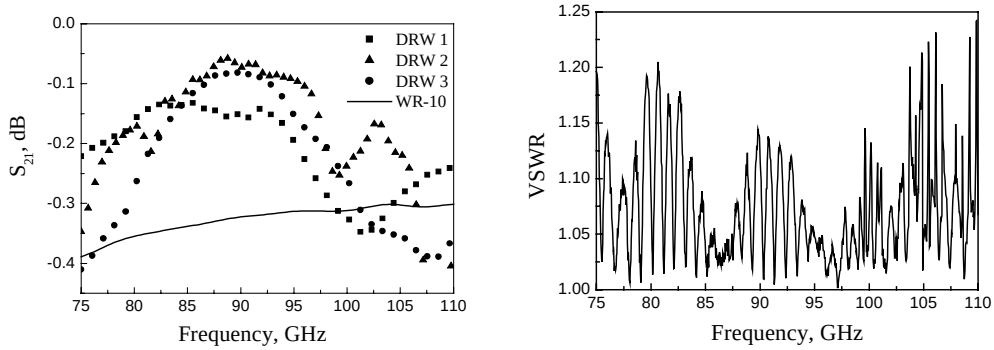


Figure 3. Transmission characteristics of 3 different sapphire waveguides.

In conclusion, we can say that the DRW with high permittivity has low loss and can be well matched with a single-mode metal waveguide (Fig. 3).

REFERENCES

[1] J.A. Paul, Y.C. Chang, “Millimeter-wave image-guide integrated passive devices”, *IEEE Transactions on Microwave Theory and Techniques*, **MTT-26**, no. 10, October 1978

[2] T.N. Trinch, R. Mittra, “Transitions from metal to dielectric waveguide”, *Microwave Journal*, November 1980, pp. 71-74

[3] H. Jacobs, M. Chrepta, “Electronic phase shifter for millimeter- wave semiconductor dielectric integrated circuits”, *IEEE Transactions on Microwave Theory and Techniques*, **MTT-22**, no. 4, April 1974

# LOW-LOSS BIAS-T FOR 4–15 GHz

Ville S. Möttönen, Petri Piironen, and Antti V. Räisänen
Radio Laboratory, Helsinki University of Technology
P.O.Box 3000, FIN-02015 HUT, Finland
Email: Ville.Mottonen@hut.fi

ABSTRACT – A low-loss and well-matched wideband (4–15 GHz) coaxial bias-T is presented. Test results demonstrate the low-loss performance of the bias-T. The measured return loss is better than 30 dB and the insertion loss is close to 0.1 dB over a wide frequency range.

## INTRODUCTION

In many applications, bias-Ts are needed to provide an active component with a proper DC operation point while not affecting the RF performance. Although bias-Ts often are integrated with the main circuit, they are also desirable as separate components, especially, in test assemblies. Wideband bias-Ts have been designed to cover microwave frequencies over a decade bandwidth [1]. However, some applications require lower losses with good matching. We designed and constructed a low-loss coaxial bias-T for testing of the noise properties of millimetre and submillimetre wave planar diodes and mixers.

## DESIGN

The design method of the bias-T is based on the idea used in constructing microstrip and stripline bias-Ts in [1]. Fig. 1 shows the equivalent circuit of the bias-T. The capacitors *C1* and *C2* perform as a high-pass and low-pass filter, respectively, as in usual bias-T designs. Wideband operation is achieved by using a band-pass filter consisting of successive quarter-wavelength transmission lines with a quarter-wavelength short-circuited high-impedance stub connected to the center. The bandwidth depends on the impedance of the stub and on the number of the transmission elements while the centre frequency is determined with the length of the stub and transmission lines.

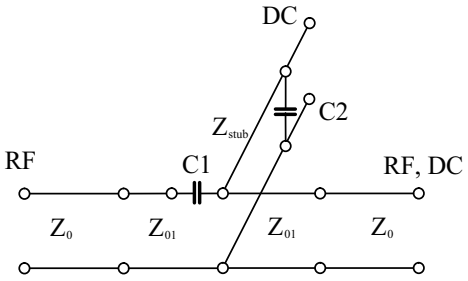


Figure 1. Equivalent circuit of the bias-T.

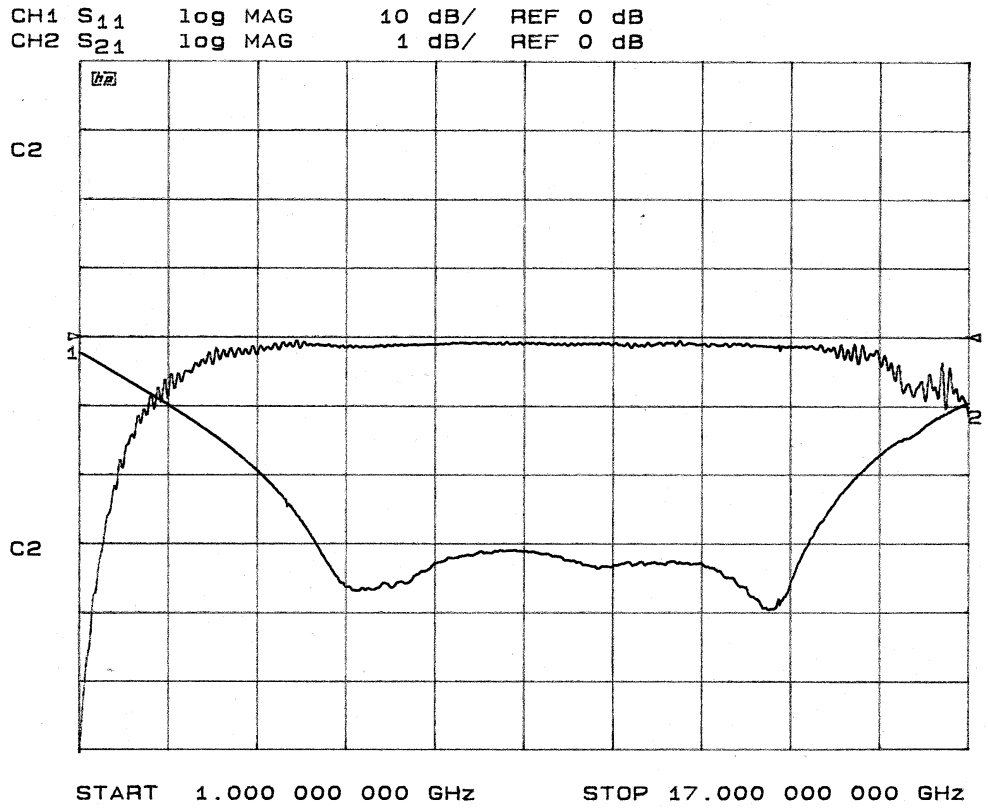


Figure 2. Measured reflection and transmission parameters of the bias-T.

## EXPERIMENTAL RESULTS

The coaxial bias-T was constructed of drilled and milled brass blocks and of three SMA connectors. The band-bass filter comprises two 45 Ω coaxial lines (air dielectric) with a 150 Ω stub in shunt. Short 50 Ω lines are used at the input and output ports for a good support and alignment of the connectors. RF and DC blockings are done with small plate capacitors.

The reflection and transmission parameters were measured with an HP 8722C network analyser. The parameters are plotted in Fig. 2. The return loss is better than 30 dB from 5.2 to 14.1 GHz and better than 20 dB from 4.2 to 15 GHz, respectively. The insertion loss is 0.1 dB over a wide frequency range. The insertion loss can be reduced further by using a metal or metal plating with higher conductivity. The measured RF isolation at the DC port is more than 30 dB over the full band.

## REFERENCES

[1] B. J. Minnis, “Decade bandwidth bias T’s for MIC applications up to 50 GHz,” *IEEE Trans. Microwave Theory Tech.*, Vol. MTT-35, No. 6, 1987, pp. 597–600.

# TRANSMISSION OF DVB-T SIGNAL OVER CABLE TV NETWORK

*Ali Hazmi, Jukka Rinne and Markku Renfors*
Tampere University of Technology
Telecommunications Laboratory
P.O.Box 553, FIN-33101 Tampere, Finland

h161966@cs.tut.fi

## ABSTRACT

In this paper, we study the quality of the terrestrial digital video broadcasting (DVB-T) transmission over the cable TV network. Generally, when terrestrial digital TV signals are distributed in the cable TV a conversion is needed in the head-end, from DVB-T (OFDM) to DVB-C (single carrier). In this work we show that it is possible to use the DVB-T signal without any conversion. At first, a simple model for the channel is designed taking into account the main impairments. Secondly, the performance of the DVB-T signal is simulated and compared to the that of digital cable TV standard DVB-C which is based on single carrier technique. The comparison is based on the useful bit rate that each system can achieve, with the same bit error rate. A channel interference problem is also simulated. Some limitations for the two systems are finally examined.

## 1. INTRODUCTION

Digital video broadcasting is rapidly replacing analog communications technology and recent research has allowed the concept of digital television broadcasting to be implemented. Such systems are already operating on satellite [3] and cable systems [2] around the world. Single carrier techniques are used in these systems.

In our days, a conversion from DVB-T to DVB-C is needed in the head-end to be able to transmit the terrestrial TV signals in the cable TV. This conversion affects the quality of the transmitted signal and increases the expenses.

The non linearity introduced by the earlier conversion, and the complexity of using adaptive time-domain equalization in the case of single carrier compared to the simple frequency equalization in the case of OFDM systems, motivates us to study the performance of the DVB-T COFDM signal over CATV network and make a comparison with the single carrier system. In the next section, simple DVB-C model for the CATV channel is developed. In the third section we briefly recall the principle of the DVB-T COFDM. The fourth section will concentrate on the single carrier technique used to transmit signals over the cable channel. In the fifth section, the performances of the two systems are compared. Finally, some requirements and specifications of the two techniques are examined.

## 2. THE CABLE TV CHANNEL MODEL

The impairments that affect the transmitted TV signal due to the CATV channel can be classified in three main parts:

***a)*** ***Linear distortion:*** It is caused by the frequency dependent attenuation of the cable, which is not fully compensated by the amplifiers. It is possible to model this part with an FIR filter where the order and the coefficients are carefully chosen taking into account the linear distortion. In our simulation model the echo profile of the NORDIC specification is considered [4]. It is suggested that 5 echoes should be present simultaneously.

***b)*** *Nonlinear distortion*: The amplifier components constitute the main source of nonlinear distortion [6]. In frequency domain, the intermodulation can be viewed as interference problem where the interfering signals occur almost on the carrier frequency of the useful signal with low level. . Based on [5] this can be modeled simply as an intermodulation interference, the level of which is at least 57 dB below the main carrier.

***c)*** ***Additive White Gaussian Noise***: It is mainly due to thermal noise that is inevitable in any communication systems.

A simplified model of the channel consists of the cascading of nonlinear amplifiers and linear echo channels. In all decent CATV networks, the delayed components are well below the main component and appear at the time as a small variation around the ideal signal. Therefore, it is sufficient to include in the model one nonlinear amplifier and one echo channel stage. Finally, we end up in the simplified model of Fig 1

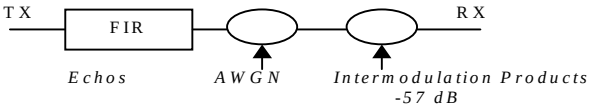


Fig. 1: Simplified simulation model.

## 3. COFDM BASED DVB-T SYSTEM

The system is based on the use of COFDM. The choice of the transmission system and the detailed parameters has been made after careful consideration and testing. The basic parameters of the DVB-T system in 2k and 8k modes are summarized in [1]

## 4. SINGLE CARRIER BASED DVB-C IN CABLE TV NETWORK

The DVB-C is using a single carrier technique based on Quadrature Amplitude Modulation (QAM). Table 1 gives examples of useful bit rates Ru for transparent re-transmission and spectrum efficient use on cable networks [2].

Table 1: Bit rates for DVB-C (Mbits/s)

| Ru (Mbit/s) | Cable symbolrate (Mbaud) | Occupied bandwidth (MHz) | Modulation scheme |
|---|---|---|---|
| 38.1 | 6.98 | 7.92 | 64-QAM |
| 25.2 | 6.84 | 7.86 | 16-QAM |

## 5. SIMULATION RESULTS AND DISCUSSION

The channel for both systems is our CATV model, where we varied the noise variance. The bit error rate is simulated for each system and for different constellations (16-QAM 64-QAM). The results are shown in Fig. 2. As we can observe, the DVB-T based on COFDM has better performance compared to the DVB-C system, for the same constellation. It can be also mentioned that DVB-T/64QAM and DVB-C/16QAM have almost the same performance.

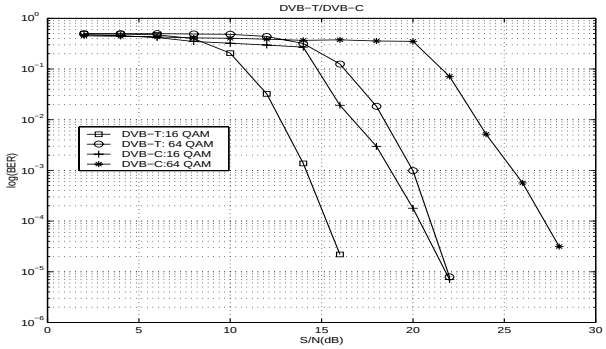


Fig. 2: BER performance.

DVB-T is using convolutional coding and DVB-C not, the bit rate performance of DVB-C (Table 1), is then higher for the same channel bandwidth. Even when we increase the code rate, we cannot achieve the same useful bitrate. To achieve almost the same performance we need to use larger constellation. 64-QAM in DVB-T with a code rate of 3/4 and a guard interval of 1/8 for example can almost assure the same performance in bit rate point of view as 16-QAM for DVB-C system (25.2 Mbits/s for DVB-C and 24.88 Mbits/s for DVB-T).

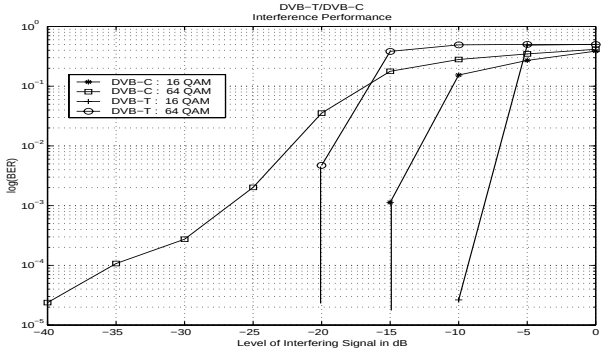


Fig. 3: Interference Performance

The effect of increasing the interfering signal level is also simulated. We have in the Fig. 3 the BER with respect to the level of the interfering signal in dB below the main carrier level, for the both systems and for different constellations. As it can be observed, even when we increase the level of the interfering signal from –57 dB to –30 dB below the main carrier level, we assure good performance in BER rate for the two systems. Only the DVB-C/64 QAM is more sensitive to interference.

## 6. CONCLUSION

In this paper, the aim was to show that DVB-T signal could be transmitted over cable TV without any conversion. For that a performance comparison was carried out for the two different systems: DVB-T based on COFDM and DVB-C based on single carrier technique. We started by building a model for the channel, and then a simulation of BER for the two systems was carried out. It was shown that the DVB-T system has best performance than the DVB-C in BER rate point view. But, larger constellations are needed to have the same useful bit rate that DVB-C system can assure in the same channel bandwidth. It was also shown that the specifications of the nonlinear amplifier can be relaxed, and a level of –20 dB of interfering signal is tolerated having almost the same performance in BER for the different systems. Except for the case of 64-QAM single carrier system, witch is more sensitive to interference, at most –30dB is tolerated.

## REFERENCES

[1] ETSI, Digital Video Broadcasting (DVB); Framing structure, channel coding and modulation for Terrestrial television, ETS 300 744 March 1997.

[2] EN 300 429 Digital Video Broadcasting (DVB); Framing structure, channel coding and modulation for cable system. (1997-08).

[3] ETS 300 421 Digital Video Broadcasting (DVB); Framing structure, channel coding and modulation for 11/12 GHz satellite services.

[4] NorDigI, Digital Integrated Receiver Decoder Specification For use in cable, satellite and terrestrial networks. Web page: http:// www.svt.se/nordig/download.htm

[5] EN 50083-7 Cabled Distribution Systems for Television and Sound Signals: System Performance April 1996.

[6] M. Moeneclaey and M.V. Bladel, “Digital HDTV Broadcasting Over the CATV Distribution system, “, Signal Processing Image Communication 5 pp405-415, 1993.

# CHIRAL SOFT AND HARD SURFACE WAVEGUIDE MODE TRANSFORMERS

Ari Viitanen
Electromagnetics Laboratory
Department of Electrical and Communications Engineering
Helsinki University of Technology
P.O. Box 3000, FIN-02015 HUT, Finland
ari.viitanen@hut.fi

ABSTRACT. Mode transformer for soft and hard surface waveguides is studied. The mode transformation effect is achieved by using chiral material inside the waveguide. For small chirality parameter values the circularly polarized eigenfields are slightly coupled and the polarization of the propagating field is changed.

## INTRODUCTION

The special corrugated surfaces, called as soft and hard surfaces, have a lot of applications in microwave engineering *Kildal* (1990). For example, the eigenwaves inside soft and hard surface waveguides are circularly polarized. Also the eigenwaves inside chiral medium are circularly polarized. In this study field propagation in cylindrical soft and hard surface waveguides filled with chiral material is considered. When the corrugation on the boundary of the waveguide is in axial direction the surface is called hard and when the corrugation is in transverse direction the surface is called soft *Kildal* (1990). It is shown that the polarization of the propagating field is changed in hard surface waveguides filled with chiral material *Viitanen* (2000). This effect can be used for mode transformation of the propagating mode. This similar mode transformation effect is also found in soft surface waveguides for certain propagating modes. The required chirality for mode transformation effect is very small which makes this kind of application practically interesting since slightly chiral materials are easier to manufacture than materials with high chirality parameter values. Chiral material can be fabricated incerting small helices into the base material. Generally, this kind of matrix is dispersive and lossy. The value of the chirality parameter is proportional to the density of chiral inclusions which is small in this case and the material is almost lossless *Mariotte et al.* (1994), *Lindell et al.* (1994).

## THEORY

The time harmonic, $e^{j\omega t}$-dependent fields are considered and the fields inside the waveguide depend on $z$ as $e^{-j\beta z}$ where $\beta$ is the propagation factor. The waveguide is filled with chiral material with the constitutive relations *Lindell et al.* (1994)

$$\mathbf{D} = \epsilon\mathbf{E} - j\kappa\sqrt{\mu_o\epsilon_o}\,\mathbf{H}, \qquad \mathbf{B} = \mu\mathbf{H} + j\kappa\sqrt{\mu_o\epsilon_o}\,\mathbf{E}, \tag{1}$$

where $\epsilon$, $\mu$ and $\kappa$ are permittivity, permeability and chirality parameter of the material, respectively. The fields are written with transverse and axial parts, inserted

into the Maxwell equations and the transverse fields are eliminated. Using the decomposition into circularly polarized fields denoted by + and − parts, the Maxwell equations reduce finally to the Helmholtz equation for the axial partial fields

$$[\nabla_t^2 + k_{c\pm}^2]E_{z\pm}(\rho,\varphi) = 0, \tag{2}$$

where $E_{z\pm} = \frac{1}{2}(E_z \mp j\eta H_z)$, $k_{c\pm} = \sqrt{k_\pm^2 - \beta^2}$, $k_\pm = k(1 \pm \kappa_r)$ and $\kappa_r = \kappa\sqrt{\frac{\mu_o\epsilon_o}{\mu\epsilon}}$. The $\nabla_t$ is the transverse part of $\nabla$ and $k = \omega\sqrt{\mu\epsilon}$. The solutions of the Helmholtz equation are Bessel functions of the first kind with index $n$. The parameters $k_{c\pm}$ are determined by the boundary condition for the soft and hard surface

$$\mathbf{u}\cdot\mathbf{E} = 0, \qquad \mathbf{u}\cdot\mathbf{H} = 0, \tag{3}$$

where $\mathbf{u} = \mathbf{u}_\varphi$ for soft surface and $\mathbf{u} = \mathbf{u}_z$ for hard surface boundary. For soft surface waveguide with index $n = 0$ and for hard surface waveguide with any index value the parameter $k_{c\pm} = p_{ns}/a$ where $p_{ns}$ are zeros of the Bessel function. This results in two separate propagating waves. When the medium inside the waveguide is slightly chiral, i.e., $|\kappa_r| \ll 1$, these two waves, + and − fields, are propagating almost with the same propagation factor. Because the difference between the propagation factors is small the most importante effect is seen in the phase factors of the total propagating field.

Finally the axial field components inside the waveguide are obtained

$$E_z(z) = [E_n\ \cos(\frac{k^2}{\beta}\kappa_r z) - \eta H_n\ \sin(\frac{k^2}{\beta}\kappa_r z)]J_n(k_c\rho)e^{jn\varphi}e^{-j\beta z}, \tag{4}$$

$$H_z(z) = [H_n\ \cos(\frac{k^2}{\beta}\kappa_r z) + \frac{E_n}{\eta}\ \sin(\frac{k^2}{\beta}\kappa_r z)]J_n(k_c\rho)e^{jn\varphi}e^{-j\beta z}. \tag{5}$$

The coefficients $E_n$ and $H_n$ are determined by the initial condition. It is seen that the axial field configuration depend on $z$. For example, if at $z = 0$ the coefficient $H_n = 0$, there is $TE_{ns}$ field inside the waveguide. At distance $z = \pi\beta/2k^2\kappa_r$ there is only magnetic axial field component, i.e., $TM_{ns}$ field. Considering the fields in terms of $TE$ and $TM$ modes the phase difference between the eigenwaves is seen as a mode transformation between $TE$ and $TM$ fields, i.e., $TE$ mode is transformed to $TM$ mode and vice versa. Also the wave impedance is changed thus making this component as a matching element between different kind of waveguides.

REFERENCES

Kildal, P-S., 1990: Artificially soft and hard surfaces in electromagnetics. *IEEE Trans. Microwave Theory Tech.* **38**, No. 10, 1537-1544.

Viitanen, A., 2000: Chiral hard-surface waveguide mode transformer. *IEEE Trans. Microwave Theory Tech.* **48**, No. 6, 1077-1079.

Mariotte, F., S. Tretyakov and B. Sauviac, 1994: Isotropic chiral composite modeling: Comparison between analytical, numerical, and experimental results. *Microwave and Optical Technology Letters,* **7**, No. 18, 861-864.

Lindell, I., A. Sihvola, S. Tretyakov and A. Viitanen, 1994: *Electromagnetic Waves in Chiral and Bi-Isotropic Media.* Norwood, NY: Artech House.

# ONSAGER-CASIMIR PRINCIPLE AND RECIPROCITY OF COMPLEX COMPOSITE MEDIA

Sergei Tretyakov and Ari Sihvola
Electromagnetics Laboratory
Helsinki University of Technology
P.O. 3000, FIN-02015 HUT, Finland
sergei.tretyakov@hut.fi ari.sihvola@hut.fi

ABSTRACT. In this presentation we discuss relation between the microscopic and macroscopic Onsager–Casimir principles. It is demonstrated that because of certain symmetries with respect to the space reversal operation, which are intrinsic to any form of the linear constitutive relations, it follows that the symmetries under time reversal expressed by the Onsager–Casimir principle are valid both on the microscopic and macroscopic levels. As one of the possible applications we show that the property of the general bi-anisotropic media to be reciprocal or non-reciprocal does not depend on the constitutive formalism.

## THEORY

In the electromagnetic theory there is a well-established *Onsager–Casimir principle* or *the principle of the symmetry of kinetic coefficients* which provides certain symmetry relations for microscopic polarizabilities and macroscopic constitutive parameters. The principle is based on the time-reversal symmetry properties of electromagnetic processes. In this paper we show that quite general and important conclusions can be drawn from the fact that microscopic and macroscopic electromagnetic processes possess both time-reversal symmetry (manifested in the Onsager-Casimir principle) and space-reversal symmetry. The latter is manifested by the fact that linear constitutive relations can connect quantities of different mathematical nature. For example, electric polarization is an even vector with respect to the space-reversal operation *(polar vector)*, but magnetic field is odd under this operation *(axial vector)*. Thus, the polarizability coefficient must possess certain mathematical properties, so that operation on an axial vector gives a polar vector. We consider the two symmetry principles dictated by the time-reversal symmetries and space-reversal symmetries together. In particular, we find that the space-inversion symmetry imposes certain restrictions on the mixing rules which connect microscopic and macroscopic parameters of electromagnetic systems. As one of the applications, we consider the Onsager–Casimir principle for the material parameters of bi-anisotropic media. We show that the Onsager–Casimir principle leads always to the same conclusions in all possible formal descriptions of bi-anisotropic media. In particular, if a medium is seen to be reciprocal in one set of material parameters, it is found to be reciprocal in any other set.

On the microscopic level a small bi-anisotropic particle is described by linear relations between the induced electric $\mathbf{p}_e$ and magnetic $\mathbf{p}_m$ dipole moments and external

electric $\mathbf{E}$ and magnetic $\mathbf{B}$ fields (in the frequency domain):

$$\mathsf{p} = \mathsf{A} \cdot \mathsf{e} = \begin{pmatrix} \overline{\overline{a}}_{ee} & \overline{\overline{a}}_{em} \\ \overline{\overline{a}}_{me} & \overline{\overline{a}}_{mm} \end{pmatrix} \cdot \mathsf{e}, \quad \text{where} \quad \mathsf{p} = \begin{pmatrix} \mathbf{p}_e \\ \mathbf{p}_m \end{pmatrix}, \quad \mathsf{e} = \begin{pmatrix} \mathbf{E} \\ \mathbf{H} \end{pmatrix} \tag{1}$$

The Onsager-Casimir relations for the polarizabilities read:

$$\overline{\overline{a}}_{ee}(\mathbf{H}_0) = \overline{\overline{a}}^T_{ee}(-\mathbf{H}_0), \qquad \overline{\overline{a}}_{mm}(\mathbf{H}_0) = \overline{\overline{a}}^T_{mm}(-\mathbf{H}_0), \qquad \overline{\overline{a}}_{me}(\mathbf{H}_0) = -\overline{\overline{a}}^T_{em}(-\mathbf{H}_0) \tag{2}$$

Here $\mathbf{H}_0$ denotes a medium parameter (or a set of several parameters) which is odd under the time reversal operation.

On the macroscopic level, we deal with the averaged quantities – *constitutive parameters* – which connect the four field quantities as in

$$\mathbf{D} = \overline{\overline{\epsilon}} \cdot \mathbf{E} + \overline{\overline{\xi}} \cdot \mathbf{H}, \qquad \mathbf{B} = \overline{\overline{\mu}} \cdot \mathbf{H} + \overline{\overline{\zeta}} \cdot \mathbf{E} \tag{3}$$

The Onsager-Casimir principle for the macroscopic parameters can be written as

$$\overline{\overline{e}}(\mathbf{H}_0) = \overline{\overline{e}}^T(-\mathbf{H}_0), \qquad \overline{\overline{h}}(\mathbf{H}_0) = \overline{\overline{h}}^T(-\mathbf{H}_0), \qquad \overline{\overline{g}}(\mathbf{H}_0) = -\overline{\overline{f}}^T(-\mathbf{H}_0) \tag{4}$$

On the microscopic level of consideration we have the fields $\mathbf{E}$ and $\mathbf{B}$ which act on charged particles and cause their displacements. On this level, the fundamental principles such as causality or the Onsager–Casimir principle should be applied to the parameters which connect microscopic responses (such as molecular dipole moments) with the microscopic fields $\mathbf{E}$ and $\mathbf{B}$. Thus, the Fourier transform of the molecular polarizability is subject to the Kramers–Kronig relations, etc. To describe a macroscopic object we average the fields and introduce the notions of so called induction fields $\mathbf{D}$ and $\mathbf{H}$. Instead of the molecular polarizabilities we deal with constitutive parameters which are in a certain sense averaged values of their microscopic counterparts. Naturally, we expect that the same principles of causality and symmetry should also apply to the macroscopic parameters. If not, we would actually conclude that the way of introducing the macroscopic parameters is non-physical.

It is important for the macroscopic electromagnetics since at the macroscopic level we cannot any more distinguish between primary and induction fields as the source and reaction fields. In different situations one or the other field can be fixed by the sources and we have to treat that as the primary source field. Causality requirement leads to the conclusion that both the permittivity $\epsilon$ and its inverse $\epsilon^{-1}$ satisfy the Kramers–Kronig relations. Similarly, both these quantities are even with respect to the time reversal, according to the Onsager–Casimir principle. In the more general case we see that these principles can be universally applied to any of the sets of the bi-anisotropic parameters.

Finally, we have found that the microscopic and macroscopic Onsager–Casimir principles (symmetries with respect to the time inversion) are related, since the macroscopic parameters are introduced as a result of a certain averaging procedure. In this procedure, correct mathematical relations between variables of different mathematical nature should be always maintained.

# STUDYING PHOTONIC BANDGAP WAVEGUIDES USING FDTD

T. Uusitupa[1] and K. Kärkkäinen[2]
Electromagnetics Laboratory / Helsinki University of Technology
P.O. Box 3000 FIN-02015-HUT, Finland
email: tero@eml.hut.fi

ABSTRACT. FDTD modelling of dielectric PBG waveguides is considered. Waveguides are assumed to be layered structures, where one layer is a PBG plate. Many essential features can be modelled 2-dimensionally.

## PBG MODELLING AND SOME NUMERICAL EXAMPLES

Photonic bandgap (PBG) material is periodically inhomogeneous material, in which EM waves having frequency in the bandgap range, can't propagate. One example of a real-world PBG is a silicon plate having a uniform lattice of cylindrical air holes. PBG material can be used as a frequency selective reflective surface, or as a wall in a sharp waveguide bend etc. Here, the chosen PBG lattice is triangular (figure 1). The modelling scheme can be considered as a "virtual measurement setup". There is a source i.e. a field excitation, for which time and spatial dependence is properly chosen. The space-time behaviour of EM fields is solved using FDTD. There are measurement surfaces, on which time-dependent fields are sampled and stored to hard disk for later analysis: field F-transforms, power flow analysis etc. Figure 1 shows measurement setup involving straight PBG waveguide.

The numerical examples are done in 2-D and assuming $TE_z$ polarisation. In all examples pulse-like excitation is used. First example is a power flow analysis of a straight PBG waveguide. Figure 2 (left) shows $P(f)$ at one measurement plane, with a few waveguide width $w$ values. PBG lattice i.e. frequency bandgap is same in every case. When $f$ belongs to bandgap, PBG works as a boundary as far as energy flow is conserned. Thus, a mode can't propagate power in the waveguide, if $f < f_{cut-off}$. Cut-off frequency goes up as the waveguide is made narrower, which can be seen in figure 2. Second example deals with determining the wavelength $\lambda(f)$ of a propagating wave, in a PBG waveguide which can be approximated as a lossless periodic waveguide, when $f$ is in the bandgap (small radiation loss). F-transformed fields at two planes were computed. Using the field phase-difference between the planes (plane separation was $a$ i.e. the waveguide period), wavelength $\lambda(f)$ was obtained (figure 2, right). In examples 1 and 2 a PEC-boundary at the waveguide centerline was used to permit only the symmetric modes. $f$ being in the bandgap and small enough, field roughly corresponds to fundamental mode. Third example is a transmission analysis of a $60^o$ waveguide bend. $P(f)$ was computed at two planes. The $H_z$-field snapshot and transmission $T(f)$ are shown in figure 3. In considered structures, the field is mostly consentrated in one layer (PBG plate). Simulation in 3-D, instead of 2-D, often means just higher radiation loss and a bit frequency-shifted response, due to a bit different effective refraction index seen by the wave.

REFERENCES: Joannopoulos, J.D. *et al.*, 1995: Photonic Crystals, Molding the Flow of Light. Princeton University Press.

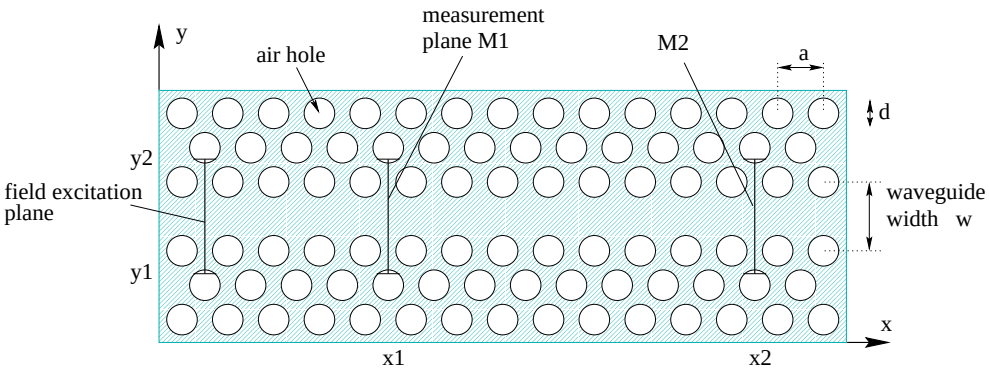


Figure 1: Triangular lattice PBG. Straight waveguide measurement setup.

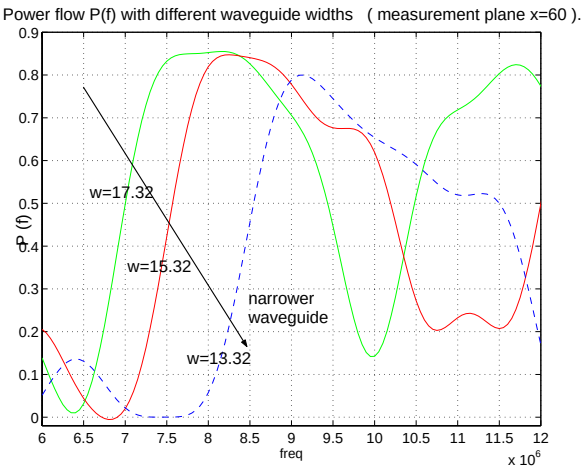


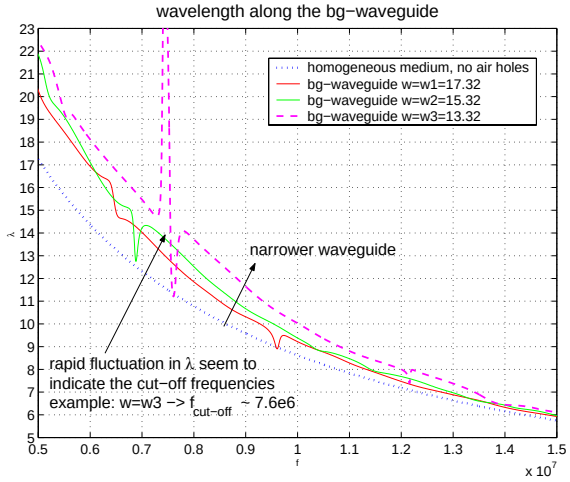


Figure 2: Left: power flow at $x = 60$. Right: wavelength in the PBG waveguide.

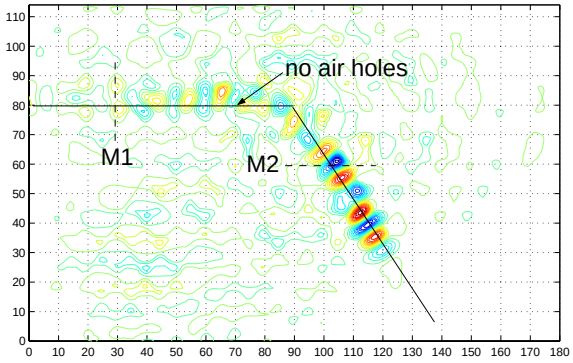


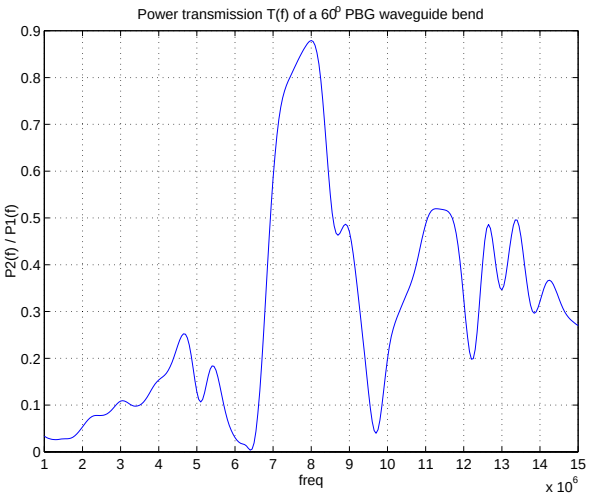


Figure 3: Left: $H_z$-field snapshot in $60^o$ bend. Right: power transmission of a $60^o$ bend.

# IDEAL BOUNDARY CONDITIONS IN ELECTROMAGNETICS

I.V. Lindell,
Electromagnetics Lab., Helsinki University of Technology
PO Box 3000, FIN-02015HUT, Espoo, Finland

The concept of 'boundary' in electromagnetic theory relates to a surface which does not let electromagnetic fields pass through it. Mathematically, the fields are related by boundary conditions at the surface. In contrast, the interface of two media is defined by conditions of continuity or discontinuity of the fields at the surface. Boundary is normally an approximation to the interface giving mathematical convenience and can be applied under certain restrictions.

Assuming time-harmonic fields with time dependence $e^{j\omega t}$, the concept of 'ideal boundary' is defined so that the complex Poynting vector $\mathbf{S} = \frac{1}{2}\mathbf{E} \times \mathbf{H}^*$ has no component normal to the surface of the boundary for any possible fields. This definition is tighter than that of the 'lossless boundary', in which case the real part of the Poynting vector has no component normal to the boundary. The two basic ideal boundary conditions most often encountered in electromagnetics are the perfect electric and magnetic conductor (PEC and PMC) conditions defined by $\mathbf{n} \times \mathbf{E} = 0$ (PEC) and $\mathbf{n} \times \mathbf{H} = 0$ (PMC). Obviously, in both of these cases we have $\mathbf{n} \cdot \mathbf{E} \times \mathbf{H}^* = 0$, whence the complex Poynting vector has no normal component. Yet another type of ideal boundary is the so-called soft-and-hard (SHS) boundary [1] defined by the conditions $\mathbf{v} \cdot \mathbf{E} = 0,\ \mathbf{v} \cdot \mathbf{H} = 0$, where $\mathbf{v}$ is a real unit vector tangential to the surface $S$, i.e., satisfying $\mathbf{n} \cdot \mathbf{v} = 0$.

It is of interest to see whether there are more general ideal boundary conditions. In fact, it can be shown that there exists a generalization to the ideal SHS conditions as $\mathbf{a} \cdot \mathbf{E} = 0,\ \mathbf{a}^* \cdot \mathbf{H} = 0$, where $\mathbf{a}$ is a complex vector satisfying $\mathbf{n} \cdot \mathbf{a} = 0$. Such a surface will be called the generalized soft-and-hard surface (GSHS) [2]. Basic properties for a plane wave reflecting from a GSHS plane are derived. It is shown that TE and TM components (with respect to the complex vector $\mathbf{a}$ and its complex conjugate $\mathbf{a}^*$, respectively), of a plane wave are reflected from a GSHS plane as from respective PMC or PEC planes. Image theory for the GSHS plane is suggested with an example.

The GSHS boundary is an anisotropic ideal boundary. It is interesting to know that there is also an isotropic ideal boundary which is the generalization of the perfectly conducting (electrically or magnetically) surface [3]. Such a boundary is, however, not linear since the boundary conditions turn out to be of the form $\mathbf{E}_t = Z\mathbf{H}_t^*$ where $t$ means component tangential to the surface. The condition involving the complex conjugation could actually be called semilinear since it satisfies only one of the two conditions of linearity. The most striking result is a special planar isotropic ideal surface which acts as a retroreflector: it reflects the incident plane wave back to the direction where it comes from. In general the reflecting wave will split in two

parts: one reflecting in the specular direction and the other one in the backward direction. Image theory for the general planar isotropic ideal surface can be formed for a source in complex space producing a Gaussian beam.

REFERENCES

[1] P.S. Kildal, 1990: Artificially soft and hard surfaces in electromagnetics, *IEEE Trans. Ant. Prop.*, vol.38, no.10, pp.1537-1544.
[2] I.V. Lindell: The ideal boundary and generalized soft-and-hard surface, *Proc. IEE Micro. Ant. Propag.*, in press.
[3] I.V. Lindell, 2000: Condition for the general ideal boundary, *Micro. Opt. Tech. Lett.*, vol.26, no.1, pp.61-64.

# Wireless Communication – Part I

# IMPROVEMENTS OF WELDED RF COMPONENTS THROUGH COMPUTER SIMULATIONS

Pekka Eskelinen[1] and Harri Eskelinen[2]
[1]Finnish Defence Forces´ Technical Research Institute
PL 10, 11311 Riihimaki, FINLAND
[2]Lappeenranta University of Technology
PL 20, 53851 Lappeenranta, FINLAND
email: ari.eskelinen@pp.inet.fi

ABSTRACT. Electromagnetic simulation packages which include a reliable surface current model can be used to pinpoint the critical areas of welded RF constructions e.g. in wide-band patch antenna arrays for 1–3 GHz operation. A rough 6–10 step discretization of current density is enough. Our results indicate a possibility to achieve performance comparable to those of laser welded samples by cheap arc processes.

## INTRODUCTION

The fast growing telecommunications manufacturing not only relies on state-of-the-art electronics but also makes use of very sophisticated mechanical structures, the design of which must be based both on a solid understanding of e.g. milling or sheet metal work and on the often tricky RF dimensioning as shown e.g. in *Eskelinen H*. (1999). The up to now applied practices have separated these two which has caused a notable amount of unnecessary iteration cycles and performance figures far from optimum, see *Hoek et al*. (1999). As an attempt to find out more efficient ways in combining the requirements of mechanical and microwave engineering we have conducted a survey of possibilities to enhance the quality of patch antennas. A key feature in them is the short circuiting welded joint at one end which not only supports the quarter wave radiating element above the ground plane but also partially contributes to matching which was also shown in *Eskelinen P et al*. (1999).

## THE WELDING PROBLEM

The real problem with the patch array is how to make a number of cheap welds so as to produce a series of optimum RF connections without physical ground plane distortions.

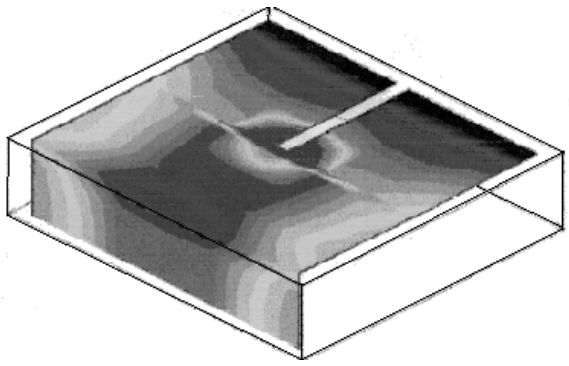

Fig. 1. A simulation shows how the microwave current density concentrates at the two lower corners of a patch element - just where welding is most difficult.

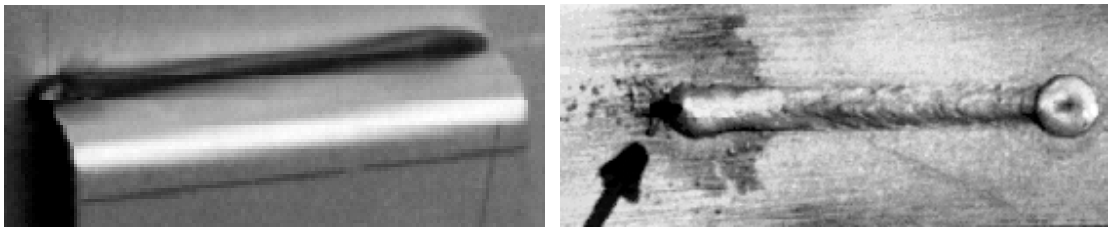

Fig. 2. The weld is hardly visible from the upper side (left). Problems were avoided specially at the starting point of each individual weld, marked with an arrow in the righthand photograph taken from the back of the ground plane.

Considerable relief to this task can be found from some of the latest electromagnetic simulation software packages, demonstrated e.g in *Eskelinen P*. (2000), with which the user can not only perform the conventional electronic tasks but also go one step towards the real physical or mechanical device by having the computation show also the microwave current density along the surfaces of the sample to be designed. This is demonstrated for our patch antenna example in Fig. 1. The interpretation as regards welding of the L-shaped piece should be quite obvious. If the connection at the two lower corners of the element - places through which most of the RF current flows - are not perfect there is not much sense in trying anything else either.

## SAMPLE RESULTS

The simulation results provided by electrical engineering science were adopted to the welding process with ashtonishingly good results. Figure 2 shows one of the real welded aluminium alloy samples which do have a well-defined contact at their edges due to a carefull and tedious tuning of the welding parameters. Because the welding power could be reduced in the middle of the element the heat input was also lower and thus the vertical distortions of the ground plane could be kept reasonable.

Based on present experiences it seems very likely that a number of mechanical microwave components, mostly needed in the cellular phone business, can benefit from the suggested approach. Those novel software packages which allow the user also to create a realistic, dimensioned physical model of the electronic device and see the energy flow on its surfaces make it much easier to find out where the focus should be when designing the mechanical construction and its manufacturing methods and sequences.

## REFERENCES

Eskelinen H.,1999: Observations on the manufacturability of mechanical subassemblies for maritime and missile electronics , *Proc. 5th International Radar Conference*, Brest

Eskelinen P., Eskelinen H. and Tiihonen K., 1999: A prototype of an adaptive integrated antenna system for cellular networks, *Proc. European Wireless ´99*, Munich, 87–90

Eskelinen P., 2000: Software review : IE3D Electromagnetic Simulation Package, *IEEE Aerospace and Electronic Systems Magazine*, vol 15/00, 22–23

Hoek C., Kuchar A. and Tafener M., 1999: Uplink and downlink field trial with a GSM/DCS1800 smart antenna base station. *Proc. European Wireles´99*, 113–118

# PERFORMANCE LIMITATIONS OF TACTICAL MOBILE VHF ANTENNAS

Pekka Eskelinen
Finnish Defence Forces´ Technical Research Institute
PL 10, 11311 Riihimaki,FINLAND
phone: 358-19-1812111, email: ari.eskelinen@pp.inet.fi

ABSTRACT. Present military communication vehicles utilize VHF antenna elements and mounting schemes which cause the radiation pattern maxima to point up to 30 degrees above the horizon and create sharp minima in the azimuth pattern, generally below 20 dB, which together can harm communications and give possibilities for hostile ECM. Besides this, commercial wide-band antennas are lossy designs with efficiencies between 5-10 per cent. Link towers on the vehicles further impair the VHF performance. The most notable drawback from ECM point-of-view is the lack of adaptive beamforming.

## INTRODUCTION

Tactical military radio communications benefit from the use of the lower VHF frequency band between 20–80 MHz due to its fairly favourable propagation characteristics with respect to the mission scenario. Mobile systems with multiple ground-plane antennas mounted on a single armoured vehicle have been introduced both by the western defence forces as well as the former Soviet troops for e.g. $C^3M$ purposes. Even a reasonably sized military force can have hundreds of communication vehicles which limits a thorough redesign of the radio concept but calls for low-cost add-on improvements.

## SUMMARY OF CURRENT RESULTS

A scale model study of possibilities for performance enhancement obtainable with current installations, based on non-classified information about vehicle geometry and antenna designs, has shown that a typical construction having 2–5 whip elements suffers from a poor radiation efficiency occasionally below –20 dBi and produces arbitrary azimuth patterns due to the mutual interaction. The obvious rising trend of the elevation pattern with main lobe maxima between 10–40 degrees above the local horizon reduces the available gain in the direction of communication by more than 10 dB. Figure 1 illustrates a very typical measured pattern geometry for azimuth and elevation planes.

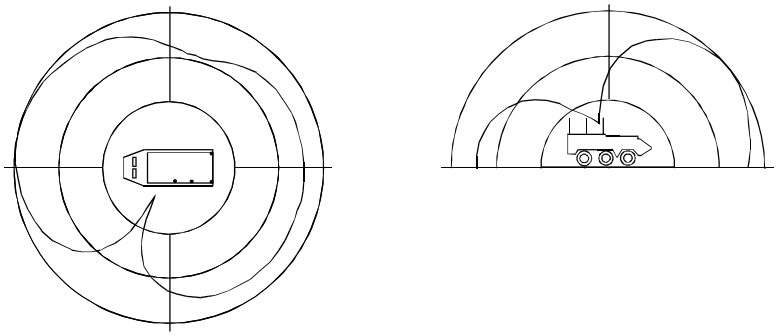

Fig. 1. Multiple vehichle-mounted VHF antennas have 20 dB azimuth pattern minima and main beam maxima 10–40 $^0$ above horizon. Scale 10 dB/div.

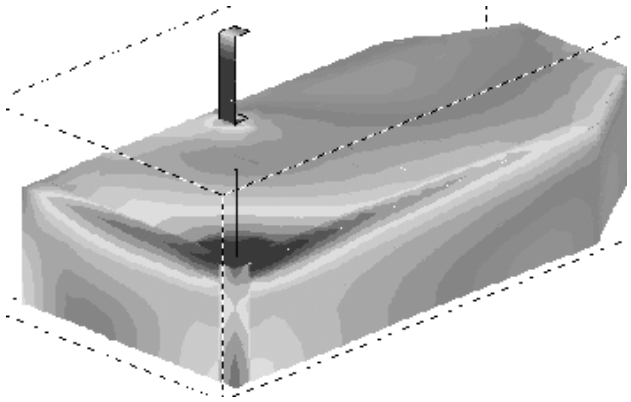

Fig. 2. A case example of simulated surface currents. The radiating element is located in the lower right corner of the vehichle and a passive one (terminated) up in the middle.

It seems that the applied design and mounting rules have been based on sole mechanical requirements and have given additional possibilities both for intentional hostile jamming or airborne reconnaisance attempts. Extensive scale model measurements with a technology developed originally in *Eskelinen* (1999) have been carried out to verify the chances of pattern or efficiency improvement obtainable with modifications which were found by software simulations similar to *Foster* (1999) performed for two typical vehicle constructions and set-ups.

Both the armoured platform itself and some surrounding terrain have been used in the model. The tests performed up to now indicate that there is a lower limit of vehicle dimensions (around $\lambda/4$ at the lowest operating frequency) below which neither an unambigious adjustment of azimuth patterns nor an increase of the radiation efficiency in wide-band operation is possible without a comprehensive change in the operating concept and equipment as is shown in *Eskelinen* (1997). Also the mutual coupling of near-by radiating elements will stay very high. The simulated RF surface currents, as shown in Fig. 2 turned out to be a very effective analysis tool for this.

In most cases the pattern maximum can be forced to go down to or even below the local horizon and the radiation to high angles will be attenuated by 10–20 dB without totally sacrificing the wide-band nature of the original antenna. Initial trials with a scale mock-up of a typical western armoured vehicle have demonstrated the potential capability to bring a C/I improvement exceeding 30 dB in the best case and 6–8 dB in less favourable conditions just with some passive beamformers.

REFERENCES

Eskelinen P., 1997: Effects of Test Vehicle Patterns on Cellular Coverage Measurements, *IEEE Aerospace and Electronic Systems Magazine* vol 12/97, 12–15

Eskelinen P., 1999: Mobile Military Communications Beyond 2000, *IEEE Aerospace and Electronic Systems Magazine*, vol 6/99, 31–33

Foster P., 1999: Siting Considerations and Performance Implications for Radar Antennas on Helicopters, *Proc. 5th International Conference on Radar Systems*, Brest, 451–454

# A SHORT PERFORMANCE EVALUATION OF THE METSÄHOVI CLOCK ARRANGEMENT FOR VLBI MEASUREMENTS

Pekka Eskelinen[1] and Pekka Sjöman[2]
[1]Finnish Defence Forces´ Technical Research Institute
PL 10, 11311 Riihimaki, FINLAND
[2]Helsinki University of Technology, Metsähovi Radio Observatory
Metsähovintie 114, 02540 Kylmälä, FINLAND
[1]email: ari.eskelinen@pp.inet.fi

ABSTRACT. A frequency drift of 7E-15/d, indicating an anomaly in the device, and both periodic and random timing fluctuations exceeding 25 ns have been observed in the Metsähovi hydrogen maser clock system through long-term comparisons with a high performance caesium clock and three different GPS receivers. The most notable time constants are 24 and 140 hours. Only a weak if any correlation has been found with the monitored clock temperature, barometric pressure or supply voltage. The contribution of the distribution and comparison electronics to the fluctuations remains to be verified.

## INTRODUCTION

Due to the importance of timing accuracy for the radio astronomical measurements at Metsähovi, attempts have been made in the past to define the uncertainty of the installed hydrogen maser clock, see e.g. *Eskelinen P.* (1996). When a modern caesium clock came free from its pervious tasks described in *Eskelinen P.* (1999) and as the Metsähovi maser was recently tuned, a new test was considered relevant. The arrangement included a comparison system between the three GPS receivers and the H-maser and a temporary set-up for Cs - H-maser. The maser 1 pps signal was provided from a distribution amplifier/isolator. As a background *Eskelinen P.* (2000) and *Parker T.* (2000) were used.

## KEY RESULTS

As shown in Fig. 1 (left), the H-maser has a relative frequency drift of around 6.7E-15 per day which exceeds at least by one decade the typical reported value for similar units. When the timing bias and the drift are removed we notice a 30 ns peak value fluctuation composed of several periodic and non-periodic terms (right). From 500 hours on

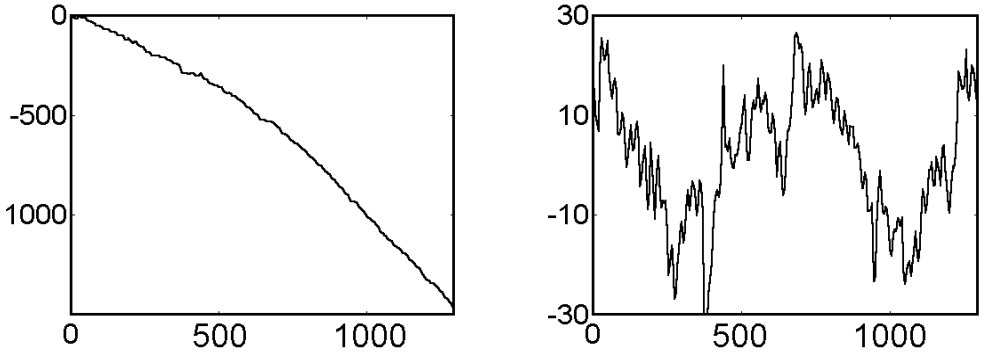


Fig. 1.The difference between the caesium clock and the H-maser shows a relative frequency drift of 6.7E-15/d and 30 ns fluctuations. Vertical scale in ns, x-axis in hours.

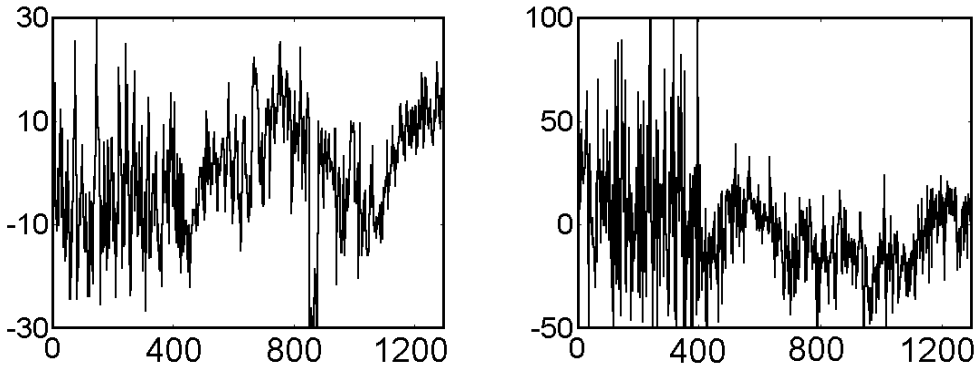


Fig. 2.The GPS measurement confirms the H-maser time shift starting at 500 hours and shows the noise in GPS1 output (right). S/A was turned off by the US at 400 hours.

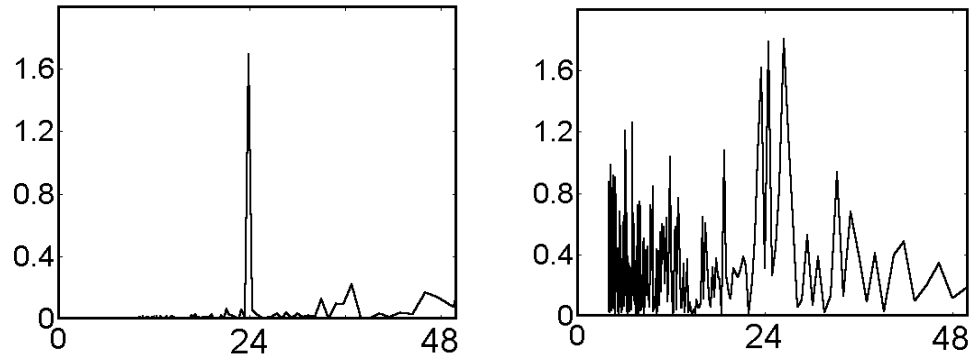


Fig. 3. Both the difference to caesium (left) and to GPS show a clear 24 hour cycle but only GPS2 seems to be a feasible reference. Others, like GPS3 (right), suffer from spurious signals in their output. Vertical scale: rel. probability, x-axis in hours.

the GPS and Cs agree, see Fig. 2, indicating a timing (very likely not frequency) error in the H-maser output. The clearest periodic term has a time constant of 24 hours as shown in Fig. 3. GPS comparisons are less suitable for this judgement due to the excessive noise content. The time functions of local temperature or presssure, opposed to *Dragonette R.* (1991), do not clarify the clock behaviour except for a transient at 400 hours, which has caused a deviation in the Cs comparison.

REFERENCES

Dragonette R.,1991: Barometric pressure-induced frequency offsets in hydrogen masers, *Proc. 45th Annual Symposium on Frequency Control*, New York, 586-590

Eskelinen P., 1996: GPS-based comparison of H-maser and caesium timescales, *Proc. URSI/IEEE XXI Convention on Radio Science*, Espoo, 106-107

Eskelinen P., 1999: Experiments with a caesium-locked UHF time&frequency reference transmitter, *Proc. URSI/IEEE XXIV Convention on Radio Science*, Turku, 22-23

Eskelinen P., 2000: Observations on Stability Measurements of Atomic Clocks, *Proc. 1999 Joint Meeting of The European Frequency and Time Forum*, Besancon, 186-189

Parker T., 2000: Hydrogen Maser Ensemble Performance and Characterization of Frequency Standards, *Proc. 1999 Joint Meeting of The European Frequency and Time Forum*, Besancon, 173-177

# CURRENT STATUS OF THE SUBMILLIMETRE WAVE HOLOGRAM COMPACT ANTENNA TEST RANGE

Janne Häkli, Jussi Säily, Juha Ala-Laurinaho, Jussi Tuovinen, Antti V. Räisänen
Radio Laboratory, Helsinki University of Technology
P.O.B. 3000, FIN-02015 HUT, Finland
Email: janne.hakli@hut.fi

## ABSTRACT

Millimetre (30–300 GHz) and submillimetre (300–3000 GHz) waves are increasingly used in applications including telecommunications, radar, remote sensing, and space research. Future scientific satellite missions have on-board instruments and antennas that operate at these frequencies. Testing of these satellites at very high frequencies is demanding, and various methods have been proposed for the task. The compact antenna test range (CATR) principle is believed to have the greatest potential for the task. In this paper, the current status of the hologram-based CATR is presented.

## THE HOLOGRAM CATR

In the hologram CATR, a radio frequency computer-generated hologram is used to create a planar wavefront. The hologram pattern is etched on a thin metallized polyester film and stretched on a frame. The volume where the peak-to-peak amplitude and phase variations of the plane wave are less than 1.0 dB and 10 degrees is called the quiet-zone of the CATR. The antenna-under-test (AUT) must be placed inside this volume. Figure 1 shows the layout of the hologram CATR and a typical hologram pattern.

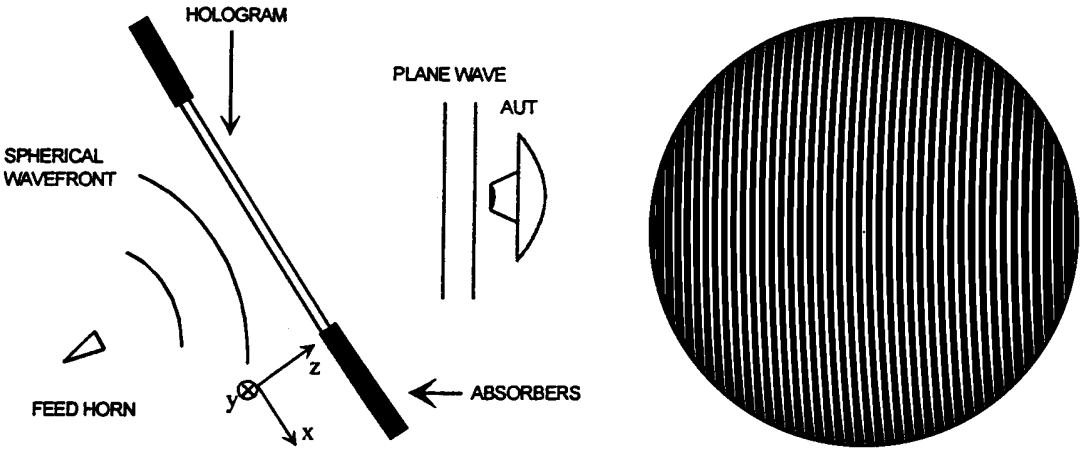


Figure 1. Layout of the hologram CATR and a typical hologram pattern.

The hologram CATR has been used for testing a 39 GHz low-profile link antenna and the Swedish Odin satellite at 119 GHz. The suitability of the hologram CATR for submillimetre wave operation was verified with a small-sized demonstrator CATR operating at 310 GHz [1]. The hologram diameter was 60 cm, and the quiet-zone field was measured 1.5 meters from the hologram surface. The test results showed good correlation between the theoretical and measured fields. Figure 2 shows the measured contour map of the quiet-zone amplitude.

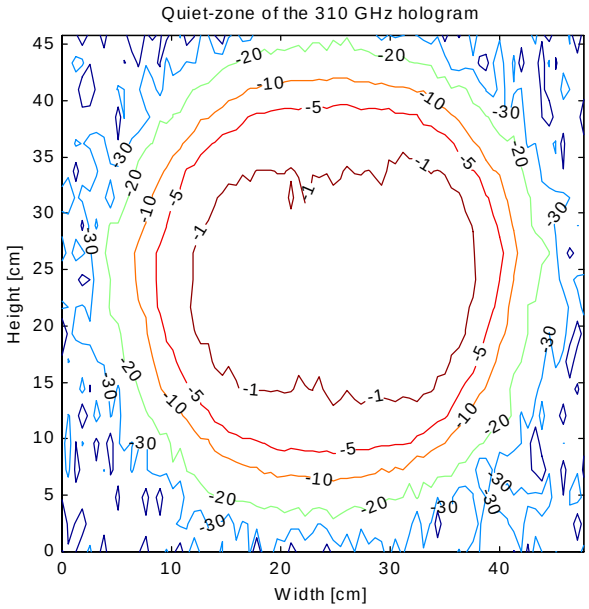


Figure 2. Quiet-zone amplitude contour map.

## CURRENT STATUS

The first two-year project for ESA ESTEC, 'Submillimetre wave antenna testing using a hologram CATR', has been successfully concluded. The results of this project promising and continued funding is available and a new project has been started. Goals of the new project include development of the hologram manufacturing, building a large CATR for 322 GHz, testing of a 1.5 meter satellite dish at 322 GHz, 650 GHz test instrumentation, and building a small test CATR for 650 GHz. An improved hologram feed system consisting of two shaped reflectors will also be developed.

Manufacturing of large holograms was found to be the most difficult obstacle in the development of an usable submillimetre wave hologram CATR. In the future a lot of development work will be related to manufacturing. Studied methods include advanced joining of hologram pieces and photomasks, and selective metallization of a substrate. Instrumentation for the 650 GHz test range is being studied. The AB Millimétre vector network analyzer MVNA-8-350 will be used in conjunction with a phase-locked backward-wave oscillator (BWO) and a sensitive Schottky receiver. Reflector synthesis software for the dual reflector feed is also being studied.

## ACKNOWLEDGEMENTS

This project has received funding from ESA ESTEC (Contract No. 13096/98/NL/SB), the Academy of Finland, and TEKES. The authors would also like to thank mr. Eino Kahra and Lauri Laakso from the Radio Laboratory workshop for their valuable help.

## REFERENCES

[1] Säily, J., Ala-Laurinaho, J., Häkli, J., Tuovinen, J., Lehto, A., Räisänen, A.V., "Test results of a 310 GHz hologram compact antenna test range", *Electronics Letters*, Vol. 36, No. 2, 2000, pp. 111-112.

# DEVELOPMENT OF A PHASE-LOCKING SYSTEM FOR SUBMILLIMETRE WAVE BACKWARD-WAVE OSCILLATORS

Jussi Säily, Juha Mallat, Antti V. Räisänen
Radio Laboratory, Helsinki University of Technology
P.O.B. 3000, FIN-02015 HUT, Finland
Email: jussi.saily@hut.fi

## ABSTRACT

Accurate antenna testing at submillimetre wavelengths (>300 GHz) using the compact antenna test range (CATR) principle requires stable and powerful source oscillators. Especially, high transmitted power is needed in testing the CATR quiet-zone field quality. Frequency-multiplied Gunn oscillators are useful up to a several hundred GHz, but the low multiplication efficiency severely limits the output power. Phase-locked backward-wave oscillators (BWO) are powerful, do not need frequency multiplication, and can easily be associated with vector network analyzers. They are very suitable for antenna testing and even for low-noise local oscillators in receivers. In this presentation, the design and test results of a phase-locked BWO at 310 GHz are discussed.

## DESIGN AND CONSTRUCTION OF THE PLL SYSTEM

The very common second-order phase-locked loop topology using an active loop filter was chosen for the system [1,2]. The downconversion of the BWO frequency for phase detection is done using a harmonic mixer. The PLL control signal is applied to the BWO anode, i.e. the tube ground, over a 100 Ω resistor to ground. The schematic of the constructed PLL system is shown in Figure 1.

Initial design of the loop filter and choosing the component values were done according to [1]. The loop filter and the whole PLL were then modeled into APLAC circuit simulator. Loop filter component values were optimised with the simulator in order to maximize the PLL control bandwidth. In the active loop filter design, all the pole-setting resistors are adjustable trimmers, and optimisation of the actual phase-locked oscillator performance is possible. The loop gain can also be adjusted. Thus, the same "lock-box" can be used with different types of BWOs by just optimising the loop filter with the trimmer potentiometers.

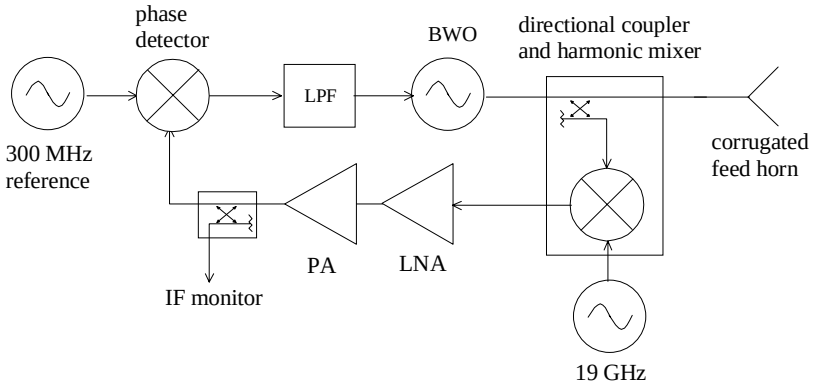


Figure 1. Schematic of the BWO-PLL system.

TEST RESULTS OF THE PLL SYSTEM AT 310 GHz

The constructed PLL was tested with a BWO at 310 GHz. After optimisation of the spectral quality with the loop filter trimmers, various oscillator parameters were measured and compared to the free-running case, i.e., without phase-lock control. The free-running BWO signal spectrum is about 300 kHz wide. The BWO tube heating current polarity is changed once in 10 seconds, and this creates a frequency jump of about 4 MHz. Long-term stability of the free-running BWO was also measured. Drifting of the center frequency is less than 5 MHz/hour. The drifting is slow enough not to disturb the PLL operation for at least in a couple of hours, and it is also easy to compensate with the computer controlled power supply.

Phase-locked spectra measured from the 'IF monitor' -port are shown in Figure 2. The measured power level is so low, that the noise floor of the spectrum analyzer itself affects the measurement. The phase-locking is stable and no adjustments are necessary for at least a couple of hours. A computer program to control the frequency and phase-locking of the BWO is being designed in LabView.

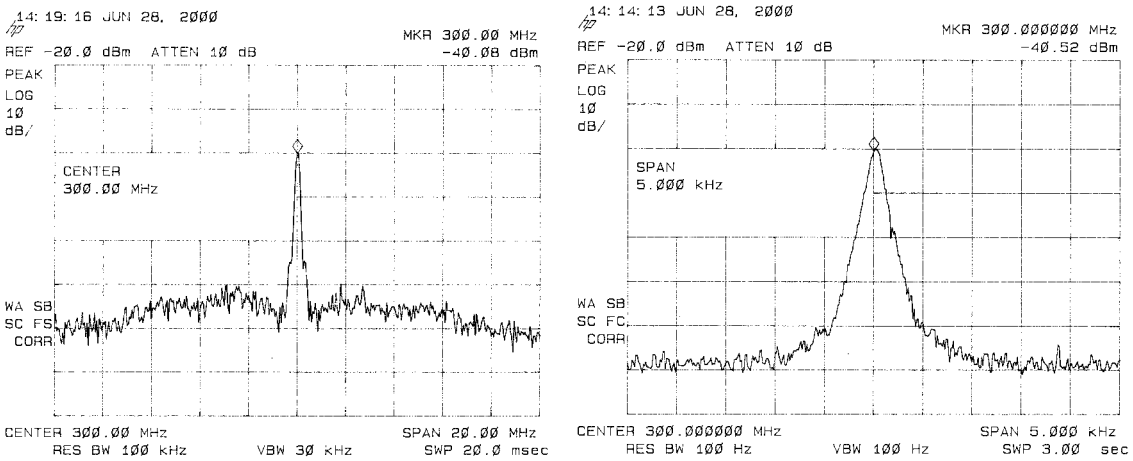


Figure 2. Measured spectra of the phase-locked backward-wave oscillator.

ACKNOWLEDGEMENTS

This project has received funding from the Academy of Finland, TEKES, and ESA ESTEC. The authors would also like to thank Dr. Philippe Goy (AB Millimétre, Paris, France) for valuable advice. Mr. Eino Kahra and Mr. Lauri Laakso from the Radio Laboratory workshop are also thanked for their help in mechanical constructions.

REFERENCES

[1] Gardner, F.M., "*Phaselock Techniques*", 2nd Edition, New York, 1979, John Wiley & Sons, Inc., 285 p.

[2] Rohde, U.L., "*Microwave and Wireless Synthesizers : Theory and Design*", New York, N.Y., 1997, John Wiley & Sons, Inc., 638 p.

# LNA and mixer circuits for a 60 GHz Radio Front End

Mikko Karkkainen[1], Jan Riska[1], Pekka Kangaslahti[1,2], Veikko Porra[1]

[1]Helsinki University of Technology, Inst. of Digital Communication,
Electronic Circuit Design Laboratory
[2]Ylinen Electronics

P.O.Box 3000, FIN-02015 HUT
mikko.karkkainen@ecdl.hut.fi

***Abstract –*** *This paper presents a prototype monolithic low noise amplifier (LNA) and a balanced resistive mixer realized using pseudomorphic high electron mobility transistors (PHEMT), which are manufactured with a 0.15 μm-gate-length GaAs process. LNA gain of 18 dB and noise figure of 5.0 dB was obtained using three 2x35 μm PHEMTs. The mixer has 13 dB conversion loss for 4.5 dBm local oscillator power.*

*A revised version of the mixer is expected to have only 10 dB conversion loss. The receiver would then have a total gain of 8 dB and a noise figure of 6.3 dB at 60 GHz. The intermediate frequency at the receiver output is 5.3 GHz.*

## I INTRODUCTION

Development of multimedia services and demand for mobile terminals has lead to increasing wireless data traffic. High data rates need larger bandwidths and thus higher frequencies. This scenario makes the research on the 60 GHz radio front end interesting.

In this study some basic RF-blocks are designed for a 60 GHz transceiver front end. Only the low noise amplifier (LNA) and the balanced resistive mixer are discussed here. After packaging the chips can be combined to form a complete 60 GHz radio front end. The results will be used as a reference for further development. The individual blocks are first realized as separate chips and then the integration level is enhanced by inserting a LNA and an image rejection mixer circuits on one chip.

## II SIMULATED AND MEASURED RESULTS

On-wafer measurements of the LNA were carried out using V-band RF-probes. The HEMTs are biased at 2.5 V drain voltage and 14 mA drain current. The vector network analyzer results show 18 dB of gain and load matching is better than –10 dB. Due to changes in the processing and coupling effects between ground-VIAs and microstrip lines the input match was worse than expected. The measured noise figure and gain of the LNA is presented in figure 1. The input return loss is -4 dB at 60 GHz. The measured LNA noise figure is 5.0 dB at 60 GHz.

The single balanced resistive mixer was also measured. The conversion loss was 13 dB for oscillator power of 4.5 dBm. The loss is expected to decrease to about 10 dB for the optimum 10

dBm LO power. The measurements were performed in an upconversion configuration. The revised version of the mixer was designed and the simulated gain compression is presented in figure 2. The packaging of the chips is underway. For a mixer loss of 10 dB we can expect to obtain a receiver gain of 8 dB and a noise figure of 6.3 dB. The chips are bonded on microstrip, which has transition to WR-15 waveguide. The IF output is coaxial.

## ACKNOWLEDGEMENTS

This study is based on a contract between HUT/ECDL and Technical Research Center of Finland (VTT/Ele). The contract is a part of LALAMO, a project on wireless wideband modems supported by the Finnish Technology Development Center (TEKES), Nokia Networks, Nokia Research Center and Ylinen Electronics.

## REFERENCES

[1] J. Riska, P. Kangaslahti, M. Karkkainen, and V. Porra, "60 GHz PHEMT MMICs for Broad-Band Wireless Front End", Proc. 10th Conference on Microwave Technique, Prag, 1999.

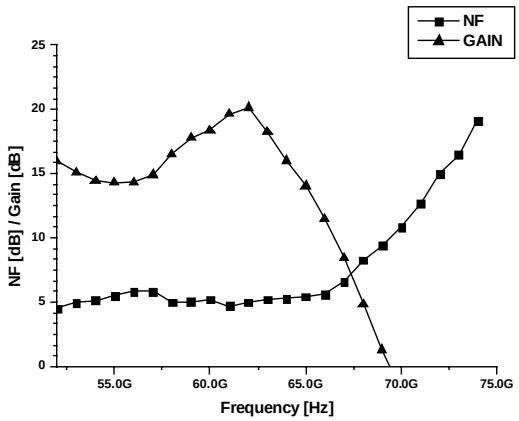


Figure 1. Measured LNA gain and noise figure

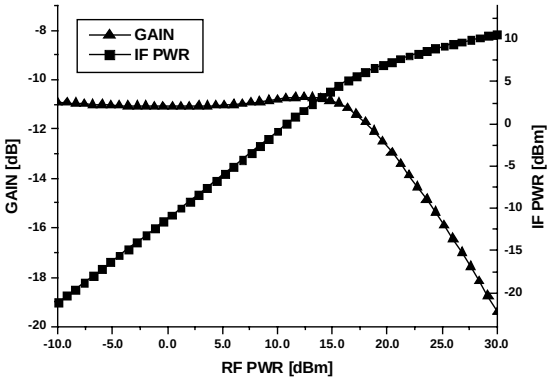


Figure 2. Simulated mixer compression

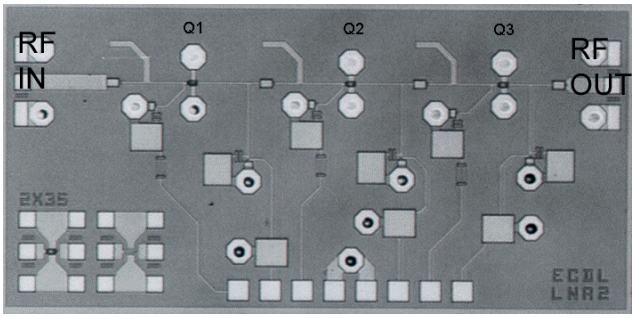


Figure 3. Microphotograph of the LNA. Chipsize is 3.0 x 1.5 mm$^2$.

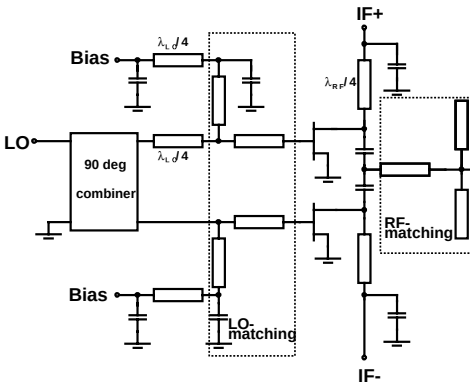


Figure 4. Balanced mixer circuit

# Space Weather

# New European Satellite Navigation Service Galileo

Seppo Korpela and Fredrick von Schoultz
Space Systems Finland Ltd.
Kappelitie 6
FIN-02200 Espoo, Finland
seppo.korpela@ssf.fi and fvs@ssf.fi

ABSTRACT. Galileo is a new navigation satellite programme initiated by European Union in collaboration with ESA. It will be the only global navigation system under civilian control. It will remarkably improve the availability and security of a satellite navigation system compared to present GPS and GLONASS systems which are under military control.

The present plan in to provide several classes of services for users. These are:

- OAS Open Access Service, free of charge, for applications intended for the public
- CAS Controlled Access Service, with restricted access, for commercial and professional applications
- SAS Safety-of-life Access Service
- GAS Governmental Access Service

The most important advantages of Galileo are integrity monitoring and guarantee of service. These will enable the use of the system in such more demanding applications as aviation.

The configuration of the Galileo system includes:

- satellite constellation providing navigation signal in space. It consists of 30 satellites in 3 orbital medium earth orbit (MEO) planes at an altitude of around 23 000 km and at an inclination of 54°.
- Ground segment controlling the satellites.
- A network of stations to monitor the signal from the satellites and to accurately calculate the orbits of the satellites.
- Elements to manage potential additional communication services, such as Search and Rescue.
- An integrity monitoring network to provide integrity information to fulfil higher performance requirements.
- Possible local components to have a very high integrity service around such areas as airports or harbours.

The frequency allocations for the international navigation systems have been increased in WRC2000 so that it is possible to use even three different frequencies to make ionospheric correction and to provide various types of services.

The definition phase will last until the end of 2000. The service is planned to be fully operational in 2008, although even tighter schedule will be considered in future.

# IONOSPHERIC EFFECTS IN GPS OBSERVATIONS

Markku Poutanen
Finnish Geodetic Institute
Geodeetinrinne 2
FIN-02430 Masala, Finland
Markku.Poutanen@fgi.fi

ABSTRACT. We give a short overview of the ionospheric effects in GPS (Global Positioning System) observations. In navigation, surveying and geodetic applications the range and range-rate errors caused by the ionosphere have to be removed, but GPS observations can be used in ionospheric studies as well. We also discuss use of data from permanently operating GPS stations for ionospheric studies.

## GPS AND IONOSPHERE

The GPS system consists (nominally) of 24 Earth-orbiting satellites (currently, 27) on six orbital planes with an inclination of 55° at the approximate height of 20 200 km. The orbital period is _ sidereal day, and at least six satellites are visible anywhere on the Earth. Each satellite transmits a signal on two frequencies, 1.5754 GHz (L1) and 1.2276 GHz (L2). On the L1 carrier is modulated the so-called C/A-code (*Coarse/Acquisition*, chip rate 1.02 MHz phase modulation) which is used in civilian applications, and on both frequencies the P-code (*Precise*, 10.23 MHz) which is reserved for military use. With the aid of the code, the signal transfer time and thus the range between the receiver and the satellite can be computed. Range observations simultaneously to at least four satellites are needed to solve for 3D position of the receiver. The current navigation accuracy is better than 10 m. (For an introduction to the GPS, see e.g. Poutanen, 1998.)

In surveying and geodetic applications the carriers L1 and L2 are used to measure the range to the satellite. Using relative observations between two receivers, an accuracy of a centimetre can be achieved. Continuously observing GPS stations, like the Finnish permanent GPS network FinnRef® (Ollikainen *et al.*, 1997) allow to track even smaller geophysical phenomena, like the postglacial rebound, the rate of which is a few mm/yr.

The range and range rate are biased by several different phenomena, ionosphere being one of the most important. Ionosphere affects the GPS signal as follows (Klobuchar, 1996): 1) Group delay of the C/A and P codes; 2) carrier phase advance; 3) Doppler shift (range rate error); 4) Faraday rotation of linearly polarised signal; 5) refraction (bending) of the microwave radiation; 6) distortion of pulse waveforms; 7) signal amplitude fading or amplitude scintillation; and 8) phase scintillation. Points 1) and 2) are the most important in GPS applications; in the first approximation they can be expressed as

$$\Delta^{ion} = \pm \frac{40.3}{f^2} \mathrm{TEC} \qquad (1)$$

where $f$ is the carrier frequency and TEC (*Total Electron Content*) the electron column density between receiver and satellite in units $10^{16}$ electrons / $m^2$. The total ionospheric bias varies between 1 .. 50 m. There is a daily and annual cycle and the Solar 11 yr activity cycle causes big variation in the ionosphere electron content. Polar regions (including e.g. Lapland) and mid-latitudes suffer mostly from the ionospheric activity.

PERMANENT GPS NETWORK AND IONOSPHERE

In relative GPS computation the effect of the ionosphere is removed using the so-called L3 combination, applying the relation in (1) that the effect is proportional to $1/f^2$,

$$\mathrm{L3} = \frac{f_{L1}^2}{f_{L1}^2 - f_{L2}^2}\mathrm{L1} - \frac{f_{L2}^2}{f_{L1}^2 - f_{L2}^2}\mathrm{L2}\,. \qquad (2)$$

This allows computation of vectors of any length without the ionospheric disturbance. Only if the ionosphere is changing rapidly, as often can happen near the Solar activity maximum, one may confront difficulties to get a reliable solution. Opposite to (2) one can use also L4 combination which removes all but the ionospheric effect,

$$\mathrm{L4} = \mathrm{L1} - \mathrm{L2}. \qquad (3)$$

There are over 40 permanently operating GPS stations already in the Nordic countries and 12 of these belongs to the Finnish permanent GPS network, FinnRef®. The data sampling interval is 30 s and each station tracks all visible satellites (typically 8–12) down to elevation angle 5°. Data (including code, carrier phase and Doppler on both frequencies) are stored permanently and can be post-processed for any kind of research. Data are downloaded from receivers once every 24 hours but there are plans to increase the downloading frequency to once/hour (at least on some stations) within a year.

Coordinates of all stations are known within a few centimetres in the global reference frame. Currently, the orbits of the GPS satellites are known to better than 5 cm in the same frame. This means that the true range between the receiver and a satellite is known within a few cm. Practically all other effects can be eliminated with a combination like in (3) and allows one to estimate the true ionospheric bias also within a few centimetres.

It is a bit surprising that GPS has not been extensively used for ionospheric studies. The system is free, the transmitted signal well controlled and documented and GPS receivers are relatively cheap. For most GPS users the ionosphere is just a noise which should be removed, but GPS can as well be used also for ionosphere studies. Permanent GPS networks offer a good basis for this because the true distances between the receiver and satellites are precisely known. If the coverage of receivers is not dense enough, the network is easy to densify with temporary or new permanent receivers. In principle, even ionosphere tomography could be possible if the density of the network is suitable. In any case, data over half of the Solar activity cycle are already available.

REFERENCES

Klobuchar J. A., 1996: Ionospheric effects on GPS. In *Global Positioning System: Theory and Applications,* Vol. **I**. (Ed. B.W: Parkinson and J. J. Spilker). *Progress in Astronautics and Aeronautics*, vol. **163**, American Institute of Aeronautics and Astronautics, Washington DC. pp. 485–515.

Ollikainen M., H. Koivula, M. Poutanen, R. Chen, 1997: Suomen kiinteiden GPS-asemien verkko. Geodeettisen laitoksen tiedote **16**. Masala. (In Finnish)

Poutanen M., 1998: *GPS-paikanmääritys*. Ursa, Helsinki. 269 s. (In Finnish)

# DETERMINATION OF IONOSPHERIC ELECTRON DENSITY BY MEANS OF SATELLITE RADIOTOMOGRAPHY

Tuomo Nygrén[1], Markku Lehtinen[2] and Evgeny D. Tereshchenko[3]
[1]Department of Physical Sciences, University of Oulu
P.O. Box 3000, FIN-90014 University of Oulu, Finland
tuomo.nygren@oulu.fi
[2]Sodankylä Geophysical Observatory, University of Oulu
FIN-90600 Sodankylä, Finland
[3]Polar Geophysical Institute, 15 Khalturina 183010, Murmansk, Russia

ABSTRACT. A tomographic method based on stochastic inversion is introduced and its applications to ionospheric tomography are shown. The results demonstrate the variability of the ionospheric F region at high latitudes.

## METHOD

We consider a chain of difference Doppler receivers on the ground level. The phase difference observed by each receiver is

$$\delta\Phi \propto \int N ds + C, \tag{1}$$

where $N$ is the electron density, $C$ is an unknown phase constant and the integration is carried out along a ray from the satellite to the receiver. When a satellite flies above the chain, the integral will be measured along many rays crossing each other in the ionosphere.

An annular grid is defined in the vertical plane above the receiver chain, and the unknowns are the phase constants and the electron densities at the grid points. Bilinear interpolation makes the measured phases into linear combinations of the unknowns. Collecting the measurements into a column vector $\mathbf{m}$ and the unknowns into a column vector $\mathbf{x}$ gives

$$\mathbf{m} = \mathbf{A_m} \cdot \mathbf{x} + \boldsymbol{\varepsilon}_\mathbf{m}, \tag{2}$$

where $\mathbf{A_m}$ is a matrix of the linear coefficients and $\boldsymbol{\varepsilon}_\mathbf{m}$ is a column vector containing the measurement errors.

The numerical inversion of this equation is unstable and therefore regularization is needed. The instability is established as too strong point-to-point variations in the inversion results, and it can be eliminated as follows. Consider two grid points $g_i$ and $g_j$ which are either horizontal or vertical neighbours. If we assume that the difference of the electron densities at these points is zero, we make some error $\varepsilon_r^{(ij)}$. This can be written as

$$0 = x_i - x_j + \varepsilon_r^{(ij)}. \tag{3}$$

Carrying this out for all differences of neighbouring grid points makes a single matrix equation

$$\mathbf{0} = \mathbf{A_r} \cdot \mathbf{x} + \boldsymbol{\varepsilon}_\mathbf{r}. \tag{4}$$

Here $\mathbf{A_r}$ is a matrix with elements $+1$, $-1$, and $0$ in appropriate places so that each component of eq. (4) is of the form (3). Eqs. (2) and (4) now give a single matrix equation

$$\begin{pmatrix} \mathbf{m} \\ \mathbf{0} \end{pmatrix} = \begin{pmatrix} \mathbf{A_m} \\ \mathbf{A_r} \end{pmatrix} \cdot \mathbf{x} + \begin{pmatrix} \boldsymbol{\varepsilon}_\mathbf{m} \\ \boldsymbol{\varepsilon}_\mathbf{r} \end{pmatrix}. \tag{5}$$

Assuming that the measurement errors and the components of $\boldsymbol{\varepsilon}_\mathbf{r}$ are Gaussian random variables with zero mean, the posterior density is also Gaussian with a center point

$$\hat{\mathbf{x}}_\mathbf{0} = (\mathbf{A_m}^T \cdot \boldsymbol{\Sigma}_\mathbf{m}^{-1} \cdot \mathbf{A_m} + \mathbf{A_r}^T \cdot \boldsymbol{\Sigma}_\mathbf{r}^{-1} \cdot \mathbf{A_r})^{-1} \cdot \mathbf{A_m}^T \cdot \boldsymbol{\Sigma}_\mathbf{m}^{-1} \cdot \mathbf{m}, \tag{6}$$

where $\boldsymbol{\Sigma}_\mathbf{m} = < \boldsymbol{\varepsilon}_\mathbf{m} \cdot \boldsymbol{\varepsilon}_\mathbf{m}^T >$ and $\boldsymbol{\Sigma}_\mathbf{r} = < \boldsymbol{\varepsilon}_\mathbf{r} \cdot \boldsymbol{\varepsilon}_\mathbf{r}^T >$ are the covariance matrices of $\boldsymbol{\varepsilon}_\mathbf{m}$ and $\boldsymbol{\varepsilon}_\mathbf{r}$, respectively, and $T$ indicates transpose. This center point gives the most probable solution of the inversion problem.

This method offers a controlled way of giving prior information on the electron density to the solver. At heights were small electron densities are expected, their point-to-point variations are also small and therefore small prior variances can be given to the solver. Correspondingly, within regions where the electron density is probably high, great point-to-point variations may occur so that the prior variances should also be great. In this manner the inversion result can be guided to a layer with a reasonable thickness and peak height.

## OBSERVATIONS

We have carried out tomographic measurements in three campaigns arranged in Scandinavia in 1993, 1995 and 1997. Four or five receivers have been used and signals from Russian navigational satellites have been observed. The sites lie approximately along the same magnetic meridian and the satellites fly at an altitude of 1000 km closely parallel to the chain. The results show a meridional cross section of the F region and demonstrate the variability of the auroral and sub-auroral ionosphere in different geophysical conditions. The phenomena visible in the results include the main trough, large F region plasma blobs, field-aligned plasma enhancements associated with upward field-aligned currents and travelling ionospheric disturbances due to atmospheric gravity waves.

## DISCUSSION

Contrary to the various iterative methods used in ionospheric tomography, the present one gives the result by means of a single inversion. Its second characteristic feature is that it does not need any separate procedure for the determination of the phase constants; they are just components of the unknown vector and are determined simultaneously with the unknown electron densities. A comparison with iterative methods like MART and SIRT has shown that stochastic inversion is superior especially in situations with a small number of observers and a high noise level.

# DETECTION OF TRACKING LOOPS PERFORMANCE OF GPS RECEIVERS FROM PPS MEASUREMENTS

**J.Mannermaa [1], K.Kalliomäki [2], T. Mansten [3]**

**[1)] Nokia Mobile Phones, FIN-33100, Tampere, Finland**
**[2)] Univ. of Oulu, Dept. of Electrical Eng., FIN-90570 Oulu, Finland**
**[3)] VTT AUTOMATION, Measurement Technology, FIN-02044 VTT, Finland**

## Introduction

GPS receivers have been under serious study all over the world during the last years due to the scientific and economic possibilities hidden into the positioning and navigation functions. Our GPS studies were made in co-operation with VTT (Technical Research Centre of Finland) in Espoo and the R&T unit of Nokia Mobile Phones. VTT has experience of over ten years and NMP about six years concerning the research of GPS receivers. Testing started in spring 1998, has non-stop characteristic and aims at long term applications of GPS receivers. The goal of our studies is to achieve comparable information and results of the overall performance of different GPS technologies. The aim of this study was to find out the operation and performance of carrier and code tracking loops by studying the PPS pulse. Due to the expanding range of GPS receiver applications with e.g. more stringent positional accuracy demands manufacturers have to concentrate more and more on the performance of internal clocks of GPS receivers.

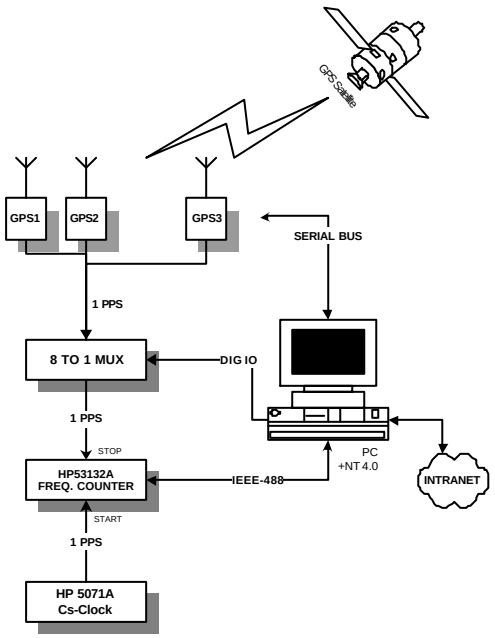


Fig 1: Measurement set-up

## Measurement system

The measurement system is shown in Fig. 1.
It enables multiplexed measurements of PPS pulses and simultaneous measurement of all RS-232 bus data from 8 receivers. The data along with date and time is saved into user-specified files in ASCII format.

## Data processing method

Short-term (10 min) raw measurement results show numerous phase jumps in ns domain, interlaced by smoother periods of phase changes with linear or parabolic characteristics. The generation of PPS pulses seems to include both small, frequent corrective phase jumps and long-term frequency changes of the master clock. The PPS pulse is synchronised to the GPS time by jumping the phase of the divider logic and by manipulating the frequency of the master clock via e.g. numerically controlled oscillators. In

order to find out the phase behaviour of the master clock behind the measured PPS pulses, a model of constant phase jumps (which are probably multiples of an internal clock period) was applied to them. The amplitude of the needed corrections was estimated by differentiating (twice, if needed) the PPS measurement results of each receiver. The differences grouped around certain values with equal intervals in all but one receiver. These group average intervals were used as estimates for the jump correction.

The corrections were made in three steps for each receiver:

- each phase difference was divided by the chosen phase jump estimate and the quotient was rounded into integer value, which tells the sum of phase jump corrections applied by the receiver to the PPS output at the point observed (with signs taken into account)
- these integers were summed from the first jump forward. The sum at each measurement result gives the total sum of signed corrective jumps from the beginning to the point observed
- the first phase result was taken as such. Every following phase result was corrected by the respective sum of corrections mentioned above, multiplied by the chosen phase jump estimate

Moreover, several measurements were made to study the influence of ambient temperature changes on the frequency and phase of master clock. The frequency and phase of the GPS receiver's master clock was also measured directly with an active probe.

**Results**

The PPS phase and frequency jump results are in Table 1. The used phase jump estimates are presented in Col. 2. Frequency jumps were observed only in receiver D. It seemed to be the only way of PPS phase control in this receiver. In Col. 4 are the observed ranges of allowable frequencies (frequency is adjusted if it tries to go outside the limits).

Table 1: Phase and frequency jumps

| GPS-receiver | Phase jump | Frequency jumps | Frequency limits |
|---|---|---|---|
| | ns | ±1·10-9·f | ±1·10-9·f |
| | | | |
| A | 26 | - | 10 |
| B | 62 | - | 30 |
| C | 320 | - | not observed |
| D | - | 22 | - |
| E | 175 | - | 80 |
| F1 | 183 | - | 90 |
| F2 | 183 | - | 90 |

By applying the described difference method neat parabolic phase curves with occasional abrupt frequency changes are achieved, Fig. 2 and 3. These curves show that the frequency

is fluctuating smoothly but kept within the desired range by adjustments. Fig. 4 depicts the behaviour of one receiver when a fast temperature change is applied.

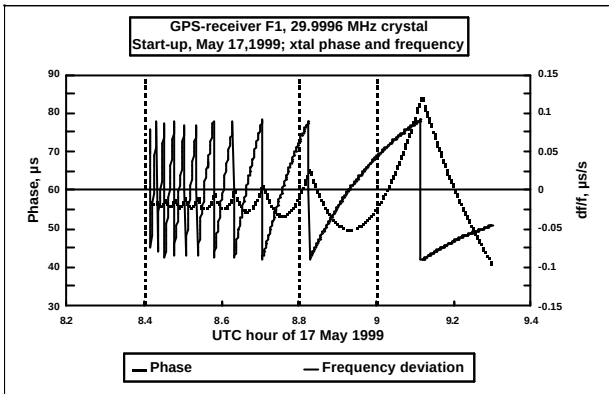


Fig.2: The phase and frequency behaviour of GPS-receiver F1 after start-up

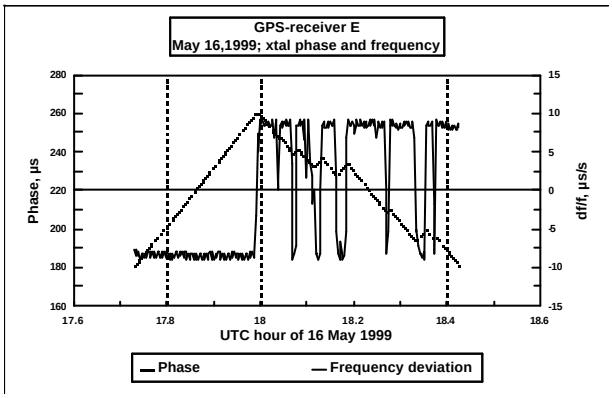


Fig.3: The phase and frequency behaviour of GPS-receiver E

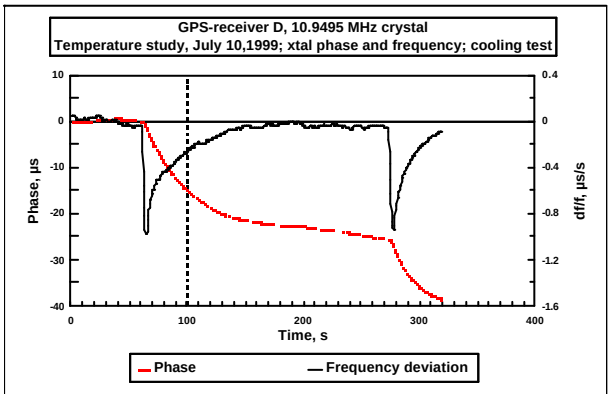


Fig.4: The phase and frequency behaviour of GPS-receiver D, two cooling tests

## Conclusions

The results of the PPS measurements show that by analysing the PPS data one can detect both frequency and phase adjustments of master clock output. By applying the method described above the constant phase corrections and frequency range limits can be detected and removed after which the behaviour of the master clock can be observed. Generally, the master clock runs freely, and both phase and frequency adjustments are done by digital circuits after it (numerically controlled oscillators). The quality of the crystal oscillator for master clock is chosen so that the subsequent circuits can compensate for all the predictable changes of the master clock output. OCXOs and NCXOs are probably never used because of their high price. Strong ambient effects can cause the GPS receiver to lose its tracking and hamper and delay the reacquisition. Therefore the XO is isolated from abrupt environmental effects by using sufficient (thermal) shields and power regulation. The better the crystal oscillator is isolated from its surroundings the better short-time behaviour is to be expected from it. The ageing of the crystal is usually hidden under ambient effects and easily compensated by GPS control loops, and therefore not worth measuring.

# GROUND-BASED SPACE WEATHER OBSERVATIONS USING THE MIRACLE SYSTEM

K. Kauristie, O. Amm, E.I. Kallio, P. Janhunen, and A. Viljanen
Finnish Meteorological Institute
Geophysical Research Division
P.O.B. 503, FIN-00101 Helsinki, Finland
kirsti.kauristie@fmi.fi

The Magnetometers - Ionospheric Radars- Allsky Cameras Large Experiment (MIRACLE) is a two-dimensional instrument network which consists of 25 magnetometers (the IMAGE magnetometer network), five all-sky cameras and the STARE coherent scatter radar system (*Syrjäsuo et al.,* 1998). These instruments in the Scandinavian sector cover an area from subauroral to polar cap latitudes over a longitude range of about two hours of local time (Figure 1). The network is maintained as international collaboration under the leadership of the Finnish Meteorological Institute (FMI).

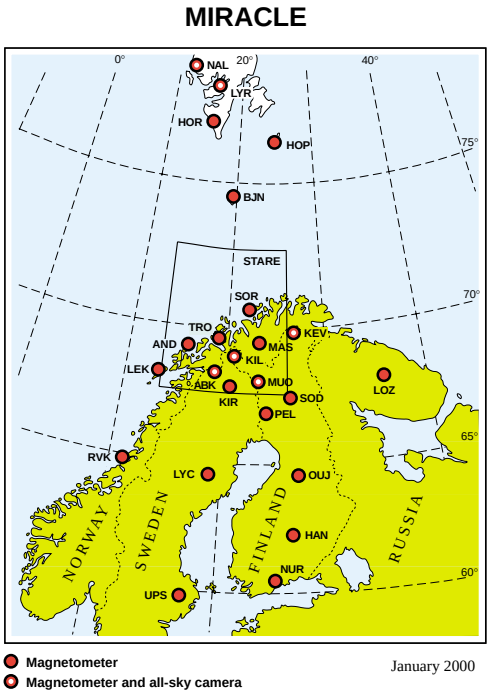


Figure 1: The MIRACLE instrument network

MIRACLE observations provide a unique possibility to model the ionospheric electrodynamics in the whole area covered by the STARE radar. Ohm's law and the current continuity equations can be solved with the method of characteristics (*Amm et al.,* 1995) when MIRACLE electric and magnetic field recordings and an estimate of the Hall-to-Pedersen conductance ratio are used as input data. MIRACLE data are useful also when trying to understand in a wider context magnetospheric satellite observations which usually are very local and thus suffer from spatial-temporal ambiguity.

Space weather studies often deal with global scale energy and particle transfer processes in the coupled solar wind - magnetosphere - ionosphere system. In the presentation we show how MIRACLE observations can be utilized also in space weather research, although the network is monitoring mesoscale activity. We demonstrate with an example that the phenomena causing the actual problems e.g. in ground-based technological systems can be very local. The possibilities to use MIRACLE observations and the method of characteristics for estimating the energy dissipation in the ionosphere will also be discussed.

REFERENCES

Amm, O., 1995: Direct determination of the local ionospheric Hall conductance distribution from two-dimensional electric and magnetic field data: application of the method using models of typical ionospheric electrodynamic situations, *Journal of Geophysical Research*, **100,** 21473-21488.

Syrjäsuo, M.T., T.I. Pulkkinen, P. Janhunen, A. Viljanen, R.J. Pellinen, K. Kauristie, H.J. Opgenoorth, S. Wallman, P. Eglitis, P. Karlsson, O. Amm, E. Nielsen, E. Nielsen, and C. Thomas, 1998: Observations of substorm electrodynamics using the MIRACLE network, in *Proceedings of the International Conference on Substorms-4*, eds. S. Kokubun and Y. Kamide, Astrophysics and Space Science Library, **238,** Terra Scientific Publishing Company/Kluwer Academic Publishers, 111-114.

# GEOMAGNETICALLY INDUCED CURRENTS AND THEIR EFFECTS IN THE FINNISH POWER SYSTEM

Jarmo Elovaara
Fingrid Oyj
P.O.Box 530
FIN-00101 HELSINKI, Finland
jarmo.elovaara@fingrid.fi

It might sound odd that a power transmission company has something to do with space weather related questions. However, the solar wind and its ionospheric interactions with Earth's geomagnetic field cause phenomena, which can be detrimental to different kind of man-made systems. In the surface of Earth these interactions are seen as longitudinal electric field strengths, which have at greatest the magnitude of some volts per kilometer. This pseudo-stationary geo-electric field causes that geomagnetically induced currents (GIC's) will flow in all conductive structures which have at least two connections in the earth. The high voltage power transmission system is a potential target to disturbances caused by GIC's because the neutral points of the 400 kV and 220 kV windings of most system transformers are earthed. The neutral point earthing is done to limit the voltage stresses under earth fault conditions and has a direct favourable impact on the construction costs of the system.

In the case of GICs the co-operation of FMI and the transmission grid owner has started in middle of 1970'ies. The grid owner has measured the pseudo-stationary GIC-currents in the neutral points of certain 400 MVA, 400 kV system transformers and has organised field tests to measure the behaviour of the Finnish power transformers under strong DC-magnetisation. It has further supported the GIC-modelling work of FMI by arranging special GIC-measurement campaigns as well as by ordering studies where the GIC-distributions and GIC-statistics in the Finnish 400 kV grid have been determined using the geomagnetic data of FMI. The last of this kind of co-operation project was finished during this summer. In this project the main emphasis was given to the determination of GIC-distributions over the Finnish 400 kV and 220 kV grids so that the probabilities for simultaneous occurrences of large GICs in several 400 kV substations could be determined.

Large GICs can occur in an electric power network, if the following conditions are met:

- the network locates under the auroral zone,
- the resistivity of earth is high,
- the system consists of long overhead transmission lines (OHTL) and
- the neutrals of the transformers connected to the OHTL-system are earthed.

Nordic countries as well as certain parts of Canada and USA fulfil these conditions. GICs have caused in electric power networks: 1) blackouts mainly due to disturbances in reactive power balance of the system, 2) equipment (mainly transformer) failures and 3) erroneous operations of certain protection relays. Failures and blackouts are experienced mainly in USA and Canada, but under very severe storms problems have been met even in United Kingdom. However, fatal effects influencing directly in the power transfer capability of the system have not been observed in Finland, although very high

DC-currents (over 200 A) have been measured in certain transformer neutrals during severe GIC-disturbances.

The main reason to all these unwanted effects is the half-cycle saturation of such transformers, which do have an earthed winding neutral point. The saturation of the transformer creates great leakage fluxes in the transformer. These in turn can have detrimental effects in the transformer if they are not of suitable type from the point of view of DC-magnetisation and if the leakage fluxes can cause in the transformer local overheating due to eddy currents. In addition, the transformer saturation distorts the supplied voltage and current by creating harmonics, which can overheat individual, other components and which do impair the quality of the supplied electricity.

The measurements made with Finnish power transformers have shown that the leakage fluxes caused by half-cycle saturation do not harm the transformers used in Finland. This is probably due to the fact that the Finnish transformers are mainly 3-phase, 5-legged, full-wound 3-winding transformers, which type is one of the most insensitive to effects of DC-saturation. In addition, due to fault current limiting and reactive power compensation reasons, already the normal short-circuit reactances of the Finnish transformers are relatively high. This means that the Finnish transformers have been designed against the effects of large stray fluxes already when the risks caused by GIC's were not even recognised. Further, the resistance of the earth-fault current limiting reactors connected between the neutral points and the earth limit the magnitude of the induced GIC's. (It can be mentioned that the damaged transformers have usually been single-phase autotransformers, which do have a very low short-circuit reactance and consequently a very low leakage flux in conditions where DC-excitation is not present.)

The obvious reason to the fact that GIC's have not disturbed operation of the grid is in turn, that the reactive power compensation capacity in Finland is high enough to take care of the full saturation of one system transformer. However, a simultaneous saturation of several transformers might cause a risk situation but the probability of this kind of event is quite low. Therefore so far no mitigation methods or warning systems have been taken into operation in Finland, but studies are going on to quantify the risk caused by the simultaneous saturation of several transformers.

A fact to be kept in mind is that during the last years the Finnish 400 kV grid has developed so that the occurrence probability of large GI-currents has decreased a lot. The main influencing factors are the new intermediate substations shortening the lines and implementation of series capacitors on the 400 kV tie lines to Sweden and on important north-south-directed 400 kV lines (the last mentioned series capacitor banks are now under construction). The series capacitors increase the power transfer capacity of the system but they also break the DC-flow in the line in question. It is therefore very probable, that the the Finnish power system does not either in future need any specific protection against the effects of GIC's.

# PROJECT ON GEOMAGNETICALLY INDUCED CURRENTS IN THE FINNISH NATURAL GAS PIPELINE NETWORK

Antti Pulkkinen[1], Kari Pajunpää[1], Ari Viljanen[1], Risto Pirjola[1],
David Boteler[2], Larisa Trichtchenko[2]

[1]Finnish Meteorological Institute
Geophysical Research Division
P.O.B. 503, FIN–001010 Helsinki, Finland
antti.pulkkinen@fmi.fi

[2]Geomagnetic Laboratory, Geological Survey of Canada
7 Observatory Crescent, Ottawa
Ontario K1A 0Y3, Canada

## PROJECT OVERVIEW

A project implemented to study effects of space weather on the Finnish natural gas pipeline was launched between the Finnish Meteorological Institute and Gasum Oy, the owner of the Finnish natural gas pipeline (*Pulkkinen*, 1999; *Pirjola et al.*, 1999). In the first part of the project we derived a theoretical model for calculating geomagnetically induced currents (GIC) and pipe-to-soil (P/S) voltages in the Finnish natural gas pipeline. In the second and third parts of the project, we carried out GIC and P/S voltage measurements in the pipeline, and with the help of the theoretical model and measurements, derived statistical predictions for the occurrences of GIC and P/S voltages in the Finnish pipeline.

## MEASUREMENTS

Measurements are carried out near the centre of the pipeline network, at Mäntsälä (Fig. 1). GIC is obtained by measuring the magnetic field created by the quasi-DC-current flowing along the pipeline. The only major problem in measurements is that the cathodic protection system disturbs the voltage measurements. GIC at Mäntsälä is less affected by the protection system and thus the effect is not critical from the point view of the study.

## STATISTICAL PREDICTIONS

A linear dependence between the geoelectric field calculated using magnetic data from the Nurmijärvi Geophysical Observatory and GIC and P/S voltage at seven different sites was derived using the theoretical method. Coefficients of the linear model were then used to determine GIC and P/S voltages for the period 1993-1998. These statistics were then extended to describe GIC and voltages of magnetically different years using a normalization based on the geomagnetic $A_k$ activity index of Nurmijärvi.

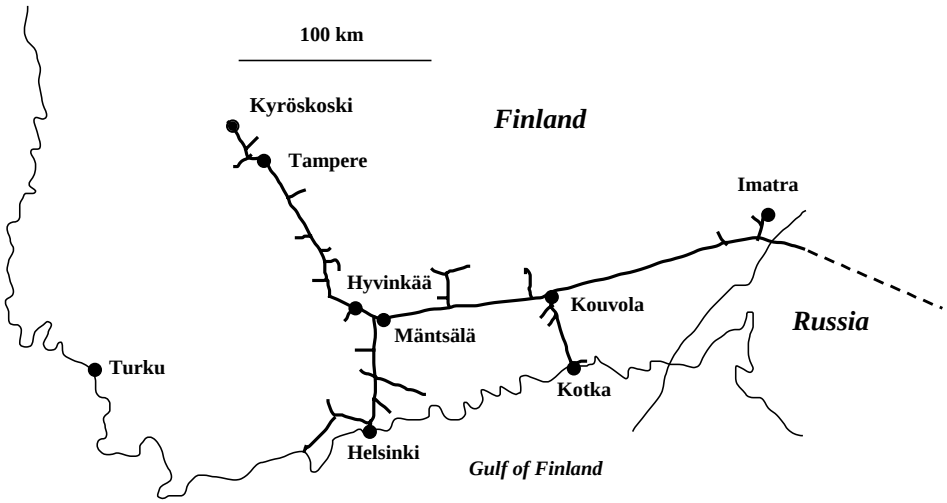


Fig.1. Finnish natural gas pipeline network

Statistical predictions clearly point out the most GIC-sensitive sections of the Finnish pipeline: the largest P/S voltages are found at Kyröskoski, which is one end of the network, while the smallest variations are seen at Imatra and Kouvola. The most probable sites for large GIC are Mäntsälä and Imatra where GIC may exceed 100 amperes. The largest value measured so far since November 1998 is 30 A on July 15, 2000.

From the point of view of pipeline operation, P/S voltages due to geomagnetic disturbances, especially at the end points of the network, seem to exceed the CP voltage during significant time periods. Thus, if coating of the pipeline is for some reason damaged and the CP fails to keep the direction of the electric current from the soil to the pipeline, the risk of corrosion is increased (*Henriksen et al.*, 1978).

ACKNOWLEDGEMENTS

Our thanks go to Mr. Juha Vainikka, Senior Vice President of Gasum Oy, and to Mr. Matti Pitkänen for a great support and interest in the study.

REFERENCES

Pirjola, R., A. Pulkkinen, H. Nevanlinna and K. Pajunpää, 1999: Study on Space Weather Effects on the Finnish Natural Gas Pipeline, *EOS, Transactions, American Geophysical Union, 80,* 332-333.

Pulkkinen, A., 1999: Geomagneettisesti indusoituvat virrat Suomen maakaasuverkossa (in Finnnish), *Finnish Meteorological Institute, Reports,* **1999:2**, 46 p.

Henriksen, J.F., R. Elvik and L. Granåsen, 1978: Telluric Current Corrosion on Buried Pipelines, *Proceedings of the 8th Scandinavian Corrosion Congress NMK 8*, 167-176.

# Wireless Communication – Part II

# RADIOWAVE PROPAGATION ASPECTS OF MOBILE LOCATION TECHNIQUES

Jaakko Lähteenmäki
VTT Information Technology
P.O. Box 1202, 02044 VTT, Finland
E-mail: jaakko.lahteenmaki@vtt.fi

**Abstract – Several techniques are currently under development for locating mobile phones. The performance of the location techniques is highly dependent on the propagation of radio waves. This presentation highlights propagation aspects related to location performance.**

## 1. INTRODUCTION

Currently, there are two main approaches for mobile phone location: a GPS (Global Positioning System) receiver module is integrated to the handset or the transmitted signals of the cellular network are used for location. GPS positioning is based on computing the handset coordinates with the help of geometric distances retrieved from signal delay measurements [3].

For network-based location there are several possibilities [1]. A rough method uses the signal levels received from base stations for the estimation of distances between base stations and the mobiles [2]. However, most attention has been paid to methods based on the delay times between base stations and the mobile. For example, in the so called E-OTD method (Enhanced Observed Time Differences) the handset measures delay-time differences towards base stations [7]. The location solution is achieved with the help of at least three base stations. In addition the synchronisation difference shall be compensated by using calibration receivers at known locations. Another possibility is to measure the direction of arrival of the signals transmitted by the mobile by at least two base stations and compute the location with the help of the two bearings. Promising results have also been received by the so called database correlation method (DCM), which is essentially similar to the enhanced signal strength (ESS) method referred in [1]. In this method, the signals received by the mobile are compared with a database containing measured and predicted fieldstrength information. The location is estimated by finding the highest correlation of the received signals and the signals in the database.

## 2. COVERAGE ASPECTS

The performance of the location methods is considerably dependent on radiowave propagation. The prerequisite for each of the location methods is that a sufficient signal level is obtained at the receiver. This is a challenging demand because connections to several satellites or base stations are needed at the same time. The most difficulties are faced indoors. According to an empirical study [4] the required link margin for covering buildings from satellites at 1.5 GHz band varies between 20-60 dB depending on the type of building. The indoor performance of GPS can be increased by special receiver techniques yielding a link margin of even 25 dB [5], which would enable GPS positioning in buildings in certain cases.

The indoor location performance of terrestrial systems is considerably improved if indoor base stations are available. Outdoor location performance is degraded in rural areas where sometimes only one base station can be received at a given point.

## 3. SIGNAL DELAYS CAUSED BY MULTIPATH PROPAGATION

The received signal is a combination of multiple delayed signal components, which severely disturbs the distance measurement accuracy of GPS and other methods based on distance or angle measurements. First signal arriving at the receiver may easily be delayed

by 50 metres or more compared to the direct path between transmitter and receiver. Furthermore, the error in distance measurement results in a 2-3 fold error in location accuracy [3]. Recently, a method based on ray-tracing and a building database has been presented for correcting the error introduced by the multipath propagation [8].

## 4. PROPAGATION EFFECTS ON THE DATABASE CORRELATION METHOD

Delays caused by multipath propagation do not affect the DCM algorithm, since the distances between base stations and the mobile are not used. However, the DCM algorithm is affected by received signal level variations caused by fast spatial fading, moving objects in the environment as well as attitude and placement of the handset. The effect of fast fading as well as the effect of moving objects can be reduced by averaging. The effectiveness of averaging is better if the handset is in continuous movement, for example as when carried by a walking person.

As it is not possible to carry out measurements everywhere the DCM database shall include fieldstrengths predicted by planning tools. Typical r.m.s. prediction errors in microcell environments (ray-tracing methods) are 10-15 dB. Simulated results for the DCM method indicate accuracy better than 60-70 m with 90% probability for prediction error range 10-20 dB [6]. This simulation assumed a regular base station grid of urban indoor and outdoor base stations with density 125 base stations per $km^2$. Initial results based on measurements carried out by VTT in operating GSM network, indicate outdoor location accuracy in microcell environment of better than 100 m with 90% probability.

## REFERENCES

[1] Koshima H., Hoshen J., "Personal locator service emerge," IEEE Spectrum, Feb. 2000, Vol. 37, No. 2, pp. 41-48.

[2] Figel W. G., "Vehicle location by a Signal Attenuation Method," IEEE Trans. on Vehicular Technology, vol. VT-18, no. 3, Nov. 1969, pp. 105-109.

[3] Kaplan E. D., "Understanding GPS principles and applications," Artech House, 1996, 554 p.

[4] Karhu S. & al., "In-building DAB service planning," Executive summary of ESA project 12330/97/NL/US, September 1999, 44 p.

[5] Moeglein M, Krasner N., "An introduction to SnapTrack server-aided GPS technology," report available at http://www.snaptrack.com.

[6] Pajunen J., "A distributed location service implementation using independent and reusable software components," Helsinki University of Technology, Master's thesis, 6.6. 2000, 76 p.

[7] Rantalainen T., "Cellular solutions in Europe," Location-based mobile value added services workshop, 5-6 May 1999, Brussels.

[8] Wang P., Hsu L., "Improved GPS location positioning in NLOS propagation environments," Millenium Conference on Antennas and Propagation, 9-14 April 2000, Davos, Switzerland.

# LOCATION OF GSM TERMINALS USING A DATABASE OF SIGNAL STRENGTH MEASUREMENTS

Heikki Laitinen, Tero Nordström, and Jaakko Lähteenmäki
VTT Information Technology
P.O.Box 1202, FIN-02044 VTT, Finland
heikki.laitinen@vtt.fi

ABSTRACT. A GSM location trial using a database of measured signal strength values is described in this presentation.

## INTRODUCTION

Several cellular location techniques have been introduced lately, most of them being based on signal timing or angle of arrival measurements, see e.g. *Drane et al.* (1998). These techniques suffer from degraded accuracy when no line of sight between the mobile and the base stations exist. This is typical in densely built urban areas where high buildings often block the line of sight and signal propagates with less attenuation along street canyons than through the buildings. However, accurate location in city centres is desirable since location services will most probably find a lot of users there.

The accuracy degradation caused by non-line-of-sight propagation can be avoided with the Database Correlation Method (DCM). In this method, the signal strength values and/or the propagation time delays, as a function of geographical position, are stored in a database. For location determination, a correlation-type algorithm is used to find the best match between the values measured by a mobile terminal and the entries of the database. The values stored in the database can either be measured or calculated using a network planning tool. A location system employing calculated signal strength values is already in use in Japan (*Koshima & Hoshen* [2000]).

## LOCATION TRIAL

We have conducted a DCM location trial in an operating GSM network. In this trial, the received signal levels of the serving cell and six strongest neighbours were measured as a function of position. This information is measured by standard GSM phones to facilitate handover. The trial area was a street grid in the centre of Helsinki, covering an area of approximately 3 $km^2$. Most of the measurements were performed with a phone and a laptop computer inside a car. The speed of the car varied from 0 to 40 km/h and 2 measurement samples per second were collected. The ‘true’ coordinates for the measurement samples were obtained by mouse-clicking marker points on a map during the measurement. The database was formed by averaging all measurement samples inside each square of a location grid, with neighbouring grid points spaced 20 m apart. In addition to the measurements forming the database, a 8.5 km long test route through the area was driven.


*Figure 1. Measured street grid (grey), test route (solid black line), and the coordinates returned by the DCM algorithm ('+'-marks).*

## RESULTS

The test route, as well as the locations returned by the DCM for all the test samples, are depicted in Figure 1. Few clearly deviated results can be seen, but most of the location results are on the route. However, there are sections on the route where no location results are found. The location error is typically directed along the route. The mean location error is 43 m, and the 67th and 95th percentiles are 49 m and 108 m, respectively.

## CONCLUSIONS

The signal strength –based DCM is a competitive alternative for cellular location especially in city centres. In restricted areas, the required database can be easily formed by measurements. For large-scale implementation, an accurate field-strength prediction tool would probably be needed.

## REFERENCES

Drane, C., M. Macnaughtan and C. Scott, 1998: Positioning GSM telephones. *IEEE Communications Magazine*, Vol. 36, No. 4, 46-59.

Koshima, H. and J. Hoshen, 2000: Personal locator services emerge. *IEEE Spectrum*, Feb. 2000, 41-48

# CMOS RF Models for Mobile Radio IC Design

**Jan Saijets[1], Markku Åberg[1] and Mikael Andersson[2]**
1) VTT Electronics, IC Group, P.O.Box 1101, FIN- 02044 VTT, Finland
2) Nokia Research Center, P.O. Box 407, FIN-00045 NOKIA GROUP, Finland
email: jan.saijets@vtt.fi

***Abstract***

*The goal of this research was to evaluate existing mainstream CMOS models at radio frequencies. Their strengths and weaknesses were compared which after possible improvement ideas were studied for the MOSFET equivalent circuit.*

## Introduction

The four mainstream CMOS models chosen for comparison were EKV [1], BSIM3v3 [2], Philips MOS Model 9 [3] and the old classic Berkeley Spice Level 3 MOSFET model [4]. The work was done by first extracting a complete scalable DC model which after the AC parameters were extracted using both capacitance measurements and S parameter fitting. Both DC and AC extractions were made by using the APLAC circuit simulator and by programs written in APLAC description language. In AC measurements and studies the MOSFET device was considered as a two-port having the gate as the input and the drain as the output. This study was done using only NMOS devices.

This study was motivated by the fact that quite a small amount of research had been focused on the AC and RF properties on MOSFET models. Mostly the improvements and studies were concentrating on improving the DC behavior. The rapid growth of mobile phone industry increased the need for cheap IC circuits. This in turn demanded better device models especially in the case of CMOS as it may evolve into a practical process at RF. Continuous efforts to shrink the minimum channel length of CMOS processes have dramatically improved the speed of MOS transistors thus becoming a possible choice at RF.

## The Evaluation Studies

The comparison of different models showed that the DC model is one of the most important factors. In this evaluation study the extrinsic AC models between different MOSFET models had identical equivalent circuits including the parasitic series resistances and zero-bias capacitances. Even the substrate diode models are quite equal in performance as it seems that the bulk-diode capacitances can be quite accurately modelled with only an area and a sidewall component, although MOS9 and BSIM3v3 provide more possibilities. The only serious differences in the AC behavior is thus generated by the active charge model and the current derivatives. When these are taken into account it could be stated that Level 3 and EKV are not as good as BSIM3v3 and MOS9 due to their problems in the DC model.

Comparisons between BSIM3v3 and MOS9 show that the simple approach of the latter seems to be at the least as good as the one of BSIM3v3. The bias dependent zero-bias capacitances of BSIM3v3 do not give any significant advantage. The opposite results in the beginning of the

project was due to the active charge model error caused by the improper NQS description. The active capacitances were practically a few per cent of the total capacitance. This bias dependent part of the capacitances were then somewhat compensated by the complex zero-bias capacitance model. BSIM3v3 had also some odd $C_{gd}$ capacitance behavior anomalies. These can be avoided by the proper XPART parameter value.

It seems that if all bias points are chosen in deep saturation the models do get very similar AC fits. The differences becomes more evident after other regions of operation has been included in the extraction bias points. However, when measuring bias points close to the threshold voltage the temperature effects are more serious and have to be taken into account. The differences of AC behavior are basically generated by the different active charge models as there are the real differences. The amount of inversion charge can vary as can the bias dependence. And again, bad DC extraction can distort the bias dependence.

Even though, efforts have been made to produce accurate models there are still problems to get a scalable conductance fit with the new MOSFET models. Also the active charge models are inaccurate between the transition from saturation to linear region although the transition regions have been made continuous.

## Conclusion

Four mainstream CMOS models were studied at RF by comparing their S parameter fits. It was found out that the real differences of the model AC behavior results from their DC and active charge models. It became also evident during the project that the more complex the MOSFET model is the more efforts have to be put on parameter extraction. Both DC and AC extraction may very easily fall into local numerical minima that are far from the physical values complicating the model optimization.

After model evaluation possible improvements were studied for the MOSFET equivalent circuit. Only some of them provided practical improvement in AC behavior.

Possible future studies for improving the MOSFET AC properties would be to study the bulk resistance geometry dependences for different bulk resistance models. Also the basic DC model could be improved to gain a more scalable conductance model.

## REFERENCES

1. C. C. Enz, F. Krummenacher, E. A. Vittoz, "An Analytical MOS Transistor Model Valid in All Regions of Operation and Dedicated to Low-Voltage and Low-Current Applications", Analog Integrated Circuits and Signal Processing, vol. 8, pp. 83 - 114, 1995

2. Y. Cheng, M. Chan, K. Hui, M. Jeng, Z. Liu, J. Huang, J. Chen, R. Tu, P.K. Ko, C. Hu, "BSIM3v3 Manual", University of California/Berkeley, 1996

3. R.M.D.A Velghe, D.B.M. Klaassen, F.M. Klaassen: "MOS Model 9", Unclassified report NL-UR 003/94, Philips Electronics N.V. 1994

4. D. Foty, "MOSFET Modeling with SPICE", Prentice Hall PTR, 1997, pp. 318 - 378

# A PASSIVE INTERMODULATION PHENOMENON IN BASE STATION ANTENNA DESIGN FOR MOBILE NETWORKS

Viatcheslav Golikov, Sami Hienonen, Tomas Sehm, Pertti Vainikainen
Helsinki University of Technology,
Radio Laboratory
P.O.B. 3000 FIN-02015 HUT,
Helsinki, Finland
v.golikov@hut.fi

ABSTRACT. This paper aims to consider the passive intermodulation (PIM) problems occurring in passive devices when two or more high-power signals are simultaneously present on a way of RF energy flowing. Due to nonlinear properties of the passive parts located near the high-strength field region, the unwanted PIM components with combination of carrier frequencies may fall within receive band of the base station. As the result, the possibility of the receiver sensitivity degradation always exists.

In the present paper, two antenna prototypes (microstrip- and probe-fed stacked patches) for GSM900 standard were used for PIM measurements under various conditions. Given samples have one and two locally situated PIM sources respectively.

## INTRODUCTION

It is well known [1,2] that passive parts of both the antennas and the environmental objects may contain nonlinear current-voltage relationships in themselves. The level of the undesirable PIM products in high power transmitters may be critical for the sensitive parts of receivers. Each of the PIM components has own physical nature of the non-linearity and may be caused by any conditions irregularity. The total influence of all the PIM components depends on various reasons and conditions, which must be taken into account during design process of the high-power RF units for the base stations equipment. The following major aspects have to be considered: applied materials, surface contamination, type of connectors, kinds of junctions, tunneling effect, breakdowns, corrosion, electrostriction and corona effects, thermal deviations, humidity variations etc. Because of all these reasons mentioned, to obtain more or less stable results, repeatable PIM experiments must be performed during the antenna design stage [3]. Special attention should be paid to dependence of the magnitude of the PIM products in relation to carrier power levels in transmitter. Some correspondence between the frequency properties of the explored samples and PIM level itself should also be established where possible.

## MEASURED COMPONENTS

It is obvious, that complex signal combined at PIM frequency is based on spectrum form of the parent signal, therefore for simplest frequency analysis many developers use few one-tone signals. In common case, using two RF carriers (sinusoidal form), the full expression for all IM components can be written as:

$$f_{IM} = \pm m*f_1 \pm n*f_2,$$

where $f_1$, $f_2$ - carrier frequencies; $m$, $n$ – arbitrary integers.
Order of the PIM product is: $Order = |m| + |n|$.

The frequency relationships between each of the PIM components are shown in Fig.1. The odd PIM components are located close to the carriers $f_1$, $f_2$, and as a rule the level of the 3rd order product is much higher than others. For GSM receiver's equipment it may result in sensitivity degradation, which is independent of the receiver's own noise floor.

RESULTS

Typically, the PIM requirement for GSM base station equipment is about –110…–120 dBm when input RF power levels are 43 dBm. The test results for 3rd order PIM response of the examined antenna prototypes are given in Fig.2. The probe-fed antenna sample meets good PIM response under the 41 dBm input power, and could be suitable for low-power applications. Actually, we didn't aim to create the antenna with high PIM performance, but given prototypes will be used for the experiments in future.

REFERENCES

[1] Helme, B.G.M., 1998: Passive intermodulation of ICT components. *IEE Colloquium on Screening Effectiveness Measurements (Ref. No. 1998/452)*, 1/1–1/8.

[2] Lui, P.L. and Rawlins A.D., 1989: Passive non-linearities in antenna systems. *IEE Colloquium on Passive Intermodulation Products in Antennas and Related Structures*, 6/1–6/7.

[3] Rosenberger, B., 1999: The measurement of intermodulation products on passive components and transmission lines. *IEEE MTT-S Symposium on Technologies for Wireless Applications 1999, Digest 1999*, 57–62.

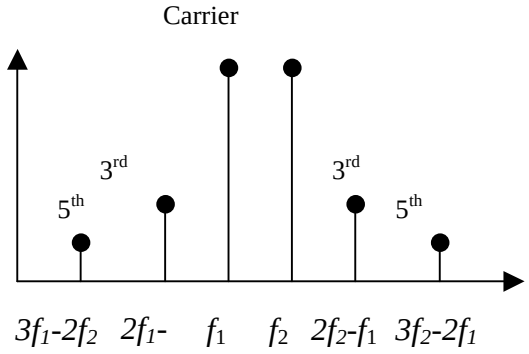


Fig.1. Spectrum of a two-carrier system with PIM response.

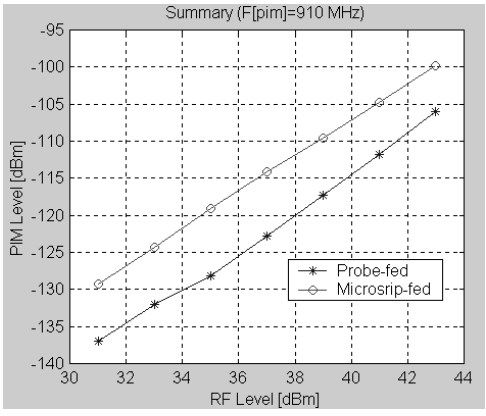


Fig.2. PIM performance of the experienced samples.

# DESIGNING A DUAL-FREQUENCY BALUN TO ELIMINATE THE EFFECT OF RF FEED CABLES IN MEASUREMENTS OF SMALL ANTENNAS

C. Icheln, P. Vainikainen,
Helsinki University of Technology,
IDC/Radio Laboratory,
P.O. Box 3000, FIN-02015 HUT, Finland
icheln@hut.fi

ABSTRACT. A dual-frequency balun applied in measurements of small dual-frequency antennas reduces parasitic currents on the surface of the RF feed cable, so that the influence of the RF measurement cable on the radiation pattern is minimised.

## INTRODUCTION

The complex transmission coefficient between a well-known measurement antenna and the mounted handset antenna under test (AUT) is usually measured with help of a network analyser. Errors in the measured radiation pattern or antenna gain can be expected due to the RF cable acting as a) a secondary radiator driven by the surface currents on the conducting surface of the handset and b) a reflector, that re-radiates part of the arriving fields. The use of sleeve-like baluns on the feed cable, located near the handset, was presented in [1], [2] as a lossless, though band-limited, means to reduce the effect of the RF cable on the antenna measurement. In this work two designs of a dual-frequency balun are presented, both of which effectively reduce the perturbation of the radiation pattern to an acceptable level at two frequencies. For measurements of mobile handset antennas that operate at 900 MHz and 1800 MHz this is a useful feature.

## DUAL-BAND BALUN

We consider a half-wavelength long tapered coaxial cylinder around the RF feed cable, very small in diameter at the end pointing away from the handset (see Fig. 1). When placing this impedance step half a wavelength away, it is transformed into an high impedance at the connection of the RF cable to the handset. The cable surface becomes practically inaccessible for surface currents.

The second design uses a cap-like design that allows no leakage. The stacked coaxial quarter-wave cap acts as a dual-frequency band-stop filter. Figure 2 illustrates the geometry and the dimensions. The capacitance of the gap basically acts as a low-pass filter, so for high frequencies the outer cavity is blocked away, and the inner cavity is the active quarter-wave balun. At low frequencies the outer cavity is added to the inner one, so the effective quarter-wave cap is twice as long.

## RESULTS

Figure 3 shows the computer simulated H-plane radiation patterns at the centre frequencies of the baluns, i.e. at 2 GHz. The absolute signal levels seen in the plot are arbitrary, as produced by the FEM software package. However, the relative levels of the different simulated cases are normalised to the same total radiated power. At 1 GHz (not shown here) with either one of the balun designs the field perturbations are decreased by

more than an order of magnitude, i.e. from more than 10 dB down to less than 1 dB. At 2 GHz the stacked-cavity balun is as effective as at 1 GHz, but the tapered cylinder is not quite as effective, i.e. perturbations up to ±2.5 dB occur in the sidelobes.

The bandwidth of design 1 is 10% at 1 GHz, and 5% at 2 GHz. For design 2 the bandwidth is 10 % both at 1 GHz and at 2 GHz. The criterion for the bandwidth is that the perturbation of the mainlobes, which is caused by the RF cable, stays within ±2 dB, when compared to the radiation pattern without any cable attached to the handset.

REFERENCES

[1] C. Icheln, J. Ollikainen, P. Vainikainen, 'Reducing the influence of feed cables on small antenna measurements', *Electronics Letters*, Vol. 35, No. 15, (1999), 1212-1214.

[2] C. Icheln, M. Popov, P. Vainikainen, S. He, 'Optimal reduction of the influence of RF feed cables in small antenna measurements', *Microwave and Optical Technology Letters*, vol. 25, no. 3, (2000), 194-196.

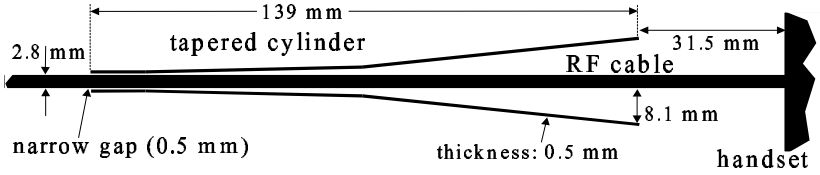


Fig. 1: Crosssection of dual-band balun 1, indicating its location on the RF cable.

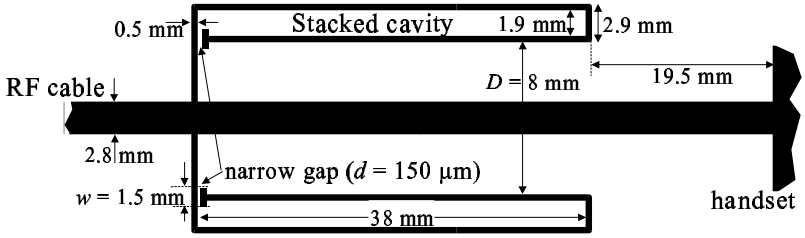


Fig. 2: Crosssection of dual-band balun 2, indicating its location on the RF cable.

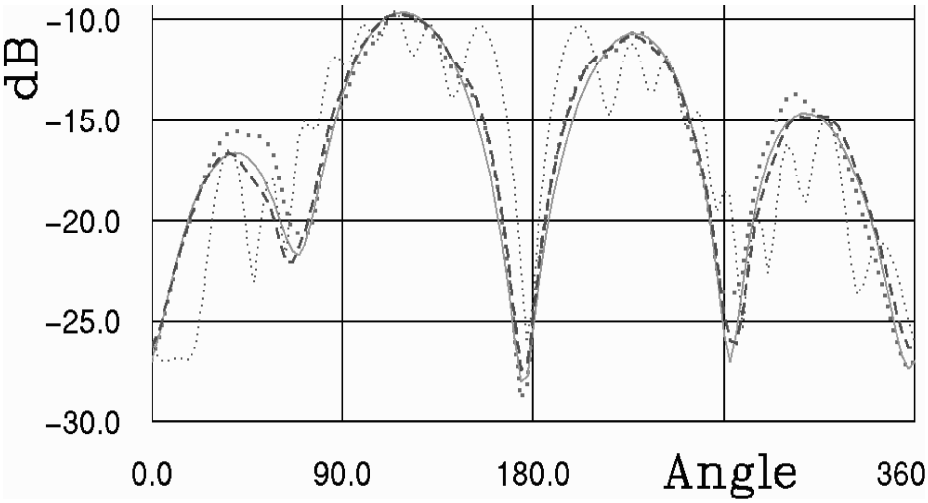


Figure 3: The H-plane radiation pattern at 2 GHz. Balun 1 is indicated by large dots, balun 2 by a dashed line, the reference case without any cable attached is denoted by a solid line, and the far-field pattern with a 500 mm long cable attached and no balun is marked with smaller dots.

# MULTIPLE-SIGNAL INTERMODULATION IN THE NONLINEAR RADIO DEVICES.

Natalia Y. Ermolova
Helsinki University of Technology
Communications and Radio Laboratories
P.O.B. 2300, FIN-02015 HUT, Finland
natalia.ermolova@hut.fi

ABSTRACT. A theoretical analysis into intermodulation products of the multiple pseudo-noise Gaussian signals fed into mildly nonlinear device is presented. Analytical formulas for output spectrum are obtained. The results may be used for analysis of nonlinear radio devices ( e.g. multicarriers amplifiers) as well as for their design.

## INTRODUCTION

A great number of radio devices exhibit nonlinear characteristics and signal distortions are inserted into radio channel because of this fact. When multiple signal is fed into nonlinear device the interaction of the input signals leads to unwanted intermodulation ( IM ) products which must be taken into account by RF designers. In this work we present the analytical description of output spectrum for model of input multiple signal the each component of which is considered as bandlimited Gaussian process with zero mean (such situation is typical for e.g. CDMA systems).

## MODEL DESCRIPTION

The input multiple signal is assumed to be

$$s(t) = \sum_{i=1}^{3} x_i(t)\cos(\phi_i(t)) \qquad (1)$$

with power spectral density (PSD) of each $x_i$

$$p_{x_i}(f) = \begin{cases} N_o/2, |f| \le B, \\ 0, |f| > B \end{cases}.$$

In (1) $\phi_i(t) = 2\pi f_i t + \varphi_i$, $f_1 < f_2 < f_3$.

The number of components in (1) is chosen to avoid cumbersome calculations and because of the fact that the main influence on the channel under consideration is due to the adjacent channels. If all carriers are equally spaced in frequency the distortions in center channel are the worst ones. On the contrary side lobes have the main influence on the out of band emission.

The model of nonlinearity is assumed to be truncated Taylor's series that is

$$y(t) = a_1 s(t) + a_3 s^3(t) \quad , \qquad (2)$$

where $y(t)$ is output signal.

Substituting (1) into (2) and taking into account only principal zone components we have

$$y(t) = \sum_{i=1,\, j,k\neq i}^{3} \{\{a_1 x_i + 3/4 a_3 x_i^3 + 3/2 x_i (x_j^2 + x_k^2)\}\cos\phi_i - 3/4 x_i^2 x_j \cos(2\phi_i - \phi_j) - 3/4 x_i^2 x_k \cos(2\phi_i - \phi_k) + 3/2 a_3 x_i x_j x_k \cos(\phi_i - \phi_j + \phi_k)\} \quad (3)$$

To calculate spectrum of (3) we define spectrum of each component of it taking into account that if $z(t) = A(t)\cos(2\pi f_0 + \varphi_i)$ then $p_z(f) = 1/4\{p_A(f - f_0) + p_A(f + f_0)\}$ As in [1] we employ Einstein-Wiener-Khintchine theorem [2] to calculate PSD of each component in (3). We employ also facts that for Gaussian stochastic processes $E[x_1 x_2 x_3 x_4] = \sigma_{12}\sigma_{34} + \sigma_{13}\sigma_{24} + \sigma_{14}\sigma_{23}$ and for independent ones $E[f(x_1)g(x_2)h(x_3)] = E[f(x_1)]E[g(x_2)]E[h(x_3)]$ [3].

The final expression for output spectrum is:

$$p_y(f) = \sum_{i=1}^{12} p_{y_i}(f)\ ,$$

where $p_{y_i} = \begin{cases} k_{1i} + k_{2i}\left[3B^2 - (f - f_i)^2\right], |f - f_i| \le B \\ k_{3i}\left[3B - |f - f_i|\right]^2, B < |f - f_i| \le 3B \\ 0, |f - f_i| > 3B \end{cases}$ ,

$f_4 = 2f_1 - f_2,$
$f_5 = 2f_1 - f_3,$
$f_6 = 2f_2 - f_3,$
$f_7 = 2f_2 - f_1,$
$f_8 = 2f_3 - f_1,$
$f_9 = 2f_3 - f_2,$
$f_{10} = f_1 + f_2 - f_3,$
$f_{11} = f_1 + f_3 - f_2,$
$f_{12} = f_2 + f_3 - f_1.$

and $k_{ij}$ are $a_1, a_3, B, N_0$ dependent parameters.

REFERENCES

1. Q. Wu, M. Tesla and R. Larkin 1998: On design of linear RF Power amplifier for CDMA signals. *Int. Journal RF and Microwave CAE 8*, 283-292.

A. Papoulis 1984: Probability, Random Variables and Stochastic Processes, Mc Graw-Hill, New York.

# Natural Electromagnetic Fields

# MULTICHANNEL LIGHTNING FLASHES DETECTED IN FINLAND IN 1998-2000

Tapio J. Tuomi
Finnish Meteorological Institute (FMI)
Geophysical Research Division
P.O.B. 503, FIN-001010 Helsinki, Finland
tapio.tuomi@fmi.fi

ABSTRACT. The new lightning location system of FMI, installed in 1997, locates separately each stroke of a flash. The data are now accurate enough to identify flashes with multiple strike points. The strike-point separations and interstroke time intervals show a pattern which may be related with the types of new channel formation: forking from an old channel and triggering of a totally new stroke.

## IMPACT LIGHTNING LOCATION SYSTEM

The present lightning location system in Finland has been manufactured by Global Atmospherics, Inc., USA, and consists of five "IMPACT" sensors and a central unit. The sensor name refers to improved accuracy by combining direction-finding and time-of-arrival techniques. Each stroke of a flash is stamped by GPS-synchronized time. A two-sensor detection is sufficient for a fair accuracy, and three or more sensors often lead to location errors smaller than 1 km. The two combined methods allow not only good accuracy but also an estimation of the accuracy. About one half of the located flashes are multiple, i.e. a flash consists of more than one stroke (up to 15). Furthermore, many multiple flashes are found to strike at more than one point on the ground; up to five points per flash have been detected. This study attempts to relate this multichannelling to the nature of the flash formation.

## SELECTION OF DATA

From the three seasons 1998-2000 a data set has been selected with the requirement that each stroke of a multiple flash has an estimated error of at most 1 km, and that each stroke has been detected by at least three sensors. The latter condition improves the error estimate and is also believed to prevent contamination from cloud flashes (only ground flashes are accepted). The system groups located strokes into flashes under the conditions that for successive strokes, the strike-point separation is within about 10 km and the time interval does not exceed 500 ms. From a set of 250,000-300,000 located strokes per year, a total of almost 10,000 multiple flashes, containing over 25,000 strokes, meet the accuracy criteria. Most flashes are negative; less than 200 flashes in this set are positive (90 % of positive flashes are single-stroke). For successive strokes of a multiple flash, the strike-point separation and interstroke interval are calculated. Figure 1 shows these plotted for the negative flashes of the year 2000 (the figure is similar for the other years).

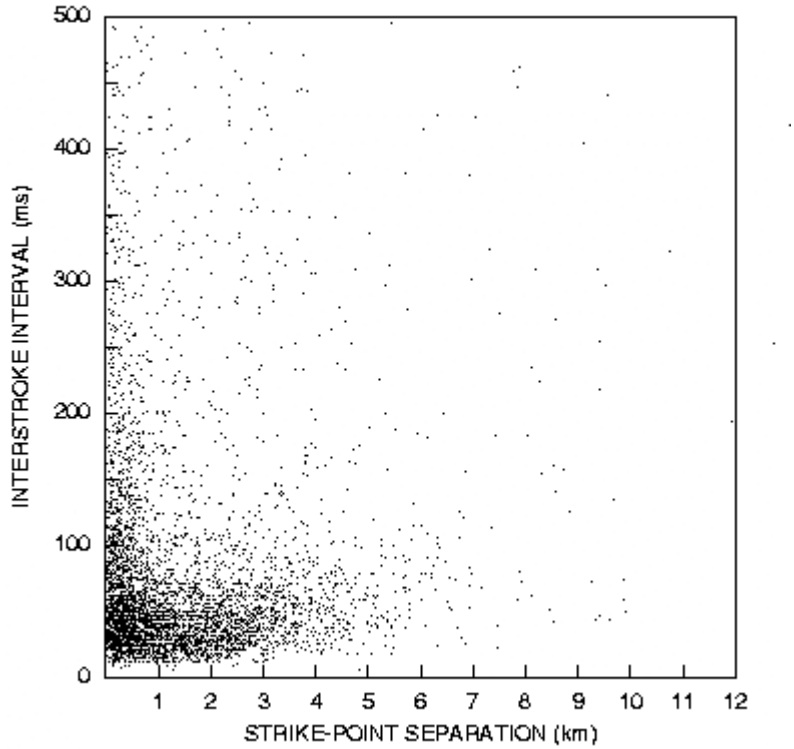


Figure 1. Relation between strike-point separation and interstroke interval for successive negative-negative strokes.

DISCUSSION

The points in Fig. 1 are mostly concentrated below 1 km separation or below 100 ms interval. Most points with small separation may actually be single-channel cases, which also contain very long interstroke intervals. After a long interval, the same channel can only be re-used by the next stroke if a so-called continuing current keeps the channel hot enough. Otherwise, a new stepped leader forms and opens a new (lower part of the) channel to the ground and the flash becomes forked. In the Figure, forking is seen to concentrate at intervals below 100 ms.

About 10 % of the points are scattered, representing long intervals (> 100 ms) associated with wide (> 1 km) separations. At least part of these are thought to be cases where the channel is not forked but a totally new channel, associated with a different charge region in the cloud, is triggered by the previous stroke. In fact, a large part of these scattered points occur in cases where the latter stroke has inverted polarity (not shown here). Most positive flashes also fall in this category. Almost all are two-stroke, with one half having an inverted-polarity (negative) second stroke, and the points are scattered. This conlusion is also supported by the finding that for "normal" negative flashes (single-channel or forked) a subsequent stroke is usually weaker than the first stroke. In these cases, the fraction of scattered points is 7-8 %. When a subsequent stroke is stronger than the first one, the fraction of scattered points is 12-13 %. This reflects greater independence of the triggered stroke on the triggering stroke, which should be the case with the formation of a totally new channel.

# CO-OPERATION OF FINGRID AND FINNISH METEOROLOGICAL INSTITUTE IN QUESTIONS RELATED TO NATURAL ELECTROMAGNETIC FIELDS

Jarmo Elovaara
Fingrid Oyj
P.O.Box 530
FIN-00101 HELSINKI, Finland
jarmo.elovaara@fingrid.fi

The designers, owners and operators of electric power networks have always needed the basic meteorological data like ambient temperature, wind speed and snow/ice load distributions, because they are important when the design standards for constructions and equipment needed in the electric power transmission are specified. During the last years interest to this kind of "classical" meteorological data has increased because different kind of extreme weather conditions have seemed to occur more frequently (and in some cases also with more severe outcomes) than earlier. Examples of this kind of occurrences are extremely low temperatures (about -50 $^{o}$C) twice within the last 15 years in Lapland, heavy storm crossing over France in December 1999 and the "ice storm" with freezing rain in January 1998 in Quebec, Canada. The both last mentioned events caused long-lasting blackouts in energy supply both in France and in Quebec. In addition to these kind of "classical" meteorological events transmission network owners and operators are interested about certain occurrences, which are related to natural electromagnetic fields and space weather effects. With these I mean especially the occurrence of thunderstorms and geomagnetically induced currents (GICs) and their effects to the power transmission. The co-operation between Fingrid Oyj (and its predecessor Imatran Voima Oy) and the Finnish Meteorological Institute (FMI) has already long tradition in both these fields. The following contribution concentrates on the co-operation in lightning recordings and on the application of information, which can be obtained from the lightning location system. A separate contribution is made on the FMI-Fingrid co-operation in research related to space weather, especially geomagnetically induced currents.

In the case of recording of lightning the co-operation between FMI and the Finnish electrical utilities started already in 1960'ies when a lightning flash counter (LFC) network was established in Finland. Most of the counters were "operated" by power transmission and distribution companies but the results were always collected and analysed by FMI. Due to this co-operation Finland is the only Nordic country which has a representative lightning statistics from early -60'ies to the present moment. Due to this co-operation we have had available e.g. ground flash density statistics over the whole country. However, the density of LFC-network was not sufficient to make the location of the lightning strokes possible. In addition, the LFC-network recorded alo cloud-to-cloud and intra-cloud flashes. When lightning location systems became commercially available, FMI started to use so called LLP-system, where the location of a ground flash is determined with the cross-bearing principle. The transmission grid owner assisted FMI by financing the purchase of one direction finder unit. When this system was modernised in 1997 by acquiring so called IMPACT-system, Fingrid supported the acquiring of the new system by making a ten year contract with FMI to get the following lightning flash/stroke data from FMI: location, time and current amplitude. In addition, a separate contract has been signed in 2000 so that Fingrid has access to the lightning viewer system of FMI.

At present access to an on-line lightning location system is quite important for a power utility, although the ground flash density in Finland is relatively low and although man cannot influence on the occurring of thunderstorms or on the consequences of an observed lightning stroke. This is due to the fact that electricity is treated within EU as a product which has to fulfil certain quality requirements. Due to the lightning location data the IMPACT-system offers the following basic benefits for operator and owner of the electric power transmission system:

- Lightning location data can be compared with the fault location data. More reliable fault statistics as well as improved knowledge about the efficiency of the lightning protection systems are some of the most important results.
- If lightning causes a permanent fault, the repair teams can be conducted more rapidly and more accurately to the correct place.
- Warnings about approaching lightning storms can be given so that repair and maintenance groups are better prepared to possible necessary actions.
- Maintenance and other works can be interrupted in time so that an approaching thunderstorm will not cause any risk to the members of the maintenance team.
- In principle, when an extensive and reliable ground flash density map is available, the line corridors and substation locations could be selected so that they will not locate in places which are very prone to lightning flashes/strokes.

Also the probability distributions of the characteristics of the lightning currents are useful information when the power transmission and distribution systems are designed. Important characteristics are e.g. amplitudes as well as shape and duration of positive and negative main strokes and subsequent strokes, Joule-integral of the current and charge of the stroke. The current amplitude and its steepness determine the overvoltage stressing the insulated structures but the current amplitude has also importance in simplified models on the basis of which the positioning of earth wires or other protective constructions is determined. The Joule-integral ($\int i^2(t) \cdot dt$) gives the thermal energy fed by the lightning in the electric conductor and the charge in turn has a correlation with the amount of metal which will be smelt at the stroke point.

At the moment only lightning current amplitudes can be obtained as an additional information directly from the IMPACT-system. Already this information has revealed that the earlier statistics about lightning current amplitudes are not necessary completely reliable. As an example can be mentioned that according to the statistics published by CIGRE[1] the median value of the peak value of the negative main stroke is about 32 kA whereas the corresponding value on the basis of FMI's measurements is only about 12 kA. The difference might be caused by the fact that the CIGRE-distribution is determined from measurements made with the help of high structures like chimneys and TV-towers whereas the IMPACT-system values are related to real cloud-to-ground flashes. However, the reason might also be that calibration methods of the IMPACT-system are not yet accurate enough. Therefore there is still both the need and possibilities to lightning related studies also in Finland.

[1] CIGRE = Conférence Internationale des Grands Réseaux Electriques à haute tension (an international research association of power production and transmission companies, manufacturing industry and research organisations)

# NEW RESEARCH RADARS IN SODANKYLÄ

Antero Väänänen
University of Oulu, Sodankylä Geophysical Observatory
Tähteläntie 112, FIN-99600 Sodankylä, Finland
av@sgo.fi

ABSTRACT. A general review of different types of ground-based radar systems used for scientific research is given. The new ionosonde, meteor-MST- and weather radars under construction in Sodankylä are presented.

## IONOSONDES

Ionosonde measures vertical position and other properties of the ionospheric layers. Most are Vertical Incidence Sounders. The apparent height is determined from the delay between the leading edge of the transmitted pulse and the returned echo. More advanced ionosondes measure also the frequency, doppler shift and its spread, amplitude, phase, angle (direction) of arrival and polarization of the returned signal. Pulses are single or coded, and may be repeated on a certain frequency, and then the transmission is moved to the next frequency. There is also a variant using a continuous frequency-sweeeped signal. The frequency range is from 0.5 - 1 MHz to 16-20 MHz. Frequency can be stepped in many different ways, linearly or logarithmically, with gaps in the sweep. TX powers go up to tens of kW. The antennas of a VIS are directed upwards and somehow made to cover the required large bandwidth.

## AURORAL RADARS

Auroral radars are a tool for looking at the magnetic field-aligned structures and phenomena of the polar atmosphere. Because the field lines are almost vertical there, and VHF and higher frequencies propagate along straight lines but HF waves refract, it is possible to get much stronger echo signals back to radar on HF than on VHF or UHF.

### HF auroral radars

These radars operate in synchronised pairs (nearest located in Finland and Iceland) viewing the same area, and are together called the SuperDARN (Dual Auroral Radar Network). They use frequency range 8 – 20 MHz, divided in several narrower subranges, and automatically choose a quiet frequency inside the most suitable subrange. The main antenna group has a gain of 25 dB and 16 electronically formed switchable beams inside a 52 degree sector. A secondary group is used in determining the vertical arrival angle. A 600 W PA is feeding each TX antenna. Transmitted signal consists of pulse groups (5-7 pulses, 200-300 ∝s long) repeated at 10 Hz for 7 seconds in each beam, and the scan of the beams is repeated at 2-minute intervals.

### VHF auroral radars

A representative system is STARE (Scandinavian Twin Auroral Radar Experiment) with stations at Midtsandan, Norway (140.0 MHz), and Hankasalmi, Finland, 143.8 MHz. TX peak power is 50 kW, radiated with a group of 8 long yagi antennas.

## IONOSPHERIC RADARS

The structures in the ionosphere generate coherent scatter, when probed with a radar wavelength in the same order with their dimensions. Incoherent scatter radars work with signals scattered back by individual electrons in the ionospheric plasma. These radars use much higher TX powers and antenna gains than the former group. EISCAT has 3 radars: 224 MHz, 3 MW, 46 dB, and 931.5 MHz, 1.5 MW, 48 dB (near Tromsø), and 500 MHz, 1 MW, 45 dB (on Svalbard).

## ATMOSPHERIC RADARS

Ionospheric and auroral radars measure mainly phenomena in the ionized plasma in upper atmosphere, the next ones mainly the neutral atmosphere at lower heights.

MST, ST and MLT radars
These are used for research of turbulence, wave and wind phenomena at heights 15 – 200 km, and can be adapted also to ionosphere or meteor studies. Many use frequencies around 50 MHz; about 2-3 MHz and UHF are used, too. A typical antenna system is a large group of vertical yagis. TX powers are in the kW - MW range.

Wind profilers, boundary layer radars
These radars represent a new and growing group, specially intended for wind measurements, for heights of about 200 m to 20 km (vertical profile or distribution of wind speed, direction, and turbulence). ST/MST radars are not much different technically. The frequencies for this new user are usually from three ranges: around 50 MHz, about 400-500 MHz and around 1.3 GHz.

Meteor radars
These do not differ much from MST radars, and many radars are used for both purposes in different configurations. Meteor radar records meteor trails, which can come from almost any direction, and cannot thus have very directional antennas. Best frequencies are in the range 20-60 MHz. Meteors can be a research subject as such, but often this radar is used for the same purpose as the MST, because the meteor trails drift with upper atmosphere winds, and so these winds can be measured also in this way. TX powers are around 10 kW, TX antenna is a simple yagi and receiving array consists of a few more yagis.

Weather radars
This name is used for the “ordinary” weather radars which give mainly a picture of the rain situation of the area around them, using rotary scanning with low antenna elevation. In the U.S. the frequency allocation for these radars is 2700-2900 MHz, in Europe 5600-5650 MHz. Typical transmitter output powers are 200-800 kW and antennas 4-8 meter paraboloids with 40-50 dB gain.

## NEW RADARS IN SODANKYLÄ

A meteor radar is under construction at SGO. It will have an additional antenna system giving the possibility to use it as a MST radar, too. A different receiving antenna array format (compared to other meteor/MST radars) will be used, giving less ambiguity in signal arrival direction determination. The new radar coding principles developed in Sodankylä will now be applied to these radar types.
At the same time the existing ionosonde of SGO will be replaced with a new construction, applying the same receiving antenna configuration and signal coding ideas. A common controller drives both systems, interleaving the transmissions to avoid interference between the systems. Both receiving systems use same components and it is possible to combine them to make all receiving channels available to both. All essential signal processing is done in general purpose computers, with the help of the GURSIP-GUTBOX interface solution from Invers Oy. The meteor-MST-radar operates on 36.9 MHz and the ionosonde on 0.5 - 30 MHz in their basic modes. When the ionosonde has the same receiving antenna configuration as the meteor radar, it is possible to use the ionosonde also as a lower frequency (HF) meteor radar.
A new weather radar has been constructed atop the Luostotunturi hill at 514 m asl. In addition to being a part of the FMI operational network it is used also by Invers Oy for radar technology development, testing and demonstration.

# SUDDEN IMPULSE EVENTS OBSERVED BY MAGNETOMETERS AND COHERENT RADARS

**N. Partamies[1)], K. Kauristie[1)], P. Eglitis[2)] and M. Uspensky[1)]**

**1) Finnish Meteorological Institute**
**Geophysical Research Division**
**P.O.Box 503, FIN-00101 Helsinki, Finland.**
**email: noora.partamies@fmi.fi**
**2) Swedish Institute of Space Physics**
**Uppsala Division, Sweden.**

The September 1999 International Space Weather Campaign was arranged to study space weather events from their initiation at the Sun to the impacts at the Earth. During the campaign the common aim of the numerous research groups was to collect a dataset of ground-based and satellite observations as complete as possible for further analysis and modelling work. SuperDARN, the global network of coherent radars, has an important role in the collected data set.

In this study we analyse ionospheric effects of three sudden impulse (SI) events, which took place on 12$^{th}$, 15$^{th}$ and 22$^{th}$ September at UT-times 0400, 2019, 1220, respectively (as defined from ground-based magnetometer data). In all these cases, clear fast shocks were observed in the solar wind by ACE, WIND and IMP-8 satellites. On 15$^{th}$ September IMF $B_z$ stayed positive before and after the shock, while the two other events were associated with negative IMF $B_z$. The study utilises SuperDARN data together with recordings of several magnetometer chains (IMAGE, CANOPUS, GIMA, and Greenland) in the different magnetic local time (MLT) sectors of the auroral zone. Special emphasis is given to the observations of the MIRACLE network, which consists of the IMAGE magnetometer chain, six all-sky cameras and the STARE radars in the Scandinavian sector.

In the presentation we discuss especially the ionospheric effects caused by the transient pressure pulses of the SIs. During the events on 15$^{th}$ and 12$^{th}$ minor effects were observed while in the last case on 22$^{th}$ the effects in both the radar and the magnetometer data were clear. The SuperDARN and the STARE radars lost the signal for about 5 minutes, which we believe to be due to an increase in precipitation and thus an increase in ionospheric conductivity and decrease of the electric field below the radar detection threshold value. Also, a strong pulse, measured in magnetic north component, propagated from dayside to nightside. The pulse was first recorded at lower latitudes (55.6$^{o}$N) and about 4 minutes later an amplified pulse was observed at higher latitudes. After the SI related pulse, some pulsations, with a period of 3 to 7 minutes, were recorded by the IMAGE magnetometers and the STARE Norway radar. Our observations of the time delay, propagation and strengthening of the pulse are consistent with an SI model by *Araki* (1994).

REFERENCES

Araki, T., 1994: A Physical Model of the Geomagnetic Sudden Commencement, in "Solar Wind Sources of Magnetospheric Ultra-Low-Frequence Waves", AGU Geophysical Monograph 81, 183--200.

# GEOELECTROMAGNETIC MODELLING AT THE FINNISH METEOROLOGICAL INSTITUTE

Risto Pirjola
Finnish Meteorological Institute
Geophysical Research Division
P.O.B. 503, FIN–001010 Helsinki, Finland
risto.pirjola@fmi.fi

A geomagnetic disturbance and the associated electric field at the earth's surface are primarily caused by magnetospheric-ionospheric currents and secondarily by currents induced within the earth. Modelling the geoelectromagnetic field thus requires assumptions about space currents and about the earth's conductivity structure. In this paper, the latter is assumed either uniform or layered. The simplest model contains a vertically-propagating primary field and a uniform earth. It easily permits the estimation of the electric field in terms of measured magnetic data. Auroral regions, including Finland, often experience fields created by an intense ionospheric electrojet current. An infinitely long line current is the simplest model of an electrojet. Electric and magnetic fields occurring at the surface of a layered earth have integral expressions over a horizontal wave number. Such a simple model has been extended at the Finnish Meteorological Institute (FMI) by adding a longitudinal space dependence into the current, and more sophisticated models contain vertical or field-aligned currents that couple the ionosphere to the magnetosphere. At FMI, the line current electrojet has also been extended to a sheet current having any spatial distribution. Then the formulas giving the electric and magnetic fields are double integrals over two wave numbers. Though being exact, such equations are complicated and do not permit fast numerical computations necessary in time-critical applications. This shortcoming is avoided by the use of the "complex image method" (CIM), in which the earth is formally replaced by a perfect conductor located at a complex depth. Originally CIM was developed for a horizontal current distribution but, using equivalent currents, it has been shown at FMI that CIM also works for a system containing vertical currents. CIM yields very accurate formulas for the magnetic field and for the horizontal electric field at the earth's surface. The formulas are also easy to be applied to fast numerical computations. It is the horizontal electric field that drives geomagnetically induced currents (GIC) in electric power transmission systems, pipelines and other conductor networks. So studies of GIC constitute an important application of CIM. In particular, the GIC-effectiveness of different ionospheric event types can easily be investigated using CIM.

# EXACT IMAGE THEORY APPLIED TO GEOPHYSICS

Jari J. Hänninen and Ismo V. Lindell
Helsinki University of Technology, Electromagnetics Laboratory
P.O. Box 3000, FIN-02015 HUT, Espoo, Finland
jari@eml.hut.fi

Risto Pirjola
Finnish Meteorological Institute, Geophysical Research Division
P.O. Box 503, FIN-00101 Helsinki, Finland

Since its introduction in *Wait* (1969), the complex image principle or Wait's image principle has become very popular for computing geophysical low-frequency fields due to atmospheric currents and other geo-electromagnetic sources above the earth. The method is an extension of the classical image principle associated with a perfectly electrically conducting (PEC) plane and is asymptotically valid when $\omega \to 0$. The Wait's image is normally presented as a geometric image of the original source in a PEC plane at a complex depth depending on the conductivity of the ground. The principle was later extended to stratified ground by expressing the complex depth in terms of the impedance of the stratified ground. In 1984 an exact form for the image theory was constructed by one of the authors and the Wait's image principle was shown to emerge as its asymptotic approximation. In the formalism of the exact theory the image of a point source is a line source in complex space.

The Wait's image principle was originally defined for a vertical magnetic dipole (horizontal current loop), and it can be applied to any horizontal current distribution provided the current is solenoidal, i.e., it satisfies $\nabla \cdot \mathbf{J}(\mathbf{r}) = 0$, and the frequency is low enough. However, if the divergence of the horizontal current does not vanish, there is accumulation of charge and the Wait's image does not give good results. It is the purpose of the present paper to derive an extension to the Wait's image principle from an asymptotic case of the exact image theory so that the charge distribution can also be taken into account.

The outline of the paper is as follows. First we review the basics of the exact-image theory for the planar interface and consider its low-frequency asymptotic form when $\omega \to 0$. Next it is shown that the exact image expressions can be simplified from an infinite series of Bessel functions to simpler Bessel function formulas which are asymptotically exact in the low-frequency case. Finally, by applying delta and step-function approximations to the image functions, we obtain simple approximative image expressions from which the Wait's image is seen to emerge as one example. Numerical verification and criteria for the application of the approximate images end the paper.

REFERENCES

J.R. Wait, 1969: Image theory of a quasi-static magnetic dipole over a dissipative ground. *Electr. Lett.*, **5**, 281-282.